2015

Localization and tracking of robotic endoscopic capsules using multiple positron emission markers

Trung Duc Than
University of Wollongong

Localization and Tracking of Robotic Endoscopic Capsules Using Multiple Positron Emission Markers

A thesis submitted in partial fulfilment of the
requirements for the award of the degree

Doctor of Philosophy

from

UNIVERSITY OF WOLLONGONG

by

Trung Duc Than
M.Eng., B.Eng.

Faculty of Engineering and Information Sciences
School of Mechanical, Materials and Mechatronic Engineering

June 2015

Declaration

I, Trung Duc Than, declare that this thesis, submitted in partial fulfilment of the requirements for the award of the degree Doctor of Philosophy, from the University of Wollongong, is wholly my own work unless otherwise referenced or acknowledged. This document has not been submitted for qualifications at any other academic institution.

Trung Duc Than
June 17, 2015

Table of Contents

Declaration ii

List of Figures vii

List of Tables x

List of Abbreviations xi

Abstract xiii

Acknowledgments xv

1 Introduction 1

1.1 Wireless capsule endoscope 1
1.2 Research problem 4
1.3 Research aim and research objectives 5
1.4 Thesis structure 6

2 Literature Review 8

2.1 Localization methods based on magnetic field 8
2.1.1 Magnetic localization for passive endoscopic capsules 9
2.1.1.1 Utilization of a permanent magnet 9
2.1.1.2 Utilization of a secondary coil 11
2.1.1.3 Utilization of a 3-axis magneto-resistive sensor 12
2.1.1.4 Discussion 13
2.1.2 Magnetic localization for magnetically actuated capsules . . . 13
2.1.2.1 High-frequency alternating magnetic field 14
2.1.2.2 Utilization of inertial sensing 15
2.1.2.3 Measuring the magnetic field generated for actuation 16
2.1.2.4 Discussion 17
2.2 Localization methods based on electromagnetic waves 18
2.2.1 Radio waves 19

2.2.1.1 Received signal strength indicator (RSSI) 19
2.2.1.2 Radio frequency identification (RFID) 21
2.2.2 Visible waves 23
2.2.3 X-rays 25
2.2.4 Gamma rays 26
2.3 Other localization methods 26
2.4 Summary 28

3 Methods and Materials 29
3.1 Introduction 29
3.2 Principle of operation 30
3.2.1 Positron emission 30
3.2.2 Annihilation and gamma rays 31
3.2.3 Positron emission tomography 31
3.2.4 Coincidence events 32
3.2.5 Scintillation detection systems in PET 33
3.2.6 Tracking multiple positron emission sources 34
3.2.7 Proposed localization method for WCE 35
3.3 Conceptual system design 36
3.3.1 "Capsule with marker" prototype 36
3.3.2 Isotopes and markers 36
3.3.3 Gamma ray detectors 37
3.4 Tracking algorithm 38
3.4.1 Removing corrupted lines and finding the triangle center . . . 40
3.4.2 Initialization method 42
3.4.3 Fuzzy C-mean clustering algorithm 43
3.4.4 Failure prediction method 45
3.5 Radiation dose estimation 46
3.6 Summary 49

4 Simulation Study 50
4.1 Introduction 50
4.2 Overview of GATE 51
4.3 Geometric phantom simulation 52
4.3.1 Simulation procedure 53
4.3.1.1 Scanner geometry 53
4.3.1.2 Phantom 54
4.3.1.3 Sources and markers 55
4.3.1.4 Digitizer 55
4.3.1.5 Physics list 57

4.3.1.6 Simulation execution and data collection 57
4.3.2 Performance evaluation using the full-ring model 58
4.3.2.1 Accuracy of finding triangle's centroid and effectiveness of removing corrupted lines 59
4.3.2.2 Position and orientation error 60
4.3.2.3 Failure prediction and initialization 62
4.3.2.4 Effect of phantom size and capsule movement speed on the tracking accuracy 63
4.3.3 Performance comparison between the full-ring scanner and a smaller detector system 64
4.3.4 Marker activity selection 67
4.4 Voxelized phantom simulation 68
4.4.1 Simulation procedure 68
4.4.1.1 Voxelized phantom 68
4.4.1.2 XCAT phantom 70
4.4.1.3 Importing XCAT phantom into GATE 71
4.4.1.4 Capsule movement 72
4.4.2 Running simulations on UOW HPC cluster 73
4.4.3 Results 75
4.5 Discussion and summary 76

5 Experimental Evaluation 79
5.1 Introduction 79
5.2 Experimental apparatus 79
5.2.1 Radioactive markers 80
5.2.2 Experimental capsule 81
5.2.3 Moving track 82
5.2.4 Phantom 83
5.3 Experimental procedure 84
5.4 Processing experimental data 85
5.5 Results 87
5.5.1 Position error of each marker 90
5.5.2 Orientation error of the capsule 92
5.5.3 Relative distance error 93
5.5.4 Precision of the tracking algorithm 93
5.6 Discussion 94

6 Algorithm Improvement 97
6.1 Introduction 97
6.2 Rigid-body transformation 99

6.3 Improved tracking algorithm based on rigid-body transformation . . . 100
6.3.1 Mathematical form of the problem . . . 100
6.3.2 Solution . . . 102
6.4 Performance evaluation of the new tracking algorithm . . . 106
6.4.1 Performance evaluation using experimental data . . . 107
6.4.2 Performance evaluation using simulation data . . . 108
6.5 Discussion and summary . . . 109

7 Discussion and Conclusion **111**
7.1 Discussion . . . 111
7.2 Limitations . . . 113
7.3 Conclusion . . . 114
7.4 Main contributions . . . 114
7.5 Recommendations for future research . . . 115

References **117**

Appendix A: GATE macros **130**

Appendix B: XCAT phantom parameters **139**

Appendix C: List of Publications **146**

List of Figures

1.1 A conventional endoscope 1
1.2 Wireless capsule endoscope and its small size 2
1.3 General structure of an endoscopic capsule 3
1.4 Schematic diagram of possible modules of a future WCE 4
1.5 Position and orientation information of a capsule inside a GI tract with respect to a reference coordinate system 5

2.1 A scheme of the cubic magnetic sensor array and its setup 10
2.2 Wearable sensing modules 11
2.3 A scheme of the magnetic motion sensing system 14
2.4 A permanent magnet mounted at the end-effector of a 6 DOF robot . 15
2.5 Measuring a rotational magnetic field generated by rotating a permanent magnet 17
2.6 Utilization of different electromagnetic waves for WCE localization . . 18
2.7 Eight RF receivers are placed on a patient's abdomen 20
2.8 A cubic antenna array and radiation pattern of RF signals transmitted by a RFID tag 22
2.9 Sequence of frames of WCE video in stomach and small bowel 24
2.10 Steps to calculate position and orientation parameters of an object using its projection on an x-ray image 25
2.11 Receivers placed on a patient's abdomen to detect ultrasonic signals emitted from a transducer integrated in a capsule 27

3.1 Process of positron emission and annihilation of a positron and an electron 31
3.2 Coincidence detection in a PET system 32
3.3 Three main types of coincidence events 33
3.4 A simple diagram of tracking positron emission sources 34
3.5 Coincidence lines arising from three markers in one localization time interval 35
3.6 Conceptual design of a PECapsule 36

3.7 Reduced geometry for capsule localization (left) compared to full-ring geometry for PET imaging (right). 38
3.8 Flow-chart of the tracking algorithm. 39
3.9 Translation vector for finding minimum distance point 41
3.10 Maximum radiation dose from the three markers to surrounding tissues. 48

4.1 Gamma rays are generated from a capsule inside a water phantom in a GATE simulation 53
4.2 A smaller detector system with two pairs of detector blocks placed 90° apart from each other 54
4.3 Design of the capsule simulated in GATE 55
4.4 Actions of the adder and reader modules in GATE 56
4.5 GATE simulation architecture 58
4.6 Computed 3D positions of the three markers in all localization runs . 58
4.7 Triangle center error in every localization run 59
4.8 Position error of each marker in every localization run with a histogram of the markers' position errors throughout all localization runs 60
4.9 An orientation vector of a PECapsule 61
4.10 Orientation error of the capsule in every localization run 61
4.11 Markers' position errors and computational time with and without failure prediction method 62
4.12 Average position error of the capsule over an entire dataset versus movement speeds of the capsule and phantom sizes 63
4.13 Coincidence lines collected by a small detector system and by a full-ring scanner 65
4.14 Average number of coincidence lines collected in each localization run by both scanners when different phantom diameters are simulated . . 67
4.15 An example of a mathematical phantom: MCAT phantom 69
4.16 An example of a voxelized phantom 69
4.17 3D renderings of male and female voxelized phantoms generated by XCAT v1.0 program 70
4.18 Visualization of the simulation with XCAT phantom 71
4.19 An intestinal section that the capsule moves inside in the simulation . 72
4.20 Gamma rays are generated from a capsule containing three ^{22}Na markers moving inside a XCAT phantom in a GATE simulation . . . 74
4.21 Computed 3D positions of the markers in all localization runs using data obtained from a voxelized phantom simulation, and 3D rendering of the GI tract of the XCAT phantom created by Amide software . . 75

4.22 Plots of position error of each marker, orientation error of the capsule, relative distances between the markers, and computational time in every localization run 77
4.23 Field of view of the reduced detector system 78

5.1 Design of the experimental capsule and markers 81
5.2 Design of the moving track 82
5.3 Overview of the experimental apparatus 83
5.4 An experimental apparatus is placed on the patient bed of a Philips TF64 PET scanner 84
5.5 A sketch of a PET scanner for conversion of crystal indices to XYZ coordinates 86
5.6 Number of true coincidence lines obtained in each localization run throughout 8-minute scanning by a TF64 PET scanner 88
5.7 3D trajectories of estimated positions and actual movement trajectories of the three markers on the same figure for comparison 90
5.8 Average position error of each marker and failure rates of the localization in different speed ranges of the capsule 91
5.9 Relative distance between any two of the three estimated markers when TF64 scanner is used 93

6.1 Three markers fixed on a capsule's cover form a rigid body 98
6.2 A simple diagram showing the principle of the tracking algorithm based on rigid-body transformation 99
6.3 An example of rigid-body transformation 100
6.4 Plots of position error of each marker, orientation error of the capsule, relative distances between the markers, and computational time in every localization run using a new tracking algorithm based on rigid-body transformation and voxelized simulation data 109

List of Tables

1.1 Main features of some commercially available WCEs 3

2.1 A comparison of key localization methods 28

4.1 Estimation error of each marker's position in each XYZ axis. 61
4.2 A comparison between the full-ring scanner and a small detector system in the number of total coincidence lines, the number of true coincidence lines, the true coincidence rate, and the average number of coincidence lines in each localization run when different phantom sizes are simulated. 65
4.3 Effect of decreasing average number of coincidence lines per run to below 210 on the tracking performance when the reduced geometry is used. 66
4.4 Main specifications of the voxelized phantom used in this study . . . 71
4.5 Specifications of the current UOW HPC cluster 74

5.1 Specifications of Philips Allegro PET scanner and Philips TF64 PET scanner 87
5.2 Average orientation error of the capsule in different speed levels of the capsule movement 92
5.3 Precision of the tracking algorithm by evaluating the position change of each marker in the periods when the capsule remained stationary at one position 94

6.1 A comparison between the previous algorithm and the new algorithm based on rigid-body transformation in terms of position error of the markers. Experimental data obtained from the Allegro scanner were used for the comparison 107
6.2 A comparison between the previous algorithm and the new algorithm based on rigid-body transformation in terms of position error of the markers. Experimental data obtained from the TF64 scanner were used for the comparison 108

List of Abbreviations

AOA — Angle of Arrival

BGO — Bismuth Germinate

CT — Computed Tomography

FOV — Field of View

GATE — Geant4 Application for Emission Tomography

GI — Gastrointestinal

GSO — Gadolinium Orthosilicate

HPC — High Performance Computing

LED — Light Emitting Diode

LOR — Line of Response

LSO — Lutetium Oxyorthosilicate

LYSO — Lutetium Yttrium Oxyorthosilicate

MCAT — Mathematical Cardiac-Torso

MMM — Magnetic Marker Monitoring

MRI — Magnetic Resonance Imaging

NN — Neural Networks

PCA — Principal Component Analysis

PET — Positron Emission Tomography

PHA — Pulse Height Analyzer

PMT — Photo-multiple Tube

RF — Radio Frequency

RFID — Radio Frequency Identification

RSSI — Received Signal Strength Indicator

SPECT — Single Photon Emission Tomography

SQUID — Superconducting Quantum Interference Device

TDOA — Time Difference of Arrival

TOA — Time of Arrival

TOF — Time of Flight

UOW — University of Wollongong

VQ — Vector Quantization

WCE — Wireless capsule endoscope

XCAT — 4D extended cardiac-torso

Abstract

Wireless capsule endoscope (WCE) is a first-line medical tool for the diagnosis of many gastrointestinal (GI) tract diseases such as obscure gastrointestinal bleeding, Crohn's disease, small bowel tumors, and Celiac disease. In the past few years, significant research attention has been dedicated to upgrading the WCE from a diagnostic-only tool to an active medical robot having not only diagnostic capabilities but also therapeutic functionalities such as biopsy, microsurgery, and targeted drug delivery. One of the major limitations that impedes the development of such a robotic-type endoscope is the lack of a highly accurate localization system. In this thesis, a novel localization method based on tracking multiple positron emission markers is presented. In the method, three spherical markers with diameters of less than 1 mm are embedded in the cover of an endoscopic capsule. Two pairs of gamma ray detector modules are arranged around a patient's body to detect coincidence gamma rays emitted from the three markers. The positions of the three markers, which refer to the position and orientation of the capsule, can then be determined using an effective tracking algorithm. The algorithm consists of four consecutive steps: a method to remove corrupted data, an initialization method, a clustering method based on the Fuzzy C-means clustering algorithm, and a failure prediction method.

In order to validate the proposed method, a simulation model of the localization system was developed using the GATE (Geant4 Application for Emission Tomography) toolkit. In this simulation study, both geometric phantoms and a realistic voxelized phantom generated by the 4D extended cardiac-torso (XCAT) software are simulated. After implementing the tracking algorithm in MATLAB, the simulation results show that the proposed method can achieve real-time tracking (computational time of 3-6 milliseconds for every localization time interval of 50 milliseconds) with an average position error of less than 0.4 mm and an average orientation error of less than 2°.

The tracking performance was then further evaluated using experimental data. An experimental apparatus was designed and fabricated using high-resolution 3D print-

ers to create a predefined track for the capsule to move along inside a water phantom. The experiments were conducted using two different commercial PET scanners: Philips Allegro and Philips TF64. The experimental results show good agreement with the simulations with an average position error of 0.5 mm and orientation error of 2.4° obtained.

In conclusion, this thesis has demonstrated the feasibility and potential of the proposed method in effectively determining the position and orientation of a robotic endoscopic capsule. In addition to producing high localization accuracy, the proposed localization method does not occupy any space inside the capsule or consume any power from the built-in battery. The method is expected to be compatible with any other actuation systems, especially the common magnetic actuation systems.

Acknowledgments

This thesis was made possible by the Ph.D. scholarship from the University of Wollongong Research Council, and was supported in part by the Intelligent Nano-Tera Research Systems Laboratory for which I am very thankful. Undertaking this PhD has been an amazing journey for me and it would not have accomplished without tremendous support and guidance I gratefully received from many people as highlighted below.

First and foremost, is a special thank to my principal supervisor Prof Gursel Alici, a very perceptive, creative and wise scientist. After more than three years being a PhD student, I have found that doing a PhD is very challenging in many ways that I have not previously expected. However, with the invaluable support, wise advice and persistent encouragement from Prof Gursel Alici, my PhD study was made much easier. Although being constantly busy due to daily administration work for the school, teaching and researching, he was always there to support and response to any requests that I made. The supervision I received from him gave me freedom and creativity in making decisions in my research. I am very grateful to be his student.

I would like to express my sincere appreciation to Dr Steven B. Harvey, my co-supervisor, for his massive help, excellent guidance and commitment in my research. Without his involvement and passion, the work presented in this thesis would not have evolved into such an interdisciplinary research. The experimental study was made possible by his great help in providing the phantoms and the radiation measurement devices, organizing the radioactive markers, contacting many technologists and scientists in the field of Nuclear Medicine for the experiment approval in using clinic PET scanners, and the transportation between Wollongong and Nepean and Austin Health hospitals. His help with English writing and proofreading is also exceptional.

I would like to thank all members of the Intelligent Nano-Tera Research Systems Laboratory, those who made this lab a great place to work, especially Prof Weihua Li for his support and encouragement. My gratitude goes to my colleagues: Dr

Chuc Nguyen, Hao Zhou, Dr Rahim Mutlu and Tongfei Tian for their friendliness, their help, and their cheerful and compassionate support throughout my adventure, especially during my not-so-good times.

I am grateful to staff at the Department of Nuclear Medicine and Centre for PET in Austin Health Hospital, Melbourne, Australia, and particularly Dr Graeme O'Keefe for his permission for conducting experiments using their Philips PET scanners, and his help with setting up and running the experiments. Without his invaluable corporation, the experiments would not have made achievable. I would also thank staff at the Department of Nuclear Medicine in Nepean Hospital, Sydney, Australia for their permission and technical assistance in conducting preliminary experiments. Thanks to technologists from Insight Oceania Pty Ltd, Australia, especially Tania Petts, for their help in seeking the right centre where the experiments can be conducted with accessible list-mode format.

I gratefully acknowledge the IT team in the Faculty of Engineering and Information Sciences, University of Wollongong for their assistance in setting up computer software throughout my PhD study. I would also like to acknowledge the University of Wollongong Information Technology Services (ITS) for computing time on the UOW High Performance Computing Cluster. Thanks to technicians in the Engineering Workshop for their help during the manufacture of the experimental apparatus. Thanks to lecturers in the RESH901 course (Fundamentals for HDR Writing) for their helpful lectures, and particularly Alisa Percy for her help with proofreading the literature review section in my first-year proposal review. I am grateful to Gate-users in the OpenGATE mailing list for their assistance in the GATE simulations, especially Marc Chamberland who was very helpful and friendly in answering my questions regarding to GATE and post-processing experimental data.

My sincere thanks to A. Prof Long Nghiem who introduced me to Prof Gursel Alici, which initiated this amazing adventure.

Last but not least, I would like to thank my parents, my sisters, my brothers-in-law, my nieces, and my nephews for their devoted love, for their unconditional support, and for their encouragements to pursue my doctoral degree. My heartfelt thanks to my girlfriend for her love, understanding and encouragement along this journey.

Chapter 1

Introduction

1.1 Wireless capsule endoscope

Endoscopy is a medical procedure used to examine and inspect the interior of a human body. According to a study conducted in 2002, approximately 19 million people in the United States were estimated to be affected by disorders of the small intestine [1]. It was reported by the World Health Organization that there were more than 1.4 million deaths caused by stomach and colorectal cancer in 2009 [2]. The American Cancer Society also reports that approximately 50,000 people die each year in the United States due to colorectal cancer [3]. These statistics indicate that effective advancements in endoscopy technology are extremely worthy of investigation.

In the 1960s when fiber optics were discovered [4], the flexible endoscope became a vital tool for diagnosing gastrointestinal (GI) diseases [5]. The conventional techniques for examining the GI tract adopt a long flexible tube with a light and a miniature

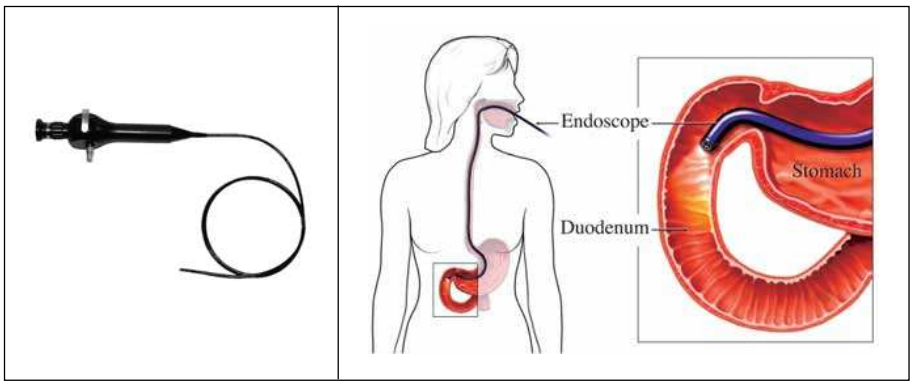

Figure 1.1: A conventional endoscope (left) and upper GI endoscopy (right) (www.drbhandari.com).

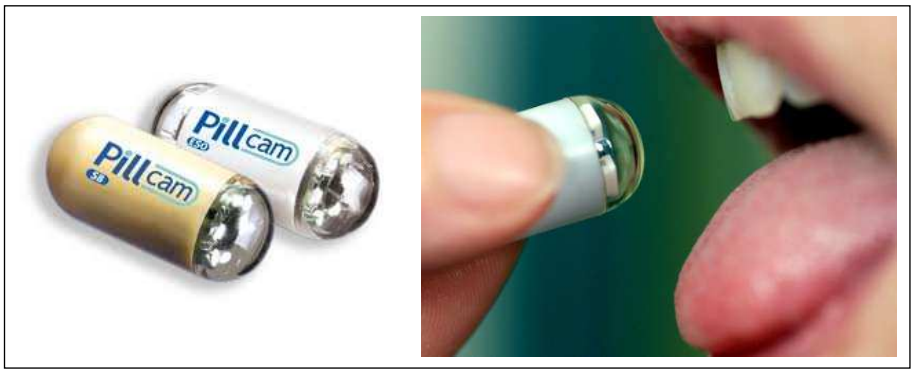

Figure 1.2: Pillcam endoscopic capsules and their small size that makes them swallowable (www.thehepcexperiment.com).

camera at the end as seen in Fig. 1.1. This equipment can be inserted through the mouth or the anus into the digestive tract. Owing to its rigidity and large diameter, it causes much pain and discomfort to whoever undergoes this procedure, especially when the endoscopists are not well skilled. This generally limits the willingness of the patients to have their GI tract examined by the technique. Furthermore, the lack of capability to reach the entire small intestine [6], which is the longest part, is also a significant shortcoming of the traditional wired endoscope.

Wireless capsule endoscope (WCE), a significant step in the efforts of developing a more effective endoscopy technique, was invented in 2000 to overcome the limitations [7]. WCE is an ingestible pill-like device that contains a tiny camera and an illuminating system for capturing images, and a transmission module for transmitting the images wirelessly to external receivers [8]. Being an innovative technique without cable connection, WCE offers a patient-friendly, non-invasive and painless investigation of not only the entire small intestine but also other GI parts [9, 10]. Figure 1.2 shows two commercial endoscopic capsules and their small size that makes them swallowable. To date, more than two million endoscopic capsules have been used all over the world [11].

Wireless capsule endoscope incorporates multi-disciplinary modules. As shown in Fig 1.3, the capsule contains 4 major components: a video camera, LEDs, batteries, and a radio-frequency (RF) transmitter. After the capsule is ingested, the camera captures a number of consecutive images of the interior of the entire GI tract during its passive travel by peristalsis. These images are sent to 8 external receivers mounted on the patient abdomen via RF communication at a frequency of 432 MHz. The received data are stored in a hard-drive connected to the receivers. At the workstation, the endoscopists can either view the pictures in real-time or download them from the hard-drive to a computer to review them later. It usually takes about 8 hours for the capsule to pass through the whole GI tract [9].

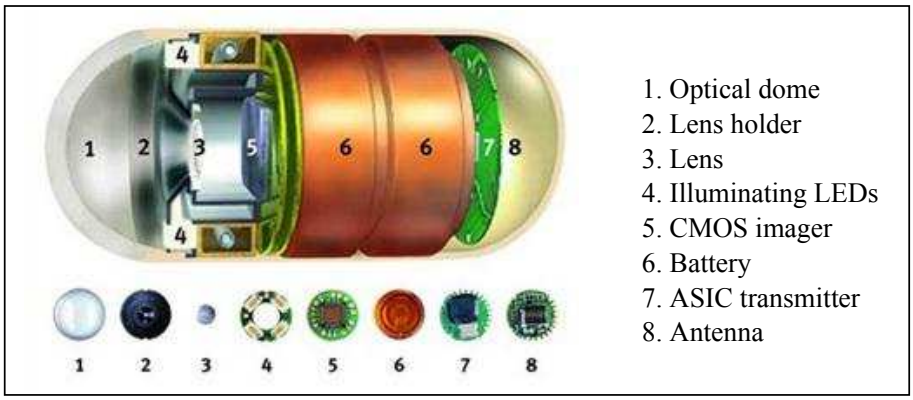

Figure 1.3: General structure of an endoscopic capsule [9].

The earliest commercial WCE, named M2A, was produced by Given Imaging Company. It has now been upgraded to Pillcam SB (or SB2). It was designed to work most effectively in the small intestine. In order to enhance the effect of the examination for the other parts of the GI tract, Given Imaging also produces Pillcam ESO (or ESO2) and Pillcam COLON (or COLON2) for the inspection of the esophagus and colon. Due to the structure of the esophagus, which is a muscular tube with a diameter of approximately 1.5-2 cm, the Pillcam ESO/ESO2 progresses faster in this area. Therefore, the camera of this capsule has much higher frame rates (up to 35 Hz) as shown in Table 1.1. On the other hand, since the operating time for this GI section is only a few minutes, the battery life time of the Pillcam ESO/ESO2 is very low (20 minutes). Pillcam COLON is designed to equip with two miniature cameras in both ends to increase the view of the entire internal surface of the large lumen in the colonic tract [12]. Beside the products of Given Imaging, EndoCapsule (from Olympus, Inc.), OMOM (from Jinshan Science and Techonology Group) and MiroCam (from Intromedic Co..,) are also currently available endoscopic capsules in medical clinics.

Table 1.1: Main features of some commercially available WCEs [13, 14].

	PillCam from Given Imaging						**Olympus**	**Jinshan**	**Intromedic**
	SB	SB2	ESO	ESO2	COLON	COLON2	EndoCapsule	OMOM	MiroCam
Size (LxD) (mm)	26x11	26x11	26x11	26x11	31x11	31x11	26x11	27.9x13	24x11
Camera	1	1	2	2	2	2	1	1	1
Frame rate (Hz)	2	2	14	18	4	4-35	2	2	3
View angle (degree)	140	156	140	169	156	156	145	140	150
LEDs	6	4	2x6	2x4	2x6	2x4	6	4	6
Real-time	Yes	Yes	Yes	Yes	Yes	Yes	Yes	Yes	-
Battery life	8 hours	9 hours	20 min	20min	10 hours	10 hours	8 hours	7-9 hours	11 hours
Target area	Small intestine	Small intestine	Esophagus	Esophagus	Colon	Colon	Small intestine	Small intestine	Small intestine

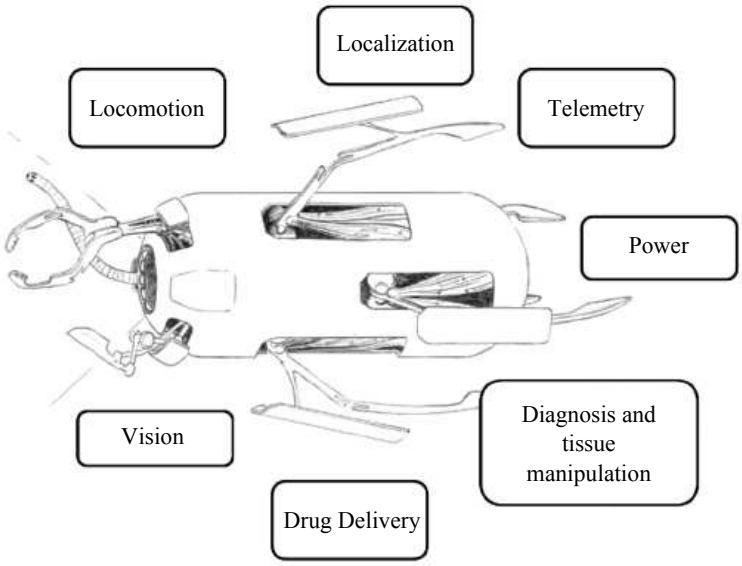

Figure 1.4: Schematic diagram of the possible modules of a future WCE [13].

1.2 Research problem

Since the introduction of the first WCE in 2000, this revolutionary technology has become an important field of research for engineers and physicians. It has been gaining substantial research attention recently, seen by the impressive number of studies on different aspects of WCE that have been published worldwide in the last ten years [15]. Current ongoing research studies are focusing on improving the diagnostic performance and upgrading the endoscopic capsule to a more powerful medical device that can carry out both diagnostic and therapeutic capabilities such as biopsy [16], micro-surgery and targeted drug delivery [17–19]. More specifically, the most active research areas include: enabling active actuation, developing sufficiently accurate localization, powering capsule wirelessly, improving the quality of endoscopic images, enhancing power efficiency/data rate of wireless telemetry, enabling intervention capabilities, etc. [12, 20]. The future robotic endoscopic capsule is thus expected to have seven possible modules as follows: locomotion, localization, telemetry, power, diagnosis and tissue manipulation, drug delivery, and vision, as seen in Fig. 1.4.

Developing a fully robotic WCE is a challenging task due to the most two major limitations of the current commercial WCE. Firstly, the capsule is unable to be accurately located when it travels along the GI tract. Therefore, although lesions can be detected by reviewing endoscopic images of abnormalities in the GI tract, their exact locations are unknown. Without a localization system, other important information for the diagnosis such as the distance that the capsule has traveled or the region of the GI tract in which the capsule is located is also missing or very

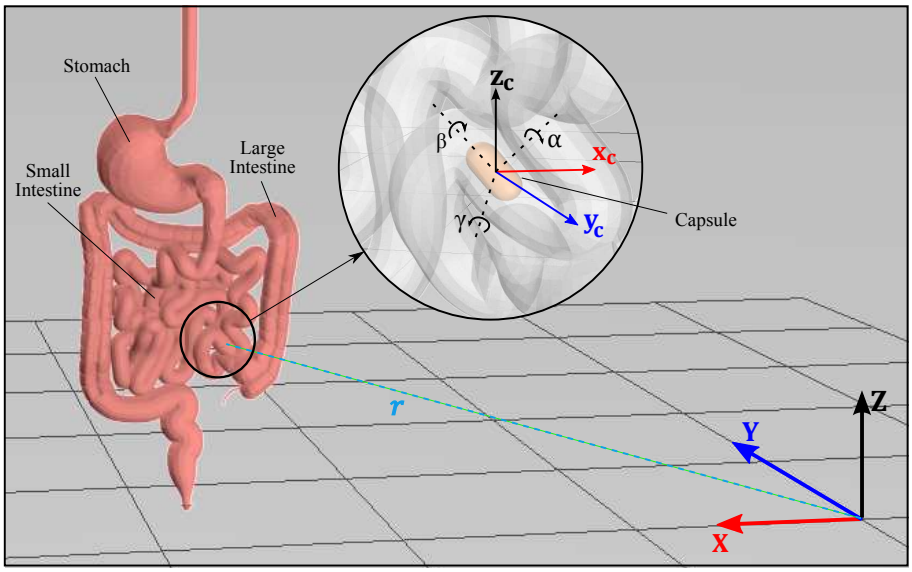

Figure 1.5: Position information (x_c, y_c, z_c) and orientation information (α, β, γ) of a capsule inside a GI tract with respect to a reference coordinate system (X, Y, Z).

difficult to estimate. This limits the diagnostic efficacy of WCE. More importantly, lack of the position and orientation data of the capsule (Fig. 1.5) also constrains the capability to return to the sites of interest for re-inspection or follow-up interventions such as drug delivery or surgical operations.

Another major limitation of WCE is that the capsule moves unpredictably and passively through the GI tract by means of natural peristalsis and gravitational effects. Therefore, the capsule is unable to stop, to turn or accelerate, resulting in potential issues such as missing symptoms or capsule retention. In addition, it is impossible to perform a biopsy or drug delivery when the capsule movement is uncontrollable. Active locomotion is thus a vital requirement for the next generation of WCE. This again emphasizes the necessity of having an accurate localization system for WCE as localization is essential to provide a prompt feedback with any position/orientation control systems. As an example, one of the most popular methods for controlling the movement of the capsule is to use an external magnetic field to move or rotate an internal permanent magnet integrated inside the capsule [4, 21]. In this method, the position and orientation data are essential to align or maintain a stable link between the external magnetic field and the internal magnetic field; and to control the strength and direction of the external magnetic field.

1.3 Research aim and research objectives

The aim of the research presented in this thesis is to develop an effective localization method for robotic endoscopic capsules that can deliver high tracking performance in

real-time. As reported in the literature and explained in detail in Chapter 2, none of the currently studied research could offer a complete solution. The techniques which have potential to provide high accurate localization data are either influenced by the magnetic field to be used for actuation or introducing long-term risk for the patient due to radiation exposure. Therefore, the proposed method is required to meet other two following key properties: minimally invasive, and compatible with different actuation systems, especially the magnetic actuation systems. The proposed method will be validated using both simulation and experimental studies.

Based on the above research aim, the specific research objectives for this work are as follows:

- To establish and develop a minimally invasive localization method that can determine accurately the position and orientation of the capsule in real-time without being interfered with other systems, especially the magnetic actuation systems.
- To develop a tracking algorithm in Matlab that can extract the localization information from the data obtained by the receivers/detectors or sensors.
- To build simulation models in a computer software to validate the proposed method, and to evaluate the tracking performance.
- To design and fabricate an experimental setup/apparatus so that experiments can be conducted to test/validate the proposed method, and to experimentally evaluate the tracking performance.
- To optimize the tracking algorithm to enhance the localization performance.

1.4 Thesis structure

The work undertaken to meet the objectives in this thesis is presented in seven chapters as follows:

- Chapter 1 provides an overview of the wireless capsule endoscope and its limitations that need to be addressed. The research aim and objectives are identified in this chapter.
- Chapter 2 presents a comprehensive review of the previously proposed localization methods. The benefits and drawbacks of the methods are compared and discussed.
- Chapter 3 describes the principle of operation and the conceptual system de-

sign of the novel localization method proposed in this thesis. The tracking algorithm is also developed in this chapter.

- Chapter 4 evaluates the tracking performance of the proposed method when simulation models of the localization system are built in GATE v6.2. Geometric phantoms and a realistic voxelized phantom (XCAT phantom) are respectively employed for the simulations.
- Chapter 5 describes the design of the experimental apparatus and the experimental procedures. The performance of the tracking algorithm is then evaluated using the obtained experimental data.
- Chapter 6 covers the development of a new tracking algorithm based on rigid-body transformation. The benefit of the new tracking algorithm is then evaluated and explained.
- Chapter 7 provides a critical discussion about the proposed localization method, limitations of the research work, main contributions of the study, and recommendation for future development. A conclusion is also drawn in this chapter.

Chapter 2

Literature Review

The methods for determining the capsule's position and orientation that have been investigated so far are categorized into two groups: magnetic-field based methods and electromagnetic-wave based methods [22].

2.1 Localization methods based on magnetic field

In the last decade, magnetic tracking methods for WCE localization have attracted the attention of researchers, as compared to other methods, for two main reasons. Firstly, static and low-frequency magnetic signals can pass through human tissue without any attenuation [23]. Secondly, magnetic tracking is a non line-of-sight method, in which the capsule does not need to be in the line of sight with magnetic sensors in order to be detected [24].

The advantage of the negligible interaction between the magnetic field and the human body is not only exploited by those who are interested in localization systems, but also by those who focus on actuation systems. This is proved by a number of current efforts trying to design actuation systems that can guide endoscopic capsules magnetically such as robotic magnetic steering [25–27], helical propulsion by a rotational magnetic field [28–31], magnetic levitation [32, 33], remote magnetic manipulation [34], and so on. Therefore, there would be an interference problem between two applied magnetic fields when both magnetic localization and magnetic actuation are operated.

Some research groups have introduced methods that can avoid this conflict problem, whereas others seem to ignore the influence of the magnetic actuation. The tracking systems in this category are thus classified into two sub-groups: magnetic localization for passive endoscopic capsules and magnetic localization for magnetically

actuated capsules.

2.1.1 Magnetic localization for passive endoscopic capsules

The two most important components in a magnetic tracking system are a magnetic source and a sensor module. Depending upon how the magnetic source is created and whether the capsule acts as a field generator or a sensing module, the localization systems in this group are divided into three subsections as follows

2.1.1.1 Utilization of a permanent magnet enclosed inside a capsule

A stable and reliable source of magnetic field is essential for any real-time magnetic tracking system. A permanent magnet is such a source. Thanks to its capability of creating a steady magnetic field without batteries. The majority of the magnetic tracking systems generate magnetic field through integrating a permanent magnet inside the capsule.

The magnetic flux originating from the magnet vary their magnitudes and directions depending on the magnet's location and orientation. To measure these persistent magnetic signals, magnetic sensors are placed around the patient's body. Based on the geometry of the small magnet, equations that represent the relationship between magnetic field strengths measured by the sensors and the position and orientation of the magnet can be established. Since the size of the magnet is much smaller than the distance from the magnet to the sensors, the magnet is assumed to behave as a magnetic dipole. The magnetic flux intensity around the magnet can be expressed by the following formula [35]

$$\vec{B} = B_x\vec{i} + B_y\vec{j} + B_z\vec{k} = \frac{\mu_\circ}{4\pi}\left(\frac{3\left(\vec{m}\cdot\vec{r}\right)\vec{r}}{\left|\vec{r}\right|^5} - \frac{\vec{m}}{\left|\vec{r}\right|^3}\right) \tag{2.1}$$

where B_x, B_y, B_z are the three components of the magnetic flux intensity, $\vec{m}$ is the magnetic dipole moment of the magnet, $\vec{r}$ is the position vector of the magnet, and $\mu_\circ$ is the air magnetic permeability ($4\pi \times 10^{-7} JA^{-2}m^{-1}$). From (2.1), it is possible to compute the localization parameters of the magnet, which are also referred to those of the capsule, by solving inverse equations using an appropriate optimization algorithm.

One of the earliest systems that have employed such a technique for monitoring the gastrointestinal transit of a capsule is the tracking system presented by Weitschiles et al. [36,37]. The Magnetic Marker Monitoring (MMM) implemented in their method

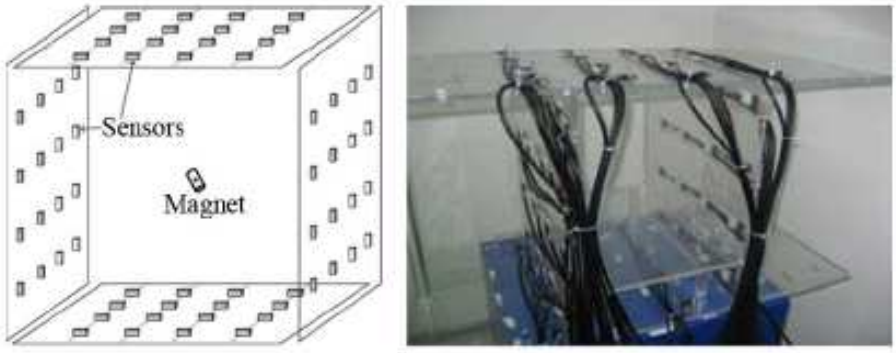

Figure 2.1: A scheme of the cubic magnetic sensor array and its setup [23].

utilized a 37-channel, Superconducting Quantum Interference Device (SQUID) sensor system above a volunteer's abdomen. The position resolution was recorded as within a range of millimeters. However, the monitoring procedure had to take place in a magnetically shielded room to reduce the magnetic noise from the surrounding environment. In addition, orientation data of the capsule were not considered.

Taking this into account, Schlageter et al. [38, 39] introduced an approach using a 2D-array of sixteen Hall sensors to determine both position and orientation of a pill-size magnet coated with silicone. When the magnet with a volume of 0.2 cm^3 moved within a distance of 20 cm from the sensor plane, its position and orientation parameters could be displayed in real-time at the rate of up to 20 Hz. Since the magnetic field strength decreases rapidly as the distance increases (due to their inverse third power relationship), moving the magnet away from the sensor array leads to a significant drop in the system's accuracy. Therefore, enlarging the localization coverage is one of the most desirable improvements for this method. Increasing the size of the magnet seems not a possible solution due to the size limit of the available space inside the capsule.

Adopting the idea of using a 2D magnetic sensor array, Chao et al. [23] increased the tracking coverage by developing a 50 cm $\times$ 50 cm $\times$ 50 cm cubic sensor array instead of only one sensor plane. This cubic sensor array is formed by two pairs of facing sensor planes, as seen in Fig. 2.1. On each of the four sensor planes, they installed sixteen 3-axis magnetic sensors (Honeywell HMC1043) in a fixed uniform interval. The system achieved an average position error of 1.8 mm and orientation error of 1.6° when the capsule (carrying a cylindrical magnet with a size of $\phi 5$ mm $\times$ $L6$ mm) moved in the inner space of the sensor cube. Although the accuracy and the tracking coverage of the system were improved noticeably, adding three sensor planes would quadruple the cost and the complexity of the system.

In terms of cost, Aziz et al. [40] proposed a tracking system that employed only three 3-axis Honeywell sensors (HMC2003) placed orthogonally in 3D space and an extra

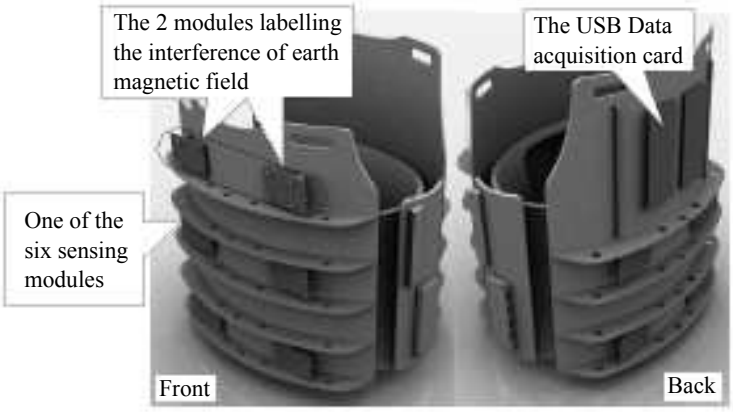

Figure 2.2: Wearable sensing modules by Wu et al. [41].

sensor for canceling environmental magnetic noise. However, due to the system simplicity and insufficient measurement data, this technique could not provide a reasonable accuracy. An error of up to 3 cm occurred when a $\phi 5$ mm $\times$ $L6$ mm cylindrical magnet was tested in a volume of 10 cm $\times$ 10 cm $\times$ 10 cm.

In terms of portability and flexibility, on the other hand, Wu et al. [41] built a wearable magnetic tracking system that could allow the patients to make basic movements with different postures during diagnostic procedures. They designed a wearable vest with a coverage of approximately $L40$ cm $\times$ $W25$ cm $\times$ $H40$ cm. The vest consists of six sensing modules at the front frame and the other four at the back frame, as shown in Fig. 2.2. Each module is composed of six linear Hall-effect sensors (A1321) forming 3 pairs of back-to-back sensors arranged perpendicularly to each other in 3D space. By this arrangement, each pair is responsible for measuring one dimension of the magnetic field. The top two modules at the front were used to eliminate the interference of the earth magnetic field. Using a small cylindrical magnet ($\phi 5$ mm $\times$ $L3$ mm) embedded inside a capsule, the position error was reported as below 10% when they performed trial tests on volunteers. Since the localization algorithm is based on the mathematical model of a magnetic dipole, when the capsule is close to the sensing module, this model is no longer correct, which results in a decrease in the system's accuracy.

2.1.1.2 Utilization of a secondary coil embedded in a capsule

Alternatively, the spatial information of the capsule can be obtained by using a coil enclosed inside a capsule. The idea of tracking a receiving coil by a large 2-D array of transmitting coils was first proposed by Plotkin and Paperno [42,43]. It was then also exploited in the commercial Aurora tracking system [44]. In this technique, the

field seen by the receiving coil is given by

$$\vec{B}_r = \vec{B}_t \cdot \vec{M} \tag{2.2}$$

where $\vec{M}$ is the magnetic moment of the receiving coil, $\vec{B}_t$ is the magnetic flux intensity generated by the transmitting coil. Since $\vec{B}_t$ can be expressed approximately by (2.1), computing the localization data in this case is similar to that of a permanent magnet. In other words, an optimization algorithm, such as Levenber-Marquardt, could be employed to solve the inverse equations for (2.2) once the electromotive force induced in the receiving coil is measured.

Applying the idea to WCE, Nagaoka and Uchiyama [45] designed a single-axis coil made by 160 turns copper wire with a size of ϕ6.5 mm $\times$ L2.3 mm to be inserted into a capsule. A magnetic field generator, placed outside of the patient's body, generated five alternating magnetic fields operating at five different frequencies. The electromotive forces, created by mutual induction, in the coil were measured to calculate the coil's position. Since the magnetic field strength decreases proportionally to the inverse third power of the distance between the primary coils and the secondary coil, the current flow in the primary coils was controlled to ensure the induced electromotive forces are always within a predetermined range. Although it was reported that the system demonstrated an accuracy of 5 mm when the capsule was up to 500 mm far away from the generator, the experiment failed at several locations.

2.1.1.3 Utilization of a 3-axis magneto-resistive sensor mounted inside a capsule

Contrary to the methods in which a permanent magnet or a coil is employed, Guo et al. [46] developed a different solution for the localization problem by sealing a 3-axis magneto-resistive sensor (HMC1023) inside a capsule. The purpose of the sensor is to measure the external magnetic fields generated by three energized coils placed on the patient's abdomen. The three coils are excited in turn by square waves with the same period of 0.03 s. At the end of every cycle, there is a break period of 0.1 s in which the coils are not excited to measure the earth magnetic field. Based on the measured data by the sensor, the position and orientation of the capsule can be computed using a neural network algorithm. When the sensor is close to the coils (less than 50 mm), the magnetic dipole assumption fails, which causes a significant error in the experimental results. Therefore, an improved localization model based on Biot-Savart Law was proposed to replace the magnetic dipole model [47]. The position errors reported vary from 6.25 mm to 36.68 mm, corresponding to orien-

tation errors of between 1.2° and 8.1° when the tracking distance was up to 0.4 m. In addition to the effort of improving the method, this group also conducted alternative experiments which employed eight energized coils excited by sinusoidal signals instead of square waves [48]. The experimental results computed by an adaptive particle swarm optimization shown an average position error of 14 mm and an average orientation error of 6.9°.

2.1.1.4 Discussion

Despite the aforementioned advantages of the magnetic tracking, the magnetic localization systems presented in Section 2.1.1 have some common drawbacks. To begin with, the devices or equipment nearby the tracking systems needs to be made of non-ferromagnetic materials. A small piece of a ferromagnetic bar unintentionally inserted into the detecting area could lead to a failure in locating the capsule [49]. Secondly, due to the size constraint of the capsule to be swallowable, the limit in tracking coverage is also a significant disadvantage. Last but most importantly, as previously stated, the question of how to remove the interference between magnetic localization and magnetic actuation is still to be answered. Making use of time division, i.e. alternately switching on or off between the actuation and sensing, has been suggested to solve this problem [14]. However, due to the hysteresis characteristics, real-time tracking would not be achieved as the magnetic localization system would have to wait until the magnetic field for actuation has completely vanished. Moreover, during the off period of the magnetic actuation, the capsule may move to a different position and orientation. For these reasons, the tracking system will not be able to provide accurate feedback data for the actuation system. Other solutions for this problem are discussed in detail in the next section.

2.1.2 Magnetic localization for magnetically actuated capsules

In the previous section, the localization methods were developed in the absence of a magnetic actuation system. In this section, magnetic localization systems that were designed to work compatibly with magnetic actuation mechanisms are discussed.

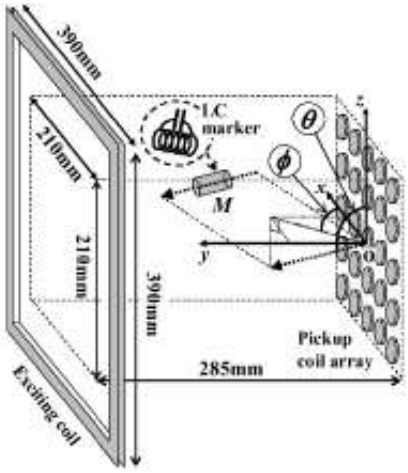

Figure 2.3: A scheme of the magnetic motion sensing system by Hashi et al. [51].

2.1.2.1 Localization method based on high-frequency alternating magnetic field

For actuation, the Olympus group [50] assembled a spiral structure on the surface of a capsule. Three pairs of Helmholtz's coils were placed in three perpendicular directions around the patient's body to generate an external rotating magnetic field. Having a permanent magnet inside, the capsule can be rotated by this external magnetic field. Thanks to the spiral structure on the capsule body, the capsule is thus propelled forward or backward depending on the direction of the current flow in the coils.

To avoid causing pain and discomfort to the patient, the capsule is not allowed to move too fast along the GI tract. The frequency of the external rotating magnetic field should thus be lower than 10 Hz [50]. Due to the fact that the low frequency (several Hz) rotating magnetic field does not influence a high frequency (from 1 kHz to 1 MHz) alternating magnetic field, the Olympus group employed the latter for localization. For this purpose, excitation coils were built around the patient's body to produce the high frequency magnetic field. The operating frequency used in this system was chosen in the range of 1 kHz to 1 MHz to prevent absorption by living tissue. As a magnetic field is induced in the small resonating coil embedded inside the capsule, detecting coil arrays were also placed around the patient to measure this induced magnetic field. The total magnetic field measured by the detecting coil arrays is given by

$$\vec{B}_{total} = \vec{B}_{excitation} + \vec{B}_{resonant} \tag{2.3}$$

where $\vec{B}_{excitation}$ is the magnetic field generated by the excitation coils, and $\vec{B}_{resonant}$ is the magnetic field induced in the small coil. From (2.3), $\vec{B}_{resonant}$ can be calculated by subtracting the magnetic field generated by the excitation coils $\vec{B}_{excitation}$ from the

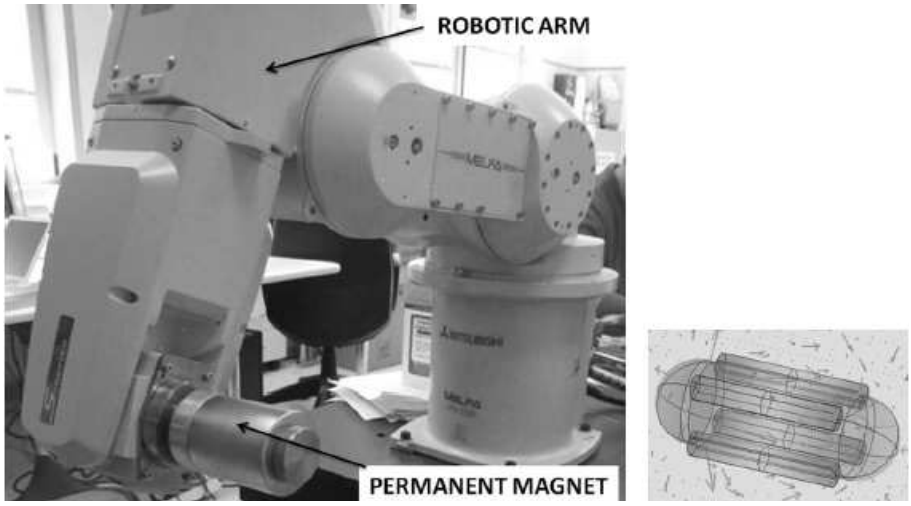

Figure 2.4: A permanent magnet mounted at the end-effector of a 6 DOF robot, and 4 cylindrical permanent magnets sealed on a capsule body [25].

measurement magnetic field $\vec{B}_{total}$. Since $\vec{B}_{resonant}$ is dependent on the position and orientation of the small coil, it is possible to estimate the localization information of the capsule. As reported in [51, 52], this technique could achieve a detection accuracy of a sub-millimeter order when the resonating coil (shown as a LC marker in Fig. 2.3), was placed within the distance of 120 mm from the detecting coil array. The marker has a diameter of 3 mm and a length of 10 mm with 250 turns. In this motion capture system, the detecting coil array, which is located 285 mm from the excitation coil, is composed of 25 pick-up coils positioned at 45 mm intervals. The resonant frequency was 306 kHz.

A similar idea of using a high frequency alternating magnetic field to solve the interference problem between magnetic actuation and magnetic localization was also introduced by Graummann [53]. However, instead of an integrated coil, a detector was inserted inside the capsule to measure the high frequency magnetic field. The measurement data were then sent to an external receiver by a transmitter unit for post processing the localization data of the capsule. Compared with the Olympus tracking system, this system consumes more power and space as an additional microcontroller unit and a transmitting unit were added to the capsule.

2.1.2.2 Localization method based on inertial sensing

Another way to propel the capsule is via magnetic steering. Ciuti et al. [25] utilized a 6 degree-of-freedom (DOF) robotic arm carrying a permanent magnet attached at its end-effector as shown in Fig 2.4. Four cylindrical magnets were mounted uniformly on the capsule body to create a magnetic link between the capsule and the external permanent magnet. The capsule can thus be dragged and steered by the robotic

arm. The steering is only effective when the internal magnets are aligned properly with the external magnets. Therefore, the capsule's position and orientation data are important to ensure a reliable magnetic link between the two magnets.

To locate the capsule, a 3-axis accelerometer LIS331DL was inserted into the capsule. At first, a rough position estimate was obtained by magnetic scanning which involves moving the end-effector above the patient's trunk to find the internal magnets. When the external magnet is close enough to the internal magnets, the internal magnets are lifted towards the end-effector by a magnetic attraction force. This sudden action is recognized since it results in an acceleration pulse on the output plots of the sensor. Next, pitch and roll data obtained from the inertial sensor are used for orientation alignment between the capsule and the external magnet. The alignment is considered as completed when any angular changes to the end-effector lead to an equivalent movement in the capsule. It is reported that the sensor could provide an orientation accuracy of 6°.

In this system, the conflict issue between actuation and localization does not exist. Instead, the actuation apparatus is also involved in locating the capsule. Nevertheless, it would be hard to make a capsule compact enough to be swallowable with the integration of an inertial sensing subsystem and four cylindrical magnets. Additionally, this localization technique only offers rough spatial information (an average error of 3 cm) without data on the vertical direction.

2.1.2.3 Localization system based on measuring the magnetic field generated for actuation

Similar to the idea of the Olympus group, Kim et al. [54] also created an external rotational magnetic field to rotate an endoscopic capsule equipped with a helical structure on its body. However, instead of utilizing the six bulky coils, the rotational magnetic field was produced by rotating a big parallelepiped permanent magnet consisting of seven smaller rectangular magnets. This magnetic field generator was driven by an electrical motor mounted on a manipulator so that it could rotate and be moved while propelling the capsule as shown in Fig. 2.5.

One notable feature of this system is that the external magnetic field generated for actuation was also exploited for localization. Three Hall-effect magnetic sensors (A1391) were set up orthogonally inside the capsule for this purpose. An extra sensor was installed on the other side of the main axis of the capsule (as seen in Fig. 2.5) to remove the offset effect and hence improve the tracking accuracy.

When the external permanent magnet spins, the magnetic flux strength at the cap-

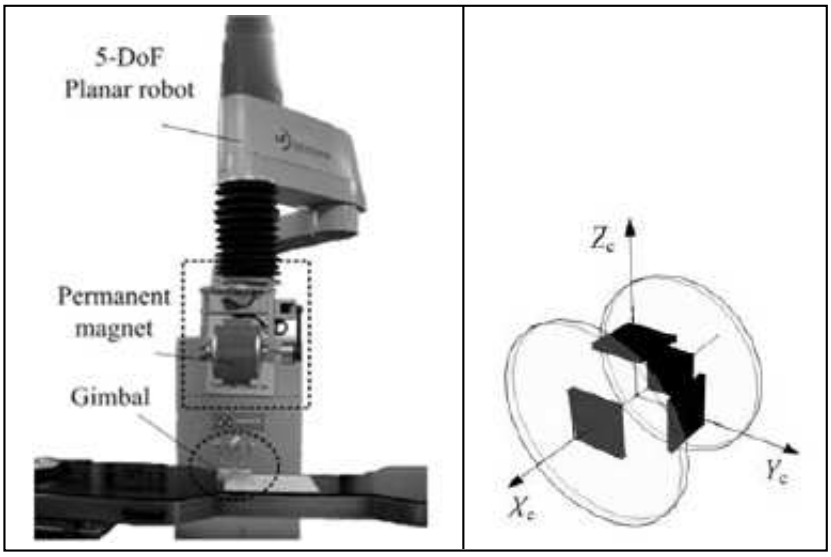

Figure 2.5: A sensor module integrated inside a capsule (right) to measure a rotational magnetic field generated by rotating a permanent magnet (left) [54].

sule location changes periodically. Its highest/lowest value is reached when the capsule lies on the XZ/XY plane. Therefore, by solving the magnetic flux density equations in these two special cases, the capsule position data can be determined. Then, a rotation matrix, which represents the capsule's orientation, is acquired by comparing the three calculated orthogonal components of the magnetic flux with the three measured orthogonal components at the located position. This localization method generated x,y,z position errors within the ranges of (+2 mm, +15 mm), (-9 mm, +12 mm) and (-10 mm, +3 mm), respectively. The orientation errors were within the range of $(-2°, +13°)$ in pitch direction and $(-4°, +11°)$ in yaw direction.

Other similar approaches, which also take advantage of the external magnetic field generated for actuation to localize the capsule, include: enclosing six one-axis Hall-effect sensors in the capsule [55]; using only one 3-axis magnetic sensor [56]; or utilizing Hall-effect sensors combined with a tri-axial accelerometer [57]. A common drawback of these methods is space requirement to install such cumbersome localization mechanisms inside the capsule. In fact, the currently available capsules are already highly compact [58].

2.1.2.4 Discussion

Among the localization methods presented in Section 2.1.2, the Olympus's method provides higher compatibility to work with other actuation systems. However, to achieve accurate 5D tracking (including 3D position, pitch and yaw data), three pairs of facing excitation coils and three pairs of facing detecting coil arrays in three

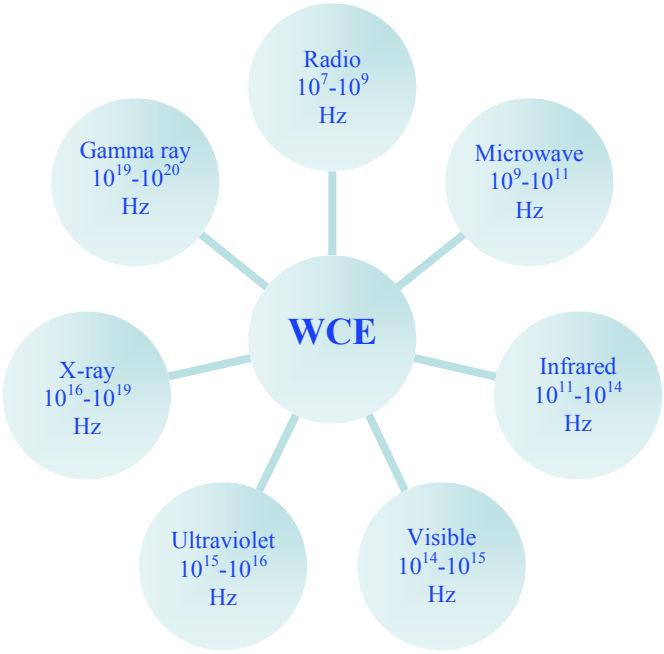

Figure 2.6: Utilization of different electromagnetic waves for WCE localization.

perpendicular directions need to be built around the patient's body. Together with the three pairs of coils to generate a rotating magnetic field for actuation, they would make the entire system complex and bulky. On the other hand, although the other systems can achieve necessary localization information to some extent without being interfered with their actuation systems, it is likely that they will not be able to deliver the same results when being applied to other actuation systems. In fact, it is still not certain that magnetic steering or rotating external permanent magnet will be the future actuation methods. Therefore, developing a more versatile and compact localization method is still necessary.

2.2 Localization methods based on electromagnetic waves

To obtain an accurate knowledge about the location of an object placed inside a narrow and complex medium like the GI tract, the object needs to be in physical contact with different types of signals from the external world. In addition to the methods based on magnetic field that have been introduced above, localization methods that employ electromagnetic waves are presented in this section. The common advantage of these approaches is that they are not affected by the magnetic fields generated for actuation.

As shown in Fig. 2.6, the electromagnetic spectrum includes the seven following

regions: radio, microwave, infrared, visible, ultraviolet, x-ray and gamma ray. However, only radio waves, visible waves, x-ray and gamma ray have been exploited for capsule tracking. Microwaves, infrared waves and ultraviolet waves have very low penetrability through the human tissues.

2.2.1 Radio waves

Radio frequency (RF) radiation has been widely used for locating an object in both outdoor and indoor environments with an accuracy of hundreds of millimeters [59]. However, applying RF in localizing an object within such a complex environment as the GI tract is a challenge. This is due to the fact that high frequency signals suffer significant attenuation at different levels when they pass through different living tissues, and low frequency signals due to their long wavelengths are not able to deliver the desired precision of several millimeters [60]. The traditional tracking techniques using RF include: received signal strength indicator (RSSI), angle of arrival (AOA), time of arrival (TOA), time difference of arrival (TDOA), and radio frequency identification (RFID). Since radio waves travel with a very high speed (3×10^8 m/s), an extremely strict time synchronization of less than 1 ns is required in order to obtain a position resolution of 0.3 m. Time based methods are thus not feasible for WCE localization. Likewise, AOA are inapplicable in the digestive tract conditions due to its low reliability even in indoor environments [61, 62]. Therefore, only RSSI and RFID have been investigated for the capsule localization.

2.2.1.1 Received signal strength indicator (RSSI)

The new generation of endoscope is called "wireless" capsule endoscope as it is equipped with a telemetry capability, which is one of the most important functions that make WCE an innovative technique compared to the previous generation. A transmitter built inside the capsule wirelessly sends endoscopic images to eight receivers placed uniformly on the patient's abdomen as shown in Fig. 2.7. Taking advantage of this telemetry function, Fisher et al. [63, 64] measured the strength of the RF signals received at the eight sensors in order to estimate the position of the capsule. The tracking algorithm is based on the observation that the closer the receiver is to the transmitter, the stronger the signal it receives. When two adjacent antennas receive equal strength signals, the capsule is assumed to be approximately between them. One advantage of this method is that it does not require additional elements in the capsule. However, the above assumption is not always true due to noise and the complex RF absorption properties of the human tissues [64]. This

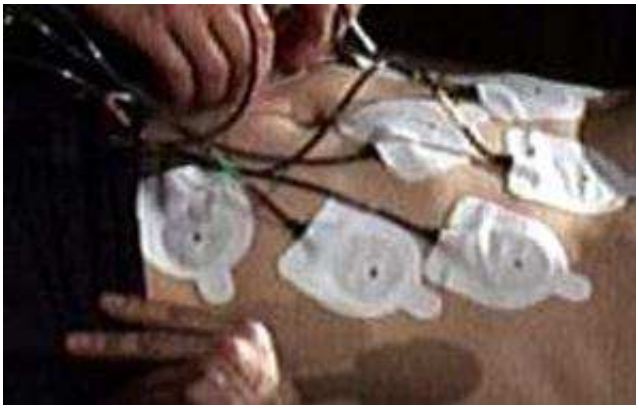

Figure 2.7: Eight RF receivers are placed on a patient's abdomen to receive the endoscopic images (www.sciencephoto.com).

localization technique, which is being used in the commercial Given Imaging M2A capsule, is thus only able to estimate 2D position information with an accuracy of 3.77 cm.

In addition to the efforts of developing a tracking system using RSSI, Arshak and Adepoju [62] applied an empirical signal propagation model, which has been widely used in RF localization, to estimate the capsule's position. This model describes the mathematical relationship between the RSSI value and the distance from the transmitter to the receiver [65]:

$$RSSI(d) = P_T - PL(d_\circ) - 10n \log_{10} \frac{d}{d_\circ} + X_\sigma \tag{2.4}$$

where d is the distance between the transmitter and the receiver, P_T is the transmit power, $PL(d_\circ)$ is the path loss for a reference distance $d_\circ$, n is the path loss exponent, X_σ is a Gaussian random variable. From (2.4), the distances between the capsule and each of the sensors can be estimated using the RSSI measurement data. Trilateration method is then employed to calculate the capsule location based on the estimated distances from the transmitter to all the receivers. It is reported that an average error of approximately 25% of the tracking distance was observed.

Instead of using a signal propagation model, Shah et al. [66] presented an algorithm based on a look-up table for the position estimation. Offline measurement was carried out first, in which at each position of the capsule, both signal strength measured by each of the sensors and 2D position data were recorded in the table. During the experiment, online data was compared with the data stored in the table to find the closest match and hence to estimate the capsule position.

A propagation attenuation model plays a vital role in the RSSI technique. The empirical model mentioned above is not accurate enough in the complex environment

of the GI tract. In order to reduce the position error of this localization method, it is necessary to develop a more appropriate attenuation model when RF signals pass through a human body. Lujia et al. [67, 68] took into account not only the distance dependence of the signal strength, but also the influence of the antenna orientation and tissue absorption to build a compensated attenuation model. However, the accuracy of this model has not yet been tested in WCE tracking. On the other hand, Yi et al. [69] compared the impact of different organs and sensor-array topology on the position error. It is reported that when there is only one 4x4 sensor array, the location errors are up to 52 mm, 65 mm, and 110 mm in the small intestine, in the stomach and in the large intestine, respectively. However, when two 4x4 sensor arrays are available, these maximum location errors are decreased to 40 mm in the small intestine, 42 mm in the stomach and 55 mm in the large intestine.

2.2.1.2 Radio frequency identification (RFID)

Beside the RSSI technique, RFID has also been investigated for the localization of WCE. A cubic antenna array is built surrounding a patient's body to track a RFID tag integrated inside a capsule. At first, the tracking algorithm was based on an assumption that the tag is only detected by the closest antennas [70]. The IDs of the antennas that have detected the tag are collected to estimate the tag's position. Using the center of gravity principle, the position of the tag, which refers to that of the capsule, can be determined. However, due to the inaccuracy of the center of gravity principle, this tracking algorithm produced large errors.

Therefore, an improved method was proposed in [71, 72]. In this method, the tag consists of a bidirectional antenna that can transmit RF signals in two opposite directions. After receiving a wake-up signal from a RFID reader, this active tag sends a reply signal to the cubic array. Since the radiation pattern is bidirectional, some antennas in two opposite faces of the cubic array receive the reply signal as shown in Fig. 2.8. These antennas form two traces on the two opposite faces. Based on the shape and the position of the traces, the position and orientation of the tag can be estimated by a matching algorithm. Although it is reported that the system achieves errors of 0.5 cm in x and y directions and 2 cm in z direction via computer simulations, this method does not seem practical to apply. In order for the RF signals to pass through the human body, the operating frequency is limited below the UHF band. In this band, it is impossible to generate directional radiation by a compact antenna with less than 1 cm in length. Another drawback of this system is that when the longitudinal axis of the tag's antenna is in the same direction with the main axis of the patient, the radiation pattern does not intersect the cubic array,

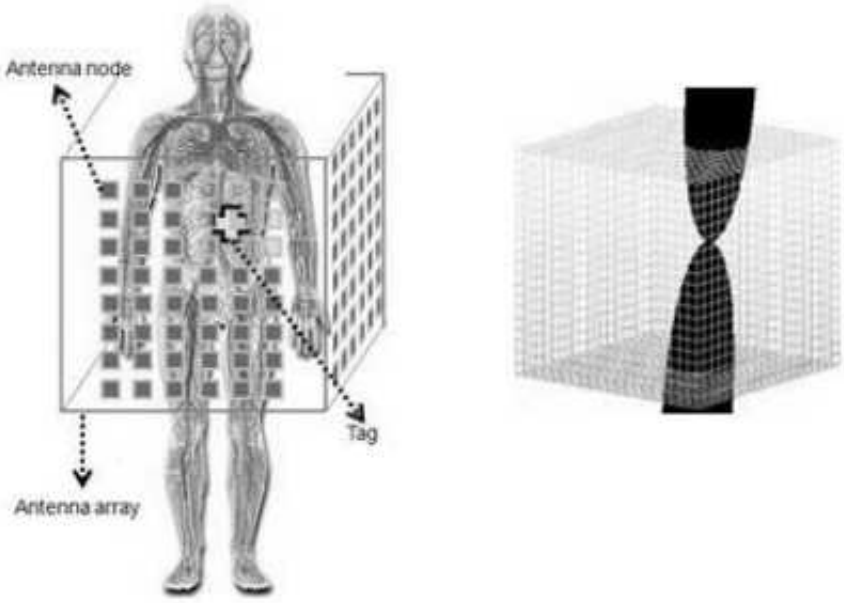

Figure 2.8: A cubic antenna array and radiation pattern of RF signals transmitted by a RFID tag [71].

and thus the matching algorithm will not be able to determine the position of the capsule. To solve this problem, at least one more tag in a perpendicular direction with the first tag may be needed in the capsule.

Another method for the localization of a RFID tag placed in a capsule is based on phase difference. In a system with one transmitter and several receivers, the RF waveforms at the i^{th} receiver is given by the following equations [73]

$$I_i(t) = A_i \cos\left(2\pi(f_r - f_c)t + \phi_i\right) + \sigma_i n_{i1} \tag{2.5}$$

$$Q_i(t) = A_i \sin\left(2\pi(f_r - f_c)t + \phi_i\right) + \sigma_i n_{i2} \tag{2.6}$$

where I(t) and Q(t) are the inphase and quadrature components of the signal; A, f_r, f_c, ϕ, σ, and n denote the received signal magnitude, the frequency at the receivers, the carrier frequency, the phase difference between the carrier at the tag and the carrier at the receiver, the noise level, and Gaussian noise, respectively. Hekimian-Williams et al. [73] showed that although exact phase value (ϕ_i) of a single signal received at an antenna cannot be used to calculate the distance that the signal has traveled, the phase difference ($\phi_i - \phi_j$) between signals of the same burst arrived at different antennas can be employed for the location estimation. The phase difference was demonstrated having a smooth change when the tag was moved, however there was not an algorithm to determine the tag's position using the measured phase difference. Taking this into account, Wille et al. [74] developed a RFID navigation system using the phase difference to track medical instruments such as needles or catheters.

Support Vector Regression (SVR), a machine learning algorithm, was applied to estimate the position of the RFID tag. Three different experiments (line datasets, box datasets and cubic datasets) were conducted for a performance evaluation. The mean errors reported were between 0.8 mm and 2.9 mm. Although the experimental results indicate a feasibility of the phase difference method for the localization of RFID tags, significant improvements are needed before applying this method to capsule tracking. The reason is that two important factors that could affect the accuracy of the localization method were ignored during the experiments. Firstly, the orientation of the tag was kept unchanged during the experiments. Secondly, the significant influence of the human tissues on the RF signals was not considered. On a different study based on the phase difference method [75], FDTD simulations with heterogeneous phantoms were used in conjunction with a non-linear least square algorithm to evaluate the tracking performance. Position errors are found to be within 1cm.

2.2.2 Visible waves

In spite of the fact that visible waves cannot penetrate human body, it has still been considered for the capsule localization through computer vision. In a WCE, white light emitting diodes (LED) are used in conjunction with a miniature camera to capture endoscopic images during its journey along the GI tract. By processing the captured images coming from the capsule, the region of the GI tract in which the capsule passes through can be estimated [76, 77]. In order to classify the images into appropriate regions, Neural Networks (NN), Vector Quantization (VQ) and combination of VQ with Principal Component Analysis (PCA) were employed. These classification methods, which used Homogeneous Texture descriptor and a MPEG-7 visual content descriptor, were able to distinguish between the upper and lower parts of a GI tract and between different regions in the upper part, such as esophagus, cardia, corpus of the stomach, pylorus, and duodenal cap. Although NN method produced slightly more accurate results than VQ and VQ+PCA, the latter sped up the computation significantly. Another effort using computer vision for classifying different organs of the GI tract in a WCE video (Fig. 2.9) is via event boundary detection algorithm [78]. Events such as when the capsule enters the next organ or intestinal bleedings can be detected by color change pattern analysis. It is reported that the precision of 51% was achieved after performing experiments with ten WCE videos. Furthermore, Evaggelos et al. [79, 80] proposed a method based on feature tracking to estimate the travel distance of the capsule from the entrance of the classified region in the GI tract.

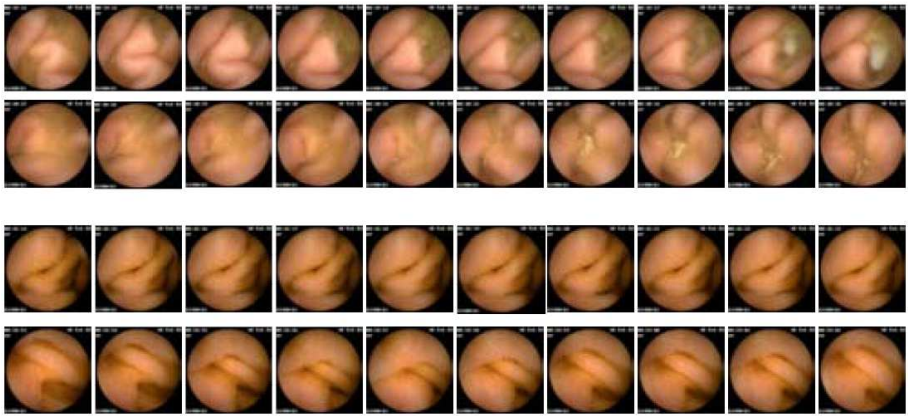

Figure 2.9: Sequence of Frames of WCE Video in stomach (top) and small bowel (bottom) [78].

As mentioned above, the tracking systems using magnetic sensor arrays can obtain 5D localization parameters without the rotation angle around the capsule's main axis, i.e. the roll angle. This is due to the fact that the magnetic field created by a cylindrical magnet is unchanged when the magnet rotates around its main axis. Therefore, Li et al. [81] presented a method based on computer vision to determine the roll angle. Based on the similarity between two consecutive endoscopic images, the rotation parameters of the capsule can be estimated through a combination of several algorithms such as Lucas-Kanade optical flow, 8-point algorithm, and quaternion algorithm. These algorithms were used for tracking correspondent feature points, selecting feature points, and rotation decomposition, respectively. It was reported that when the roll angle varied within a range of less than 30°, the maximum angle error was 1.8°. However, the algorithm failed when the angle change was larger than 30°.

Although the localization methods described in this section do not require any addition hardware in the WCE or any external equipment, the tracking accuracy significantly depends on the speed of the capsule and the image capturing rate. A large variation in two consecutive images would result in a large error, or even a tracking failure. These methods may thus not be suitable for an active WCE which could have rapid movements due to an external control. In addition, the basic data provided by the methods are not sufficient to serve as a feedback for an actuation system. They can only be used as a reference to help the endoscopists improve the diagnostic performance.

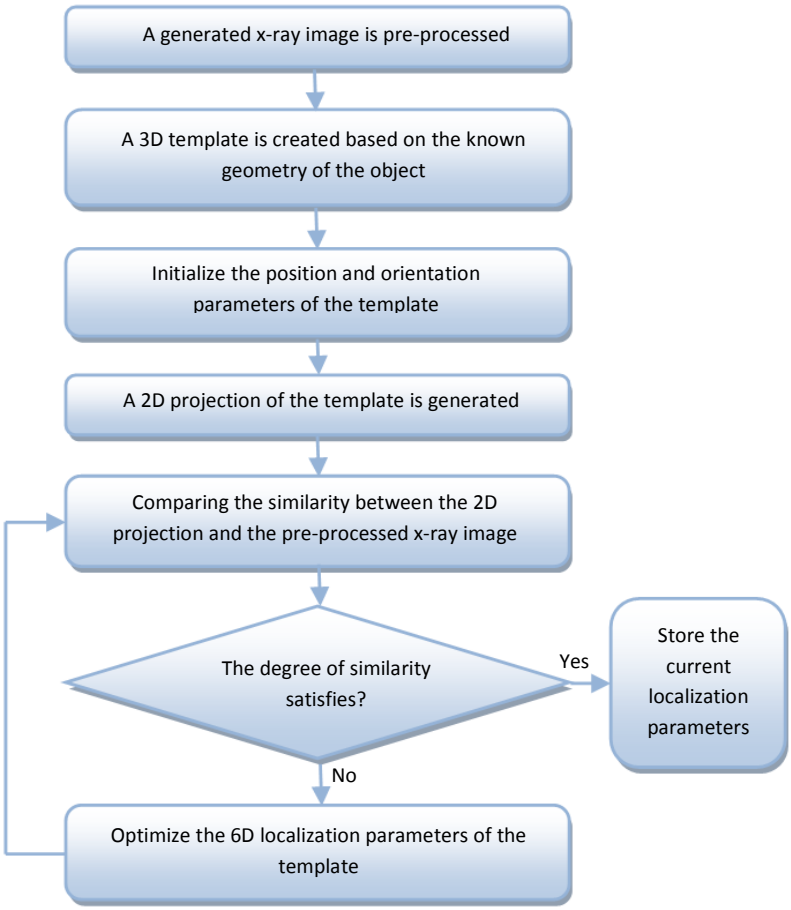

Figure 2.10: Steps to calculate position and orientation parameters of an object using its projection on an x-ray image.

2.2.3 X-rays

X-rays, which have been used widely for medical imaging, can also be exploited to track an object inside a human body. Fluoroscopy, an imaging technique based on X-ray radiation, was used in a magnetic steering system as a visual guide for the maneuvers [26]. The relative position of the capsule to the patient's organs are shown continuously in 2D images in real-time. However, this method can only provide visual assistance via radiation images, while it is impossible to obtain the absolute coordinates of the capsule's position and orientation. To solve this issue, Kuth et al. [82] proposed a method that takes advantage of both x-ray imaging and image processing for the localization of WCE. The solution was based on the fact that when the distance between an x-ray source and a radiation detector plane is kept unchanged, every change in the position and orientation of an object within the coverage of the X-ray beam can lead to an equivalent change in the projection on the detector. Therefore, the position and orientation parameters of the capsule can be computed depending on the shape of the projection on the radiation images. In some extreme cases when the longitudinal axis of the capsule is perpendicular to

the detector, another x-ray source is placed at an angle to the first one to enhance the system's accuracy. The image recording rate is controlled based on the speed of the capsule. Iteration steps to compute the position and orientation of the capsule from its projection on the x-ray images is explained in detail in [83] and shown in Fig. 2.10.

In the algorithm, a 3D virtual model of the capsule and its components are built. The 2D projection of the virtual model on an equivalent detector plane is compared with the real projection. Depending on the similarity between these two projections, the algorithm produces an optimized rotation matrix and a translation vector to move the 3D virtual model to a new location with a different orientation. This process is repeated until the degree of similarity between the real projection and the updated projection is acceptable. The rotation and transformation parameters of the 3D model are adopted to be those of the capsule. Although this method promises to deliver highly accurate results, the potential hazard for the patient in case of high x-ray dosage is a significant disadvantage (especially when the endoscopic procedure is long). Using a hybrid system which combines the x-ray method with one of the other 3D localization methods could be a solution to reduce the radiation burden on the patient's body.

2.2.4 Gamma rays

Although gamma rays have not been employed for the localization of WCE, this method was exploited in the gamma-scintigraphy technique to visualize the position of an Enterion capsule, a drug-delivery type capsule, in real-time [84]. The capsule that is loaded with gamma-emitting radioisotopes can be detected by scintillation cameras. Since gamma rays are absorbed partly by human tissues when traveling from the radioactive agent to the cameras, both dorsal and ventral images are taken to enhance the tracking accuracy [85]. However, this method can only provide visual images of the radioisotope location without orientation data of the capsule.

2.3 Other localization methods

Beside the above localization methods, magnetic resonance imaging (MRI), a widely used diagnostic imaging technique, could also be employed for localization [86–88]. Dumoulin et al. [86] proposed a method for tracking interventional devices such as catheters, biopsy needles in real-time using MRI. In this method, the spatial position of an interventional device was determined by incorporating one or more

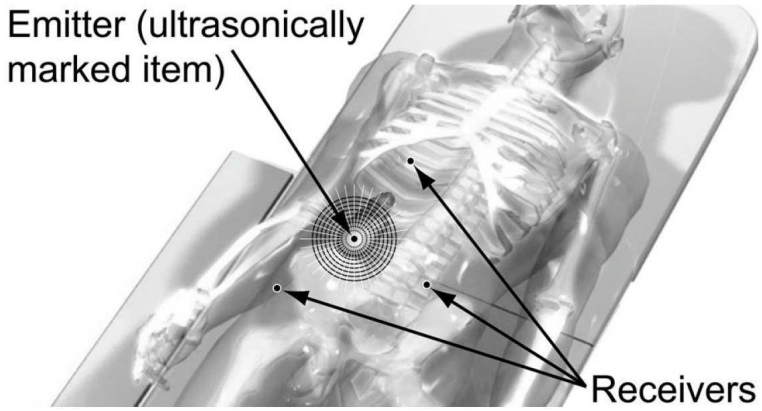

Figure 2.11: Receivers placed on a patient's abdomen to detect ultrasonic signals emitted from a transducer integrated in a capsule [91].

miniature RF coils into the device to sense special MRI pulse sequences. Adopting this tracking method, Krieger et al. [88] demonstrated that six degree-of-freedom (6-DOF) position and orientation of a biopsy needle which carries three micro-tracking coils could be computed with a tracking speed, a mean positional error and a rotational error of 20 Hz, 0.2 mm and 0.3°, respectively. However, this method requires custom-programmed pulse sequences, which are different from the standard pulse sequences of commercial MRI scanners [89, 90]. In addition, using very costly MRI equipments would also be a significant disadvantage of this method.

Ultrasound, another diagnostic imaging technique, is also a potential method for localization in soft tissue. The position information can be estimated by means of two different approaches. The first approach is based on measuring the time of flight (TOF) between ultrasonic pulses transmitted from an external source and the echoes reflected by the capsule [92]. In this approach, the accurate knowledge of the speed of sound in different human tissues plays an important role in the tracking accuracy. Moreover, the capsule must always lie in the scanning plane to be sensed [91]. This drawback can be overcome by the second approach, in which an ultrasound transducer is embedded inside the capsule, and external receivers are located on the patient's abdomen (Fig. 2.11) to detect the emitted ultrasonic signals [20, 93]. Since the ultrasonic signals only need to travel through the media once, this approach offers twice deeper penetration than the first approach. However, using ultrasound for WCE localization would be a challenge due to the acoustic impedance mismatch [94].

Table 2.1: A comparison of the key localization methods. "-" indicates that the information is unknown. The accuracy may be "High" (position error < 2 mm), Moderate (position error within 2 mm to 20 mm), or Low (position error > 20 mm).

	Localization methods	**Occupy space within capsule**	**Consume battery power**	**Accuracy**	**Interference with magnetic actuation**	**Real-time**	**Adverse health effects**
Magnetic localization (passive WCE)	Permanent magnet	Yes	No	High	Yes	Yes	No
	Secondary coil	Yes	Yes	Moderate	Yes	-	No
	Magnetoresistive sensor	Yes	Yes	Moderate	Yes	No	No
Magnetic localization (active WCE)	HF alternating magnetic field	Yes	No	High	No	Yes	-
	Inertial sensing	Yes	Yes	Low	No	-	No
	Embedded sensors to measure actuation magnetic field	Yes	Yes	Moderate	No	-	No
Electromagnetic radiation	Radio frequency	No	No	Low	No	No	No
	Visible waves	No	No	Low	No	-	No
	X-ray	No	No	High	No	Yes	Yes
	Gamma ray	Yes	No	-	No	Yes	Yes
Others	MRI	Yes	Yes	High	-	Yes	-
	Ultrasound	Yes	Yes	-	No	Yes	-

2.4 Summary

Although many localization methods have been proposed as reviewed above, none of them can offer a complete solution to address the challenging localization problem for WCE. To date, a commercial WCE can only provide 2D position information with a very low accuracy (37 mm). Table 2.1 illustrates a comparison of different methods presented in this chapter. As shown in the table, the approaches which have potential to obtain high accuracy are either influenced by the magnetic field to be used for actuation or having adverse health effects to the patient, or still at the proof-of-concept stage.

Chapter 3

Methods and Materials

3.1 Introduction

To solve the localization problem for WCE, a novel localization method based on tracking multiple positron emission markers is proposed. In this method, at least three spherical positron emission markers with diameters of less than 1 mm are embedded in the cover of an endoscopic capsule. Depending on the activity of the isotope confined in the markers, a number of coincidence gamma rays are emitted from the markers in each time interval (called a localization run). Therefore, two pairs of position sensitive gamma ray detector modules are arranged around a patient's body to detect these coincidence gamma rays. The positions of the three markers, which refer to the position and orientation of the capsule, can then be determined using an effective tracking algorithm.

The main benefits of the proposed localization method include:

- Capability of delivering a high tracking accuracy with both position and orientation data, which is verified by simulation data (Chapter 4) and experimental data (Chapter 5).
- Real-time tracking.
- No space occupation within the compact capsule.
- No power consumption of the integrated battery within the capsule.
- Compatibility with other actuation systems, especially magnetic actuation systems.

The principle of operation, the conceptual system design and the tracking algorithm itself are explained in further detail in the remainder of this chapter.

3.2 Principle of operation

3.2.1 Positron emission

An atom consists of a nucleus with electrons rotating around it. The nucleus contains a number of protons (denoted by Z) and a number of neutrons (denoted by N). The number of electrons in an atom is normally equal to the number of protons in the nucleus. While electrons have a negative electrical charge, protons and neutrons have a positive and zero charge, respectively. The total number of neutrons and protons in an atomic nucleus is called the mass number (denoted by A). A nuclide is an atomic species characterized by the specific constitution of a given number of protons and neutrons in a nucleus. A nuclide is represented by ${}^{A}_{Z}X_{N}$.

Approximately 270 nuclides are stable, while more than 2,800 nuclides are unstable, called radionuclides. The nuclides are unstable due to two reasons: the ratio of protons to neutrons is beyond a certain range, or the total number of protons is higher than 82, which is the atomic number of lead. Many unstable nuclides have been artificially produced in cyclotrons or reactors, and some occur naturally. The nuclides which have the same number of protons are called isotopes.

Positron emission (or β^+ decay) occurs when a proton-rich isotope decays. In this process, a proton (p) is converted into a neutron (n) which results in an emission of a positron (β^+) and a neutrino (ν) as shown in (3.1). A positron and an electron have the same mass but opposite electric charge. They behave similarly when passing through the human body. The neutrino has a very weak interaction with matter, thus it is generally not considered in medical applications.

$$ {}^{A}_{Z}X_{N} \rightarrow {}^{A}_{Z-1}Y_{N+1} + \beta^+ + \nu \tag{3.1} $$

$$ p \rightarrow n + \beta^+ + \nu \tag{3.2} $$

where ${}^{A}_{Z}X_{N}$ is the parent nuclide, and ${}^{A}_{Z-1}Y_{N+1}$ is the daughter nuclide. Since a neutron is heavier than a proton by one electron mass, the right side of (3.2) is two electron masses more than the left side. Based on the energy conservation law, the radionuclide must have a transition energy of 2×0.511 MeV $= 1.022$ MeV to decay by positron emission. This energy is split as kinetic energy between the positron (β^+) and the neutrino (ν).

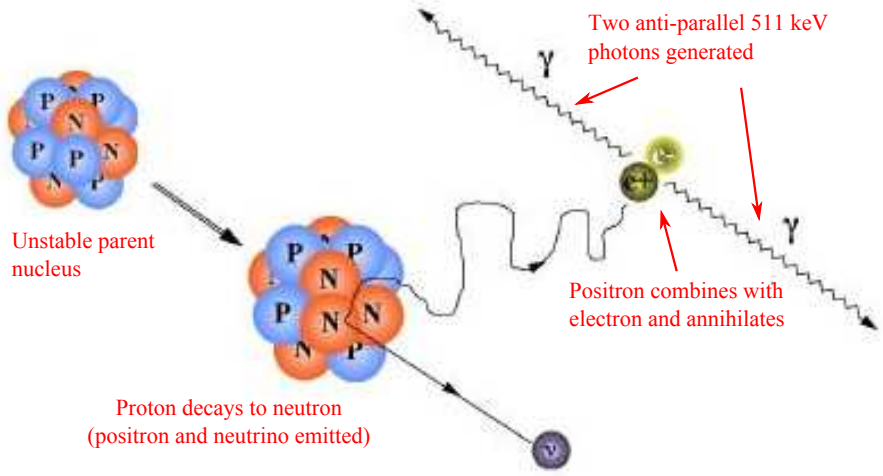

Figure 3.1: Process of positron emission and annihilation of a positron and an electron (http://depts.washington.edu).

3.2.2 Annihilation and gamma rays

After the positron is emitted from the nuclide, it travels at a high speed (almost the speed of light) to the surrounding environment. It interacts with matter by ionizing and exciting many of the nearby atoms. As it loses energy due to the interaction, it eventually slows down and encounters an electron. As soon as this happens, these two particles mutually annihilate and their masses are converted into electromagnetic energy (1.022 MeV). This energy is released in form of two gamma rays (511 keV) traveling in almost opposite directions (180° apart). The entire process is illustrated in Fig. 3.1 and Eq.(3.3).

$$\beta^+ + e^- \rightarrow \gamma + \gamma \tag{3.3}$$

The distance that the emitted positron has traveled before the annihilation event occurs is called positron range. Typically, it is within a few millimeters depending on the kinetic energy of the positron and the medium. Therefore, each isotope has a different positron range for a certain medium. In some cases, the gamma rays are emitted a few tenths of a degree less than 180° apart due to the left over energy and momentum of the positron and the electron. This phenomenon is called noncollinearity.

3.2.3 Positron emission tomography

Positron emission tomography (PET) is a nuclear imaging technology that is used to provide 3D tomographic images of the distribution of positron emitting tracers within the body. Based on the principle mentioned above, PET systems contain

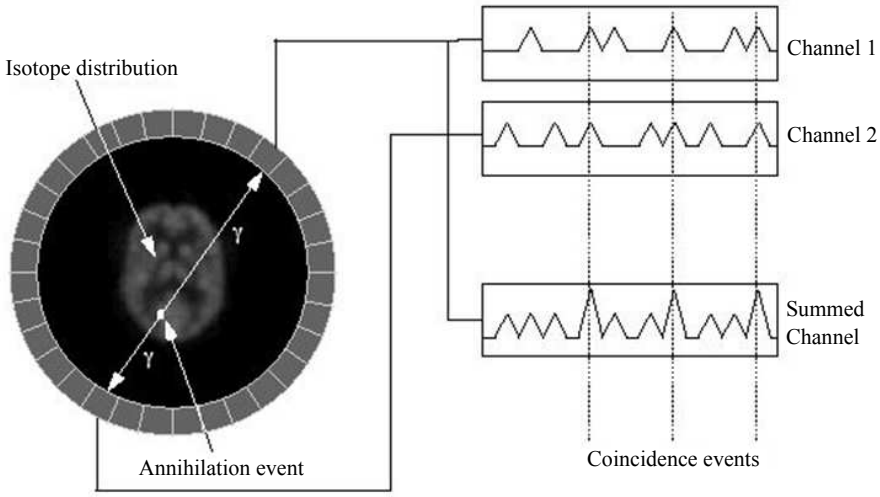

Figure 3.2: Coincidence detection in a PET system [95].

several rings of scintillation detectors surrounding the patient to detect the generated gamma rays from the annihilation. Simultaneously detecting both annihilation photons defines a line of response (LOR), and the location of the annihilation in the body is assumed to be somewhere along this line. Using a large number of detected events (i.e. LORs), the spatial distribution of the tracer can be determined.

A coincidence event is considered to occur when two opposite detectors detect the two gamma rays within a very short interval of time (typically from six to twelve nanoseconds). This time interval is called a time window. Fig. 3.2 shows how the circuitry within the PET scanner identifies an annihilation coincidence event. Each detector acts as a single event detector, and it generates a timed pulse as soon as it receives an incident photon. These pulses are recorded in their corresponding channels in the coincidence circuitry. A summed pulse is calculated in every time window to check if any coincidence occurs within the time interval. In one second, a large number of coincident events are detected depending on the activity and the type of the tracer. The line that joins the two detectors which are involved in the detection of a coincidence event is called a coincidence line (or LOR).

3.2.4 Coincidence events

Due to Compton inelastic scattering and the fact that occasional multiple annihilation events occur within the same time window, there are four major types of coincidence events: true, random, scattered and multiple.

- True coincidences (Fig. 3.3c): A true coincidence occurs when both gamma rays from a single annihilation event are detected in coincidence without either of them undergoing any form of interaction with the object being scanned.

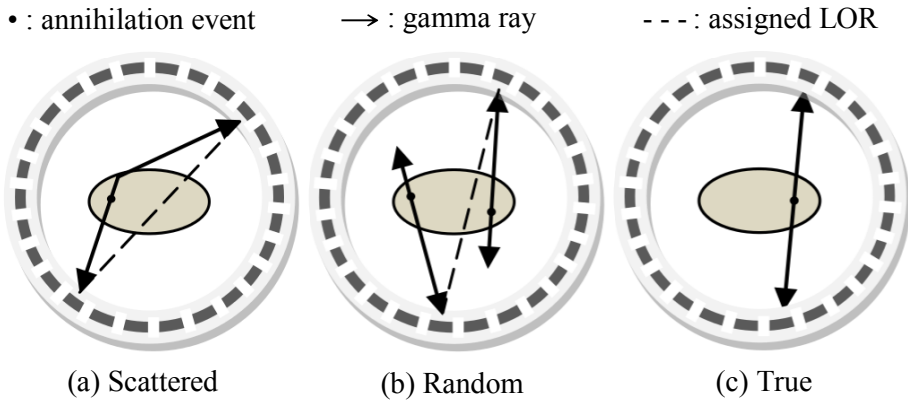

Figure 3.3: Three main types of coincidence events.

There must be no other events detected during this time window.

- Scattered coincidences (Fig. 3.3a): A scattered coincidence occurs when at least one of the gamma rays from a single annihilation event scatters in the object being scanned prior to detection. Since the Compton scattering process changes the direction of the gamma ray, the resulting LOR will be misplaced. This results in a decrease in the image contrast and the spatial resolution of the image. The ratio of the scattered coincidences to true coincidences depends on the medium inside the object and on the detector geometry.

- Random (or accidental) coincidences (Fig. 3.3b): A random coincidence occurs when two gamma rays not arising from the same positron decay are detected in coincidence within the same time window. Random coincidences are distributed uniformly across the field of view (FOV), and the rate of random coincidences increases approximately with the square of the activity of the isotope.

- Multiple coincidences: Multiple coincidences occur when more than two gamma rays arising from two or more positron decay are detected in coincidence by different detectors. Since more than two detectors are involved in this case, it is unable to determine the LOR, and thus the event is discarded.

3.2.5 Scintillation detection systems in PET

The detectors used in PET to detect the gamma rays are scintillation crystals such as BGO (bismuth germinate), LSO (lutetium oxyorthosilicate), LYSO (lutetium yttrium oxyorthosilicate), and so on. When the annihilation photon reaches a crystal, it deposits its energy in the scintillating material. This energy excites atoms of the material to a higher energy level. These atoms are then de-excited to the ground state, giving off visible light.

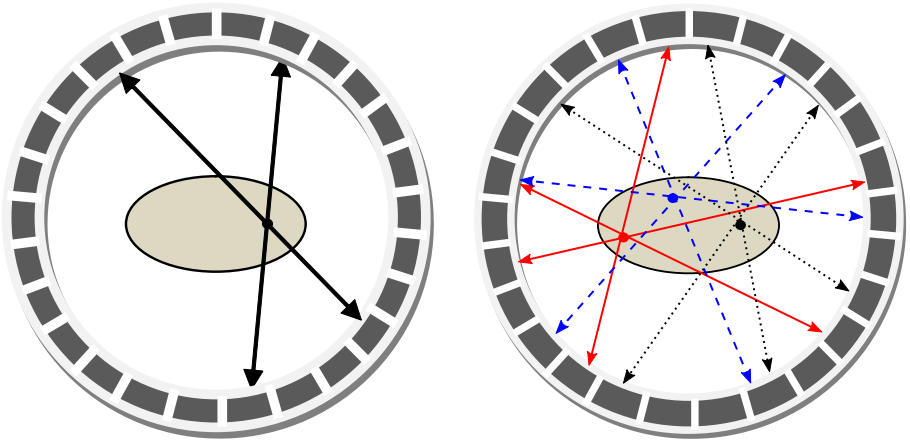

Figure 3.4: A simple diagram of tracking a single positron emission source (left), and tracking three positron emission sources (right).

A photo-multiplier tube (PMT) is coupled to the crystals to convert the light photons produced in the crystals to an electrical pulse. Using PMTs, signals identifying the position, deposited energy, and time of each interaction can be obtained.

The electrical pulses from the PMTs are passed through a pulse height analyzer (PHA), which is an energy discriminator with a low-energy level and an upper-energy level, to reject photons whose deposited energy differs significantly from 511 keV. This discriminator is essential in PET to reduce the number of scattered photons detected. Scattered annihilation photons have lower energy than the unscattered ones. The upper-energy level is used to avoid the case that multiple photons reach the same detector at the same time. The narrowness of the energy window of the PHA needs to be optimized such that scattered photons are rejected accurately while not affecting the sensitivity of the PET system.

3.2.6 Tracking multiple positron emission sources

As mentioned above, when a coincidence line is recorded, a positron annihilation event is expected to have occurred somewhere along the coincidence line. Therefore, if there is only a single positron emission point source being scanned, ideally two non-parallel coincidence lines are sufficient to locate the source as shown in Fig. 3.4. However, in practice, due to the positron range, noncollinearity, random and scattered coincidences, it is necessary to have a sufficient number of coincidence lines to improve the tracking accuracy. In this case, the 3D location of the point source can be estimated by finding the point that minimizes the sum of squared perpendicular distances to all of the recorded coincidence lines [96].

Extending the above principle, it is possible to track multiple positron emission sources by PET detectors. However, each coincidence line collected first needs to

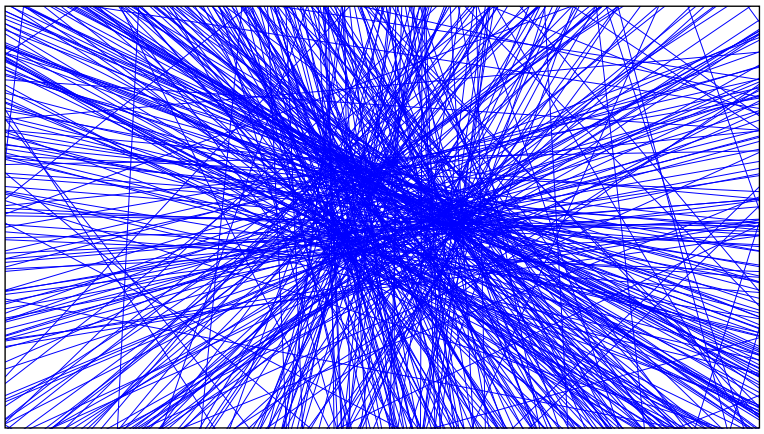

Figure 3.5: Coincidence lines arising from three markers in one localization time interval. The location of the markers is evident.

be assigned correctly to the corresponding source that has generated it. Then, the position of each individual source can be determined from its set of coincidence lines, similar to the case of tracking a single point source. As an example, Fig. 3.4 shows a simple diagram of a simple case when there are 3 point sources and each source generates 3 coincidence lines. Firstly, the coincidence lines are classified into 3 groups: red, blue and black. Then, the position of the red source is the point that minimizes the sum of squared perpendicular distances to all the red lines. A similar process applies to the blue and black sources.

3.2.7 Proposed localization method for WCE

In conclusion, the principle of operation of the localization method for WCE proposed in this thesis is summarized as follows:

In order to determine both the position and orientation of a WCE, three positron emission markers are embedded in the cover of the capsule, as shown in Fig. 3.6. Due to annihilations of emitted positrons from the markers with electrons from the surrounding environment, a number of gamma rays are generated in each localization time interval (or localization run). These gamma rays can then be detected by gamma ray detectors placed around the patient's body. Each gamma ray detected by the detectors generates a line of response, called a coincidence line. Figure 3.5 illustrates coincidence lines collected in one localization time interval. Due to scattered coincidence and random coincidence, most of the coincidence lines are true but some are corrupted. An effective tracking algorithm is developed to determine the position of each marker. The position and orientation information of the capsule can then be obtained based on the position data of the three markers.

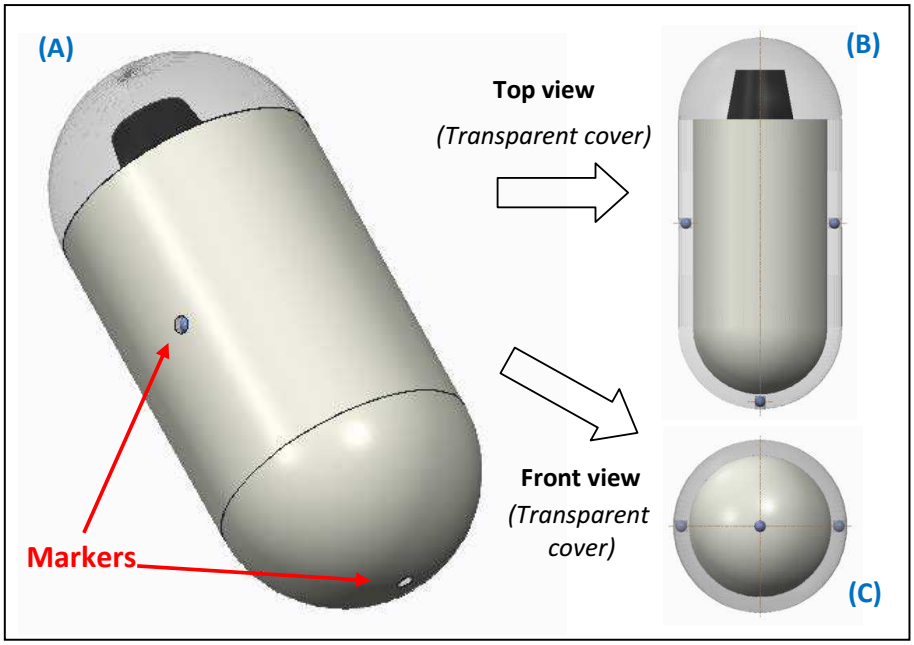

Figure 3.6: Conceptual design of a PECapsule. (A): Three positron emission markers are embedded in the cover of the capsule. (B) and (C): Top and front views (cover is drawn transparent for better visualization of the markers). (Note: figure not drawn to scale).

3.3 Conceptual system design

3.3.1 "Capsule with marker" prototype

An endoscopic capsule carrying positron emission markers is called a PEcapsule. On a 1.5 mm-thick cover of a PEcapsule, there are three $\phi\,1$ mm $\times\, L\,1.25$ mm cylindrical holes as shown in Fig. 3.6 so that the markers can be attached to the PEcapsule before the start of an endoscopy procedure. A 0.25 mm thick lid at the top of the hole will then lock the marker to prevent it from being released during the procedure. The three markers form a triangle with sides of 10 mm, 13 mm and 13 mm long respectively.

3.3.2 Isotopes and markers

In tumor tracking [96], the choice of isotope is limited due to the restriction of the isotope's half-life. The markers remain in the tumor after completing the radiation therapy, thus their half-lives are only allowed to be from a few days to a few weeks depending on the treatment duration [96]. This is to avoid high internal radiation dose to the patient. Conversely, in capsule localization, the capsule is generally disposed in normal excretion after traveling for approximately 8-10 hours inside the GI tract [12]. Therefore, in most cases, the patient will not be exposed to additional

radiation once the WCE examination has been completed. Moreover, in the future when the capsule is provided with an active actuation system, the duration of a WCE examination is expected to be shortened significantly and capsule retention is not expected to occur. Accordingly, this provides a broader range of choice of isotopes used in capsule tracking. Any positron emission isotope whose half-life is greater than a few hours (typical transition time) could be used.

In this study, ^{22}Na (with a half-life of 2.6 years) is chosen to be the radioactive cores for the three markers. This is because ^{22}Na has already been used widely to manufacture point sources in the field of PET imaging. Secondly, the positron range of ^{22}Na is smaller than that of other positron emission isotopes such as ^{124}I, ^{74}As, ^{84}Rb [97]. Thus, using ^{22}Na will potentially provide higher tracking accuracy. Finally, thanks to its long half-life, the markers can be re-used multiple times for future WCE examinations that require localization without frequent replenishment.

The marker is designed to have a spherical shape with a diameter of less than 1mm. The marker contains a tiny spherical radioactive core ^{22}Na (with a diameter of 0.25 mm to 0.5 mm, and an activity of $50\,\mu Ci$ or 1.85 MBq) centered in an acrylic or metallic shell. For some other isotopes which have higher positron range such as ^{124}I, the spherical shell can be made of gold, tungsten or titanium with a thickness of 0.2-0.3 mm depending on the positron range of the isotopes [97]. This is to confine the emitted positrons to within the shell before annihilation occurs, and thus reduce the effect of positron range in the tracking accuracy. In practice, the marker design can be fabricated using similar techniques that have been used to produce commercial brachytherapy seeds [96].

3.3.3 Gamma ray detectors

Gamma ray detectors which have been used in clinical PET imaging can also be employed in this tracking application for WCE. In the conventional PET systems, for imaging purposes, the detectors need to be arranged in full rings to generate a number of images of the radioactive tracer distribution inside the patient's body using reconstruction algorithms. However, for tracking purposes, in theory, a minimum of 2 pairs of facing detector blocks at a certain angle to each other is sufficient to provide the location information of the markers. This could significantly reduce the cost and the complexity of the localization system for WCE. Figure 3.7 shows a visual comparison between a conventional PET scanner and a reduced detector system for capsule localization. The specifications of this reduced detector system is described in more detail in Section 4.3.3.

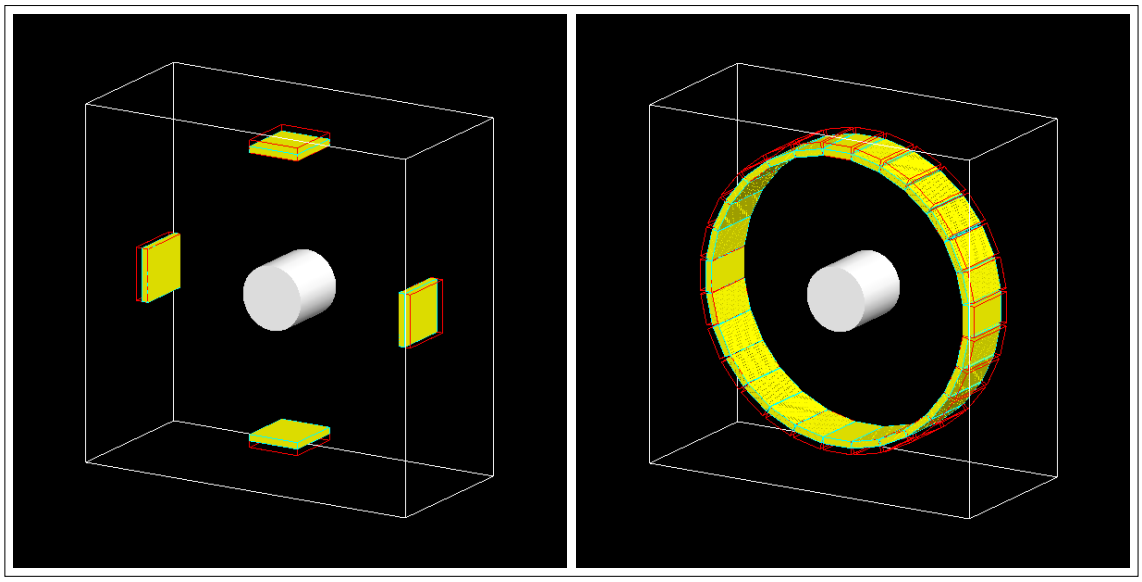

Figure 3.7: Reduced geometry for capsule localization (left) compared to full-ring geometry for PET imaging (right).

3.4 Tracking algorithm

As mentioned above, a number (hundreds or thousands) of coincidence lines (including both true and corrupted ones) are collected in every localization time interval (chosen as 50 ms). A tracking algorithm is required to extract the position information of the three markers from the collected coincidence lines. The algorithm needs to perform fast enough to preserve real-time tracking while ensuring high tracking accuracy. In this section, an effective tracking algorithm [98] based on Fuzzy C-means clustering algorithm is developed. This tracking algorithm is inspired by the algorithm proposed in [96, 97, 99]. Our algorithm consists of four following main steps, and it can be extended to work with not only three markers, but also four, five or more if required.

1. An outlier removal method: to remove corrupted lines based on finding the center of the triangle formed by the three markers. This step provides clean input data for the Fuzzy C-means clustering algorithm in step 4.

2. An initialization method: to estimate the initial points for the three vertices of the triangle (i.e. the initial positions of the three markers). The initial positions are estimated through finding the optimal rotational angles of the triangle when it is rotated around its center obtained is Step 1. This initialization step is only activated at the start of the localization procedure or when the failure prediction method in Step 3 has identified a potential failure. For other localization runs, the last known positions of the markers are used as initial values.

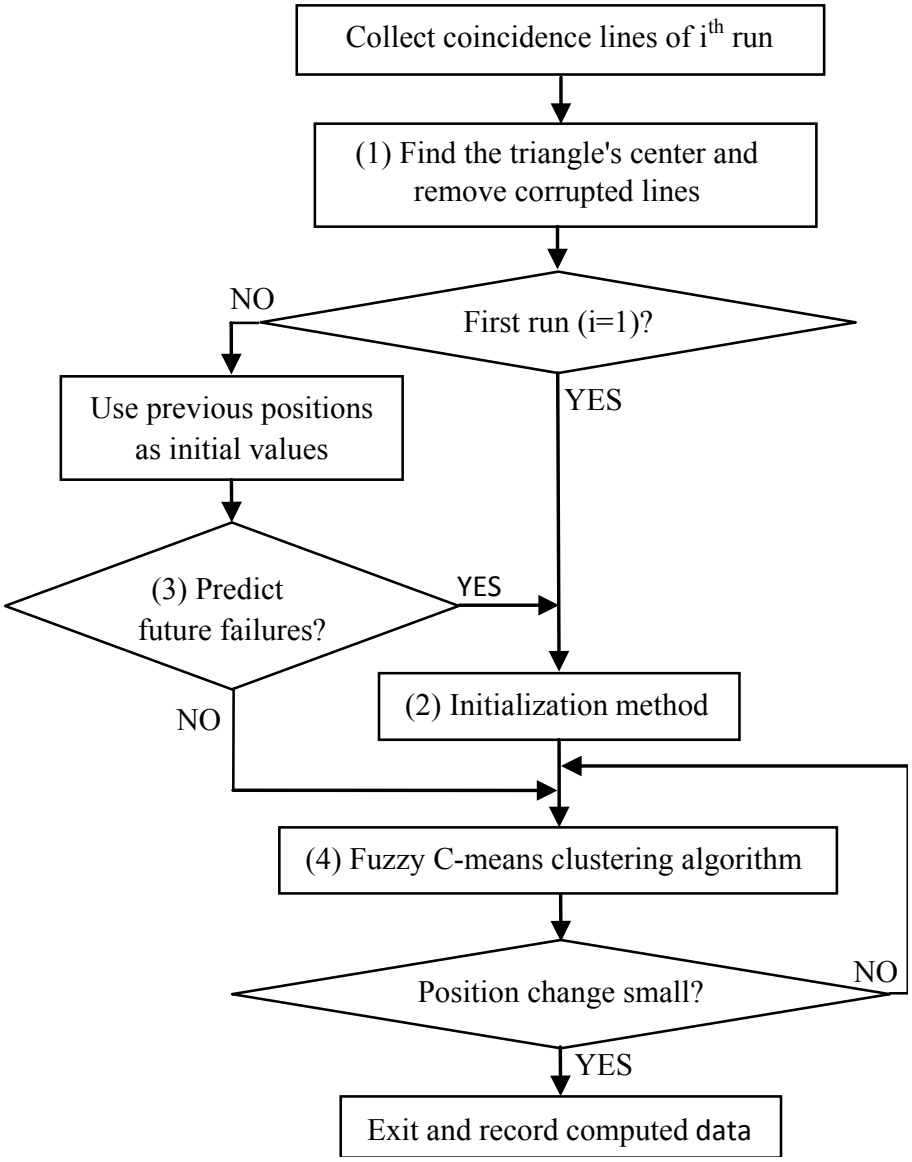

Figure 3.8: Flow-chart of the tracking algorithm.

3. A failure prediction method: In some extreme cases in which the capsule encounters an abrupt movement, the prior knowledge of the markers' position may not be reliable to be an initial value. To prevent the clustering algorithm in Step 4 from failure in such cases, this step checks and then activates Step 2 again (if necessary) to provide better initial estimates.

4. A clustering method: a core part of the tracking algorithm. This step is based on the Fuzzy C-means clustering algorithm [100] to classify the coincidence lines into three groups such that coincidence lines in each group are supposed to be generated from the same marker. The position of each marker can then be determined by finding the point that minimizes the sum of squared distance to all coincidence lines in the corresponding group.

The algorithm flow-chart is described in Fig. 3.8, and each step is explained in detail in the following Sections 3.4.1 to 3.4.4

3.4.1 Removing corrupted lines and finding the triangle center

As shown in Fig. 3.6, the three markers form a triangle with edge lengths of 10 mm, 13 mm and 13 mm. In this first step of the algorithm, the center of the triangle is localized first. There are several types of triangle center, but the one that is considered here is the triangle's centroid as it minimizes the sum of squared distances to the three vertices. This centroid is the point that minimizes the sum of squared distances to all of the true coincidence lines.

In order to locate the center of the triangle, the two following sub-steps are executed repeatedly in sequence until no coincidence lines are discarded and the change in the estimated position of the triangle center is less than a pre-determined value:

- Finding the point that minimizes the sum of squared perpendicular distances to all coincidence lines (called minimum distance point).
- Removing coincidence lines that are too far from the calculated minimum distance point based on the modified Thompson Tau's method, a statistical outlier removal method [101].

The mathematical formula representing the iterations to determine the minimum distance point is given by

$$\vec{C}^{(j+1)} = \vec{C}^{(j)} + \vec{T}^{(j)} \tag{3.4}$$

where $\vec{C}^{(j+1)}$ is the new XYZ position of the center at the iteration $(j+1)^{th}$; $\vec{C}^{(j)}$ is the position of the center at the previous iteration (j^{th}). The initial position of the center $\vec{C}^{(j=0)}$ is set at (0, 0, 0) (which is the centroid of the detector system) for the first localization run ($i = 1$), and is set at the previously estimated position for other localization runs ($i > 1$). And $\vec{T}^{(j)}$ is a translation vector (Fig. 3.9), defined by

$$\vec{T}^{(j)} = k_T \frac{\sum_{n=1}^{N} G\left(\left\| \vec{d}\left(\vec{C}^{(j)}, l_n\right) \right\|, \overline{d}^{(j)}, \sigma^{(j)} \right) \cdot \vec{d}\left(\vec{C}^{(j)}, l_n\right)}{\sum_{n=1}^{N} G\left(\left\| \vec{d}\left(\vec{C}^{(j)}, l_n\right) \right\|, \overline{d}^{(j)}, \sigma^{(j)} \right)} \tag{3.5}$$

where N is the number of coincidence lines collected in the current localization run i^{th}; k_T is a scale constant which influences the iteration speed (by testing, we chose $k_T = 0.5$ as it provides a fast but stable convergence for the iteration);

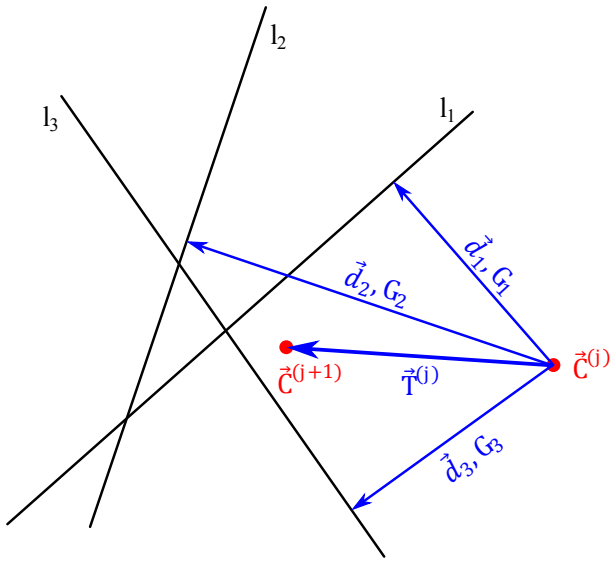

Figure 3.9: Translation vector for finding minimum distance point.

$\vec{d}(\vec{C}^{(j)}, l_n)$ denotes the perpendicular distance vector from $\vec{C}(j)$ to a coincidence line l_n. Calculating distance vectors for every line $l_n\,(n = 1, ..., N)$, we obtain a set (S) of distance components with a mean $\overline{d}^{(j)}$ and a standard deviation $\sigma^{(j)}$. Each distance vector is then assigned a weight $G\left(\left\|\vec{d}\left(\vec{C}^{(j)}, l_n\right)\right\|, \overline{d}^{(j)}, \sigma^{(j)}\right)$ depending on how statistically inconsistent its magnitude is with the rest of the components in the set. The weight $G\left(\left\|\vec{d}\left(\vec{C}^{(j)}, l_n\right)\right\|, \overline{d}^{(j)}, \sigma^{(j)}\right)$ is computed according to the Gaussian probability distribution.

The iterations stop once the position change of the minimum distance point is less than a threshold, i.e. when the magnitude of the translation vector $\vec{T}^{(j)}$ is less than the threshold (in this case 0.1 mm).

The modified Thompson Tau's method [101] is then activated to eliminate the coincidence lines that are too far from the calculated minimum distance point. By this method, only one corrupted line is rejected at a time. In each iteration step, the mean distance $\overline{d}$ and the standard deviation σ of the set (S) are re-calculated, and the line furthest from the minimum distance point is considered as a suspected corrupted line. Using the following rules, this line is determined to be rejected or to be kept

- If $\left(\left\|\vec{d}_f\right\| - \overline{d}\right) > \tau \cdot \sigma$, the line is discarded
- If $\left(\left\|\vec{d}_f\right\| - \overline{d}\right) \leq \tau \cdot \sigma$, the line is kept

where $\left\|\vec{d}_f\right\|$ is the distance from the minimum distance point to the furthest line. τ is the modified Thompson constant controlled by the number of coincidence lines

in the set S. The value of τ can be selected from the table of modified Thompson τ values for different number of data points [101]. For example, τ varies from 1.9530 to 1.9572 when the number of data points is from 200 to 500. Once a corrupted line is rejected, the process starts over and it is repeated until no more corrupted lines are identified.

3.4.2 Initialization method

Given a computed triangle center, the purpose of this step is to estimate initial values for the three markers (i.e. the three vertices of the triangle). This can be done by rotating the triangle around its center such that the sum of squared distances from the vertices to their respective coincidence lines is minimal. Assume that the triangle is rotated by a rotation angle θ around a unit vector (u, v, w) that goes through the triangle center, the positions of the three vertices are

$$\left[\vec{M}_1\ \vec{M}_2\ \vec{M}_3\right] = R(u, v, w, \theta) \cdot \left[\vec{M}_1^{(0)}\ \vec{M}_2^{(0)}\ \vec{M}_3^{(0)}\right] + \left[\vec{C}\ \vec{C}\ \vec{C}\right] \tag{3.6}$$

where $\vec{C}$ is the location of the triangle center; $R(u, v, w, \theta)$ is a rotation matrix as a function of (u, v, w, θ); and $\left[\vec{M}_1^{(0)}\ \vec{M}_2^{(0)}\ \vec{M}_3^{(0)}\right] = \left[(-5, -4, 0)^T\ (0, 8, 0)^T\ (5, -4, 0)^T\right]$ mm are reference positions of the three vertices when the triangle is assumed to lie on the XY plane with its center placed at the origin of the Cartesian coordinate (i.e. the centroid of the detector system).

The sum of squared distances from the three vertices to their respective coincidence lines is a function of (u, v, w, θ) as below

$$D(u, v, w, \theta) = \sum_{k=1}^{3} \sum_{j=1}^{N_k} \left\| \vec{d}(\vec{M}_k, l_j) \right\|^2 \tag{3.7}$$

where k is the marker index ($k = 1, 2, 3$); l_j is the coincidence line to which the marker $\vec{M}_k$ is the closest marker (l_j has a unit vector $\vec{n}_j = (n_{jx}, n_{jy}, n_{jz})$ and pass through a point $\vec{a}_j$); N_k is the number of coincidence lines to which $\vec{M}_k$ is the closest marker; $\left\| \vec{d}(\vec{M}_k, l_j) \right\|$ is the distance from the marker $\vec{M}_k$ to the line l_j.

To minimize D, the parameters (u, v, w, θ) must satisfy the following equation

$$\frac{\partial D}{\partial u} = \frac{\partial D}{\partial v} = \frac{\partial D}{\partial w} = \frac{\partial D}{\partial \theta} = 0 \tag{3.8}$$

From Eq.(3.7) and Eq.(3.6) , we have

$$D = \sum_{k=1}^{3} \sum_{j=1}^{N_k} \Big(- c_j + \vec{V}_j^T \left(R\vec{M}_k^{(0)} + \vec{C} \right) - \left(R\vec{M}_k^{(0)} + \vec{C} \right)^T A_j \left(R\vec{M}_k^{(0)} + \vec{C} \right) \Big) \quad (3.9)$$

where $c_j = \vec{a}_j^T \left[\vec{n}_j\right]_\times^2 \vec{a}_j$ (3.10)

$$\vec{V}_j^T = 2\vec{a}_j^T \left[\vec{n}_j\right]_\times^2 \quad (3.11)$$

$$A_j = \left[\vec{n}_j\right]_\times^2 \quad (3.12)$$

$$\left[\vec{n}_j\right]_\times = \begin{bmatrix} 0 & -n_{jz} & n_{jy} \\ n_{jz} & 0 & -n_{jx} \\ -n_{jy} & n_{jx} & 0 \end{bmatrix} \quad (3.13)$$

Eq.(3.8) can thus be solved by a built-in optimization function in Matlab (e.g. fmincon). Once (u, v, w, θ) have been computed, the initial positions of the markers can be estimated using Eq.(3.6). This initialization method is generally time-consuming, thus it is only used when the localization starts or when a potential failure is detected. For other localization runs, the markers' positions calculated from the previous localization run are employed as initial data.

3.4.3 Fuzzy C-mean clustering algorithm

Given the initial positions for the three markers estimated in step 2, the Fuzzy C-mean clustering algorithm [100] is used to classify the coincidence lines into three groups such that the lines in the same group arise from the same marker. The position of each marker is expected to be the point that minimizes the sum of squared perpendicular distance to all coincidence lines in its corresponding group. In contrast to hard clustering where each coincidence line is only allowed to belong to exactly one cluster, the Fuzzy C-mean clustering assigns a degree of membership of each coincidence line to every cluster.

Similar to the Expectation Maximization (EM) clustering algorithm [96], the Fuzzy C-mean algorithm carries out through the same iterative sub-steps as below. However, a fuzzy function (Eq.(3.15)) is used instead of the Gaussian probability density function employed in the EM algorithm.

- At the start of the algorithm ($i = 0$), the position of the three markers are set at estimated initial values $\vec{M}_k^{(i=0)}$ $(k = 1, 2, 3)$. Since the isotopes confined in the three markers are chosen at approximately the same activity, the number of coincidence lines in each cluster is initially assumed to be equal to each

other. Therefore, the initial relative activity of each marker is

$$f_1^{(i=0)} = f_2^{(i=0)} = f_3^{(i=0)} = \frac{1}{3} \tag{3.14}$$

The relative activity of a marker indicates how large the size of its corresponding cluster is compared to the other clusters.

- At the i^{th} iteration, the degree of membership of each coincidence line l_n ($n = 1, ..., N$) to each of the clusters ($k = 1, ..., 3$) is given by

$$u_{nk}^{(i)} = \frac{f_k^{(i)} \cdot \left(\frac{1}{\left\| \vec{d}(\vec{M}_k^{(i)}, l_n) \right\|^2} \right)^{\frac{1}{(q-1)}}}{\sum_{j=1}^{3} f_j^{(i)} \cdot \left(\frac{1}{\left\| \vec{d}(\vec{M}_j^{(i)}, l_n) \right\|^2} \right)^{\frac{1}{(q-1)}}} \tag{3.15}$$

where $\left\| \vec{d}(\vec{M}_k^{(i)}, l_n) \right\|$ is the distance from the marker k to the line l_n; and q is a weighting exponent which controls the "fuzziness" of the resulting clusters. The exponent q can be any number greater than 1 (by testing, it is chosen as 1.6).

- The new positions of the markers and their relative activity are then updated:

$$\vec{M}_k^{(i+1)} = \vec{M}_k^{(i)} + h \frac{\sum_{n=1}^{N} (u_{nk}^{(i)})^q \cdot \vec{d}(\vec{M}_k^{(i)}, l_n)}{\sum_{n=1}^{N} (u_{nk}^{(i)})^q} \tag{3.16}$$

where h is a scale constant which controls the iteration speed (by testing, h is chosen as 1.5)

$$f_k^{(i+1)} = \frac{\sum_{n=1}^{N} u_{nk}^{(i)}}{\sum_{j=1}^{3} \sum_{n=1}^{N} u_{nj}^{(i)}} \tag{3.17}$$

As explained in Section 3.4.1, most of the corrupted coincidence lines have been identified and discarded by removing the coincidence lines that are too far from the triangle center. However, there may remain some coincidence lines passing close to the triangle center but not belonging to any clusters (i.e.their distances to each marker are larger than 5 mm). Their assigned membership values would contribute to the new estimate of the markers' positions as shown in Eq.(3.16), and hence

negatively affect the tracking accuracy. Furthermore, since the minimum distance between any two of the three markers are 10 mm, a coincidence line whose distance to a marker $\vec{M}_k^{(i)}$ is larger than 5 mm is supposed to belong to other markers. Therefore, the following condition is added to Eq.(3.15)

$$u_{nk}^{(i)} = 0 \quad if \quad \left\| \vec{d}(\vec{M}_k^{(i)}, l_n) \right\| > 5mm \tag{3.18}$$

3.4.4 Failure prediction method

As explained above, the initialization method provides reliable initial values for the markers' positions which most likely lead to successful clustering by the Fuzzy C-mean algorithm. However, the computation of this initial estimate is cumbersome and time-consuming (approximately 0.4 s to 0.5 s) compared to the sampling time of 50 ms (one localization time interval). The initialization method is thus only used for the first localization run when prior knowledge of the markers' positions is unknown. In other localization runs, markers' positions calculated from the previous run can be taken as initial positions for the markers.

In some extreme cases in which the capsule's position and orientation change dramatically after one localization run (e.g. when the patient coughs; or when the capsule falls in a hollow area such as the patient's stomach; or due to a sudden force generated by a magnetic actuation system), the initial estimate based on prior knowledge from the previous run may not be reliable. Wrong initial positions could result in a failure in the Fuzzy C-mean algorithm (the clustering algorithm is considered to fail when at least two markers are assigned to the same cluster). Therefore, a failure prediction method is essential to prevent the Fuzzy C-mean algorithm from having incorrect starting values in such cases. Once the failure prediction method has detected a potential failure, the last known positions of the markers will not be used as the starting points for the clustering algorithm. Instead, the initialization method described in step 2 (Section 3.4.2) is activated again to provide better initial data.

In order to avoid potential failures, the two following conditions are checked before proceeding to the Fuzzy C-mean clustering algorithm:

- The relative distance between any two of the three initial points is compared with a pre-determined value (5 mm). If the former is smaller than the latter, the initial points are considered unacceptable. This is because two initial points that are too close to each other would likely be assigned to the same cluster.

- If the capsule encounters an abrupt movement, the position change of the markers between two consecutive localization runs would be large. The collected coincidence lines would thus be far away from the three initial points. In order to check whether or not this condition occurs, the failure prediction method compares the total number of "close" lines to the three initial points with 50% of the total number of coincidence lines collected in the localization run. The initial positions are considered to be good only if the former is larger than the latter. A coincidence line is considered to be "close" with a marker if their perpendicular distance is less than 5 mm.

3.5 Radiation dose estimation

The criteria for choosing the activity level of the markers depends on several major factors as follows:

- *Required tracking accuracy:* Since the tracking algorithm is executed every localization run, a sufficient number of coincidence lines in every run are essential to achieve the required accuracy. Insufficient numbers of coincidence lines input to the tracking algorithm will result in a low tracking accuracy. The activity of the marker is thus required to be at a certain level in order to generate sufficient coincidence lines.
- *Patient size:* Due to the scattering and attenuation characteristics of the gamma rays when passing through the human tissues, more coincidence lines are detected in a small patient than in a big patient. Therefore, the activity of the marker needs to be chosen at a level such that the required accuracy can still be achieved in a heavy patient.
- *Tracking frequency (or localization time interval):* The higher the tracking frequency is (or the shorter the localization run is), the less number of coincidence lines are detected in one localization run. To ensure real-time tracking, the tracking frequency is determined first based on the speed of the capsule. Then, the required level of the marker's activity can be estimated using the predetermined tracking frequency.
- *Sensitivity of detector system:* The number of coincidence lines detected in each localization run is influenced by many specifications of the detector system, such as the sensitivity, the crystal type, the axial length of the detector ring, the digitizer, and so on. The activity level is thus chosen depending on the specific detector system used.

- *Marker size:* The maximum activity of a marker is limited by the size of the radioactive core confined in the marker. For example, a spherical volume with a diameter of 0.25 mm can contain up to 1.85 MBq of ^{22}Na. Therefore, the marker needs to have a large enough size to contain a sufficient amount of radioactive source. In addition, since the marker is embedded in the cover of the capsule, the marker's diameter should not be be larger than the cover's thickness.

Based on the above criteria and by extensive testing, in this study, the activity of each marker is chosen at 1.85 MBq, i.e. 1.85 Mbq$\times 3 = 5.55$ Mbq in total. Although this activity level is much lower than in a typical clinical PET scan (200-600 MBq of ^{18}F-FDG in a few hours [102]), a quantitative evaluation of the radiation exposure to a patient using the proposed method is still investigated as below.

Since the physical half-life of ^{22}Na ($T_{1/2}$= 2.6 years) is much longer than the duration of one WCE examination (8-10 hours), the loss of activity due to the physical decay of the radionuclide can be neglected. The equivalent radiation dose from a marker to the surrounding tissues can thus be calculated by the external dose formula [103] as below

$$\dot{H} = \frac{\Gamma \times A \times e^{-\mu T}}{d^2} \tag{3.19}$$

where $\dot{H}$ is the equivalent dose rate (in $\mu Sv/h$), Γ is the gamma constant of ^{22}Na (0.362 $\mu Sv/h$ per MBq @ 1m), A is the activity of the isotope (in MBq), μ is the linear PET attenuation coefficient (in cm^{-1}) ($\mu_{\text{tissues}} = 0.096$, $\mu_{\text{bone}} = 0.172$ [104]), T is the thickness of the attenuating material (in cm), and d is the distance from the marker (m).

Therefore, the total radiation dose from one marker for an entire WCE examination is given by

$$H = \int_0^t \dot{H}\, dt = \int_0^t \frac{\Gamma \times A \times e^{-\mu T}}{d^2}\, dt \tag{3.20}$$

where H is the total radiation dose in one WCE examination from one marker (in μSv) and t is the duration of the examination (in hours). As the capsule moves during the WCE procedure, the distance d from a tissue to the marker is a function of the time dt, the capsule velocity, and the structure of the GI tract. The architecture of the human GI tract, which consists of esophagus, stomach, small intestine and colon, is very complex, especially the small intestine. In addition, the capsule speed varies depending on a number of factors such as peristaltic propulsive force, the environment of the digestive section where the capsule is, an active control for capsule movement, etc. Therefore, it is impossible to calculate the exact cumulative radiation dose to a patient's tissues.

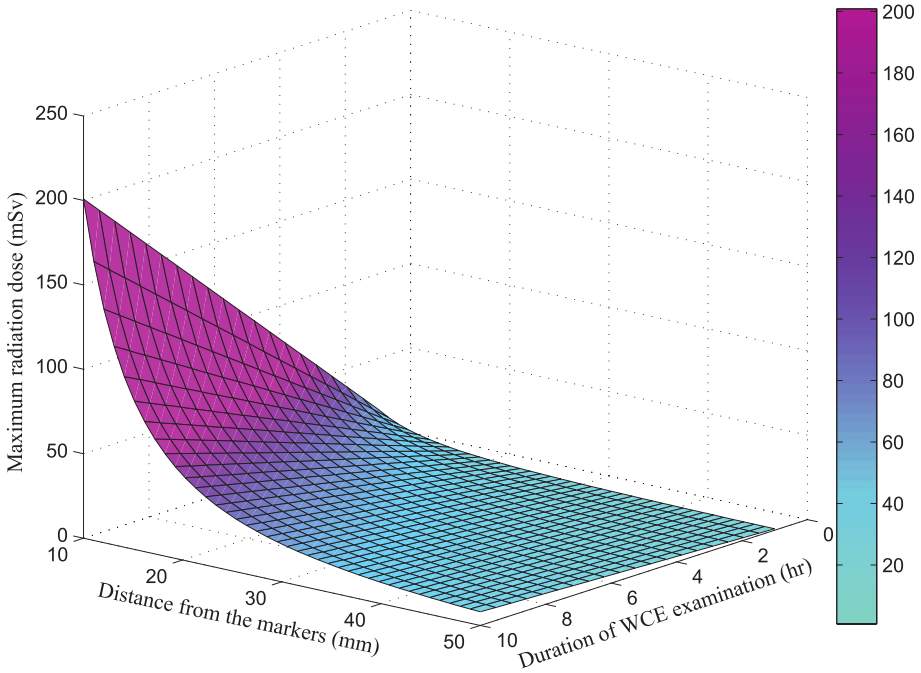

Figure 3.10: Maximum radiation dose from the three markers to surrounding tissues.

However, the maximum equivalent radiation dose to the surrounding tissues from the three markers can be approximately estimated by a simplified equation (when the capsule is assumed to remain stationary, and the gamma rays are assumed to pass through the air before reaching the tissue) as below

$$H_{max} \approx \frac{3 \times \Gamma \times A \times t}{d^2} \tag{3.21}$$

As mentioned above, A is chosen at 1.85 MBq, thus

$$H_{max} \approx \frac{3 \times 0.362 \times 1.85 \times t}{d^2} \tag{3.22}$$

$$\approx \frac{2.009 \times t}{d^2} \, (\mu Sv) \tag{3.23}$$

Fig. 3.10 shows a distribution of the maximum equivalent radiation dose (mSv) to surrounding tissues as a function of the duration of the WCE examination (from 1 to 10 hours) and the distance from the capsule (from 10 mm to 50 mm). The further the distance from the capsule to the tissue is, the lower the radiation that it is exposed to. The radiation dose drops dramatically when the distance is larger than 20 mm. The maximum radiation dose to a tissue that is 50 mm away from the capsule in 10 hours is approximately 8.04 mSv.

3.6 Summary

To summarize, an innovative localization method for WCE based on tracking three positron emission markers embedded in the capsule's cover has been proposed in this chapter. The principle of operation, the conceptual system design, and the tracking algorithm have been presented in detail. Up to this point, three important advantages of the proposed method can be identified. These are: that it does not occupy any space inside the capsule, that it does not consume any power from the built-in battery, and that it is compatible with magnetic actuation systems for controlling the capsule movement (as there is no interaction between gamma rays and magnetic fields). In regards to the radiation exposure to the patient's body, the activity of the markers used in this method is much lower than that of the standard radiotracers used in clinic PET imaging (less than 10 Mbq compared with 200-600 Mbq in a few hours).

In the next chapters, the advantage of real-time tracking and high localization accuracy are verified using simulation data and experimental data using commercial PET scanners.

Chapter 4

Simulation Study

4.1 Introduction

In order to examine the validation of the proposed localization method, a model of the localization system was simulated in GATE v6.2 (Geant4 Application for Emission Tomography), a Monte Carlo simulation toolkit developed by the OpenGATE collaboration since 2001 [105]. GATE is a reliable way to provide accurate modeling of Positron Emission Tomography (PET) and Single Photon Emission Tomography (SPECT). Many models of commercial PET and SPECT systems have been simulated in GATE and then validated by comparing the results generated by GATE against those obtained from real systems. For example, the models of Allegro and Mosaic PET scanners from Philips [106, 107], GE Advance scanner from GEMS [108], and ECAT HRRT scanner from Siemens [109] were validated with an agreement from 1% to 8%. Thanks to its reliability, GATE toolkit has been used widely in many studies in the field of nuclear medicine.

In GATE, simulations can be performed with two different types of phantom: geometric phantom and voxelized phantom. Geometric phantoms, which are created based on a single or a combination of geometric objects such as spheres, cylinders, parallelepipeds etc., are generally used to speed up the simulations when the anatomy of the phantom is not important. On the contrary, voxelized phantoms provide more detailed and realistic simulations but significantly increase the computational time of the simulations due to the complexity of the phantom structure. In this study, the simulations with geometric phantoms were performed first to evaluate the tracking algorithm and prove the feasibility of the proposed method. Then, a more realistic phantom (XCAT phantom [110]), which is based on 3D torso structures using realistic MRI data and high-resolution CT data, is simulated to further

validate the tracking performance.

For performance evaluation, the data obtained by these two classes of simulations are input to the tracking algorithm implemented in Matlab. The evaluation is presented in Section 4.3.2 and Section 4.4.3

4.2 Overview of GATE

GATE is based on the Geant4 [111, 112] libraries to provide a modular, versatile, scripted simulation platform for nuclear medicine applications. GATE is open-source software dedicated to the modeling of Positron Emission Tomography (PET), Single Photon Emission Tomography (SPECT), x-ray computed tomography (CT), and radiation therapy [105, 113]. Over the years, it has been constantly improved and refined by the worldwide collaboration of about 21 laboratories. The objective of the OpenGATE collaboration is to improve, document and test GATE thoroughly against commercially available imaging systems in PET and SPECT. A number of studies have validated the GATE simulated data against real data obtained by commercial PET and SPECT scanners.

GATE can be used for a broad range of applications including optimization of detector design for new scanners, optimization of acquisition and processing protocols, correction methodologies for scatter, attenuation and partial volume, developing new reconstruction algorithms, dose calculation in radiotherapy and brachytherapy, and so on.

GATE allows the modeling of time-dependent phenomena such as scanner rotation, patient motion, source movements, and source decay kinetics. The digitiser chain of the detector, from the interaction of a photon with the scintillating crystals to the collection of a LOR by the electronics, is also modeled in GATE. In addition, GATE can model the physical processes involved in photo interactions with matter such as Compton and Rayleigh scattering, photoelectric absorption, etc.

GATE is user-friendly simulation software since it allows the end-users to design and control each feature of the simulations by using macros instead of C++ programming. This scripting language can be stored in one macro file or separated in several macro files for ease of use.

There are eight general steps to set up and launch a GATE simulation as follows

- *Step one (building scanner geometry):* In this step, the shape, the size and the position of the elements of the scanner system can be designed by combining

several basic geometrical volumes together. The material of each volume can be assigned from the list of the GATE material database.

- *Step two (building phantom geometry)*: This step defines the geometry and material of the phantom. It can be a geometrical structure or a voxelized phantom. A geometric phantom can be created by GATE itself, whereas a voxelized phantom is usually created by an external source and can be imported in GATE.
- *Step three (setting up the physics processes):* In this step, the physics processes for particle construction, interactions for photons/positrons/electrons, radioactive decay, production cuts are defined.
- *Step four (initialization):* This step starts the computation of the cross section tables. Once the simulation has been initialized, the users are unable to modify the geometry and physics list.
- *Step five (setting up the digitizer):* This step defines the signal processing chain of the coincidence detection including the detection of hits in the scintillating crystals, how photons are reflected in the crystal, how PMTs receive the light photons, the processing stage in which energy windows, time window, dead time are set, and the production of coincidences.
- *Step six (setting up the sources):* In this step, the users need to define the type of the source as well as its other characteristics such as geometry, total activity, and its movement. The source movement can be achieved by moving the volume that it is attached to.
- *Step seven (data output management):* In this step, five different output formats such as ASCII, Root, Interfile, LMF (List-Mode Format) and ECAT can be individually enabled or disabled by the users.
- *Step eight (time management):* The acquisition is started in this step. The time slice, the starting time and the ending time of the acquisition is defined by the users.

4.3 Geometric phantom simulation

As mentioned in Section 3.3.3, in theory, two pairs of facing detector blocks at a given angle to each other would be sufficient to localize the PEcapsule (an endoscopic capsule carrying positron emission markers). However, such a reduced-geometry detector system has not been available in practice. Therefore, in this section, first,

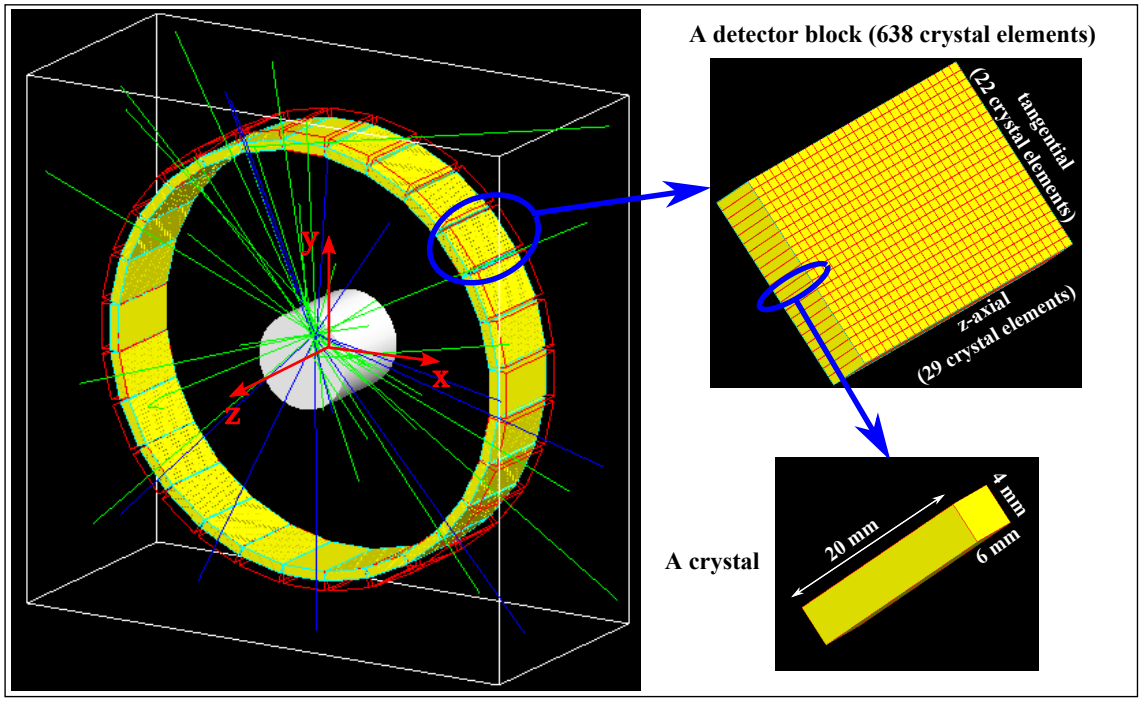

Figure 4.1: Gamma rays are generated from a capsule inside a water phantom (white cylinder) in a GATE simulation. A detector block (top right) and a crystal (bottom right) are presented magnified to show their dimensions.

a model of a commercial PET scanner (Philips Alegro/GEMINI PET scanner) is simulated to prove the concept. Then, a smaller detector system with two pairs of detector modules is modeled to analyze how reducing the detector geometry would affect the tracking performance.

4.3.1 Simulation procedure

4.3.1.1 Scanner geometry

a. Full-ring geometry:

In the first simulation dataset, the model of a gamma-ray detector system is designed according to the geometry of the Philips Allegro PET scanner [106] as shown in Fig. 4.1. In this scanner, 28 detector blocks are arranged in a full ring with an inner diameter of 86.4 cm. Each block consists of 22 (tangential) $\times$ 29 (axial) Gadolinium Orthosilicate (GSO) crystals. Therefore, in total, there are $28 \times 22 \times 29 = 17,864$ crystals in this design. Each crystal element has a surface area of 4 mm (axial) $\times$ 6 mm (tangential), and a thickness of 20 mm. In one block, the gap between any two consecutive crystals are 0.3 mm in both tangential and axial direction. The detector arrangement results in an axial FOV of 180 mm.

b. Reduced geometry:

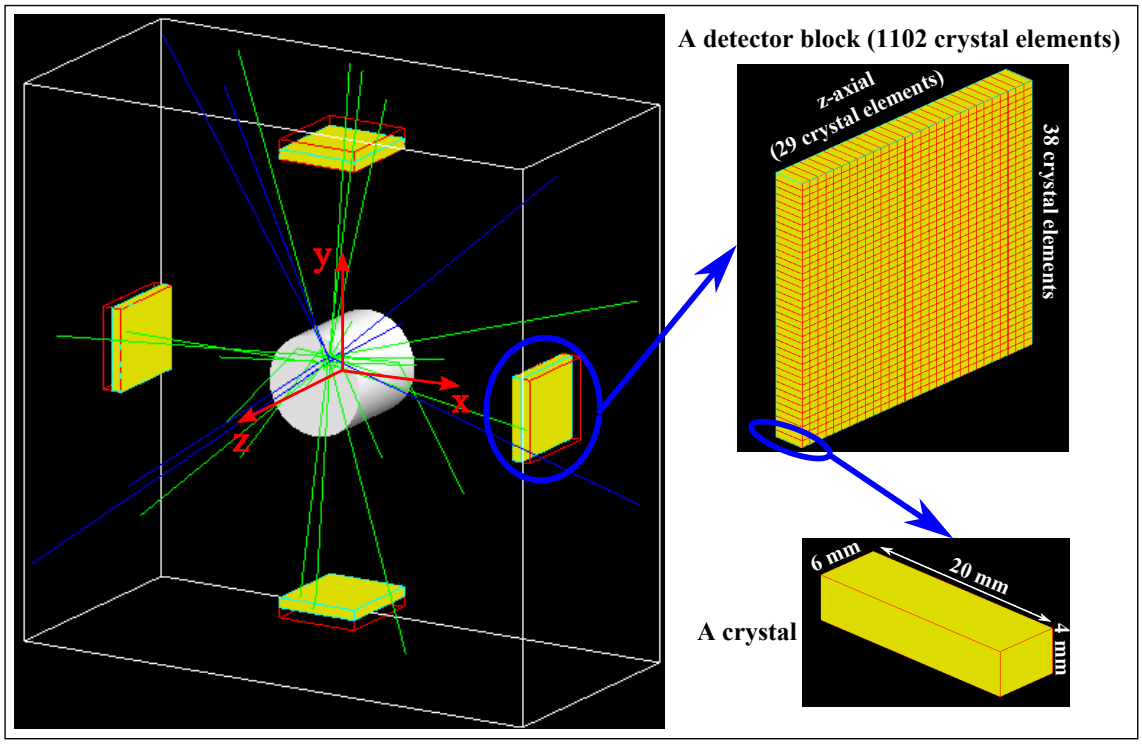

Figure 4.2: A smaller detector system with two pairs of detector blocks placed 90° apart from each other. A detector block (top right) and a crystal (bottom right) are presented magnified to show their dimensions.

In the second simulation dataset, a smaller detector system with two pairs of detector modules placed 90° apart from each other (as shown in Fig. 4.2) is built. Most of the parameters of the full-ring model above are retained. However, instead of using 28 detector blocks, this simulation uses only 4 blocks and each block contains 38 (tangential) $\times$ 29 (axial) crystals. This means that the number of crystals in this design is $4 \times 38 \times 29 = 4{,}408$, i.e. four times less than the number of crystals in the full-ring design (17,864 crystals).

4.3.1.2 Phantom

A cylindrical water phantom with a diameter of 20 cm and a length of 20 cm is placed at the center of the scanner to simulate a patient's body, as illustrated in Fig. 4.1 and Fig. 4.2. The phantom is filled with water to maintain similar attenuation and scattering properties of the gamma rays when they pass through a patient's body. The main axis of the phantom is aligned with the scanner's axial axis (z) (Fig. 4.2).

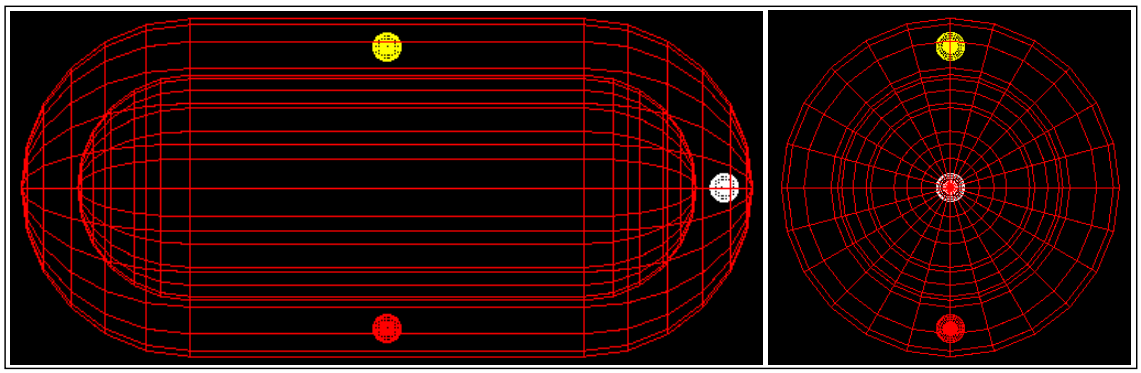

Figure 4.3: Side view (left) and bottom view (right) of the capsule designed in GATE.

4.3.1.3 Sources and markers

A plastic capsule with a diameter of 12 mm and a length of 26 mm is placed inside the phantom. The thickness of the capsule's cover is 2 mm. Three radioactive markers are embedded in the capsule's cover with the same configuration as shown in Fig. 3.6. The modeled marker contains a 0.5 mm-diameter spherical radioactive core encapsulated in a spherical acrylic shell with a thickness of 0.25 mm. The isotope ^{22}Na with an activity of 1.85 MBq is used as the radioactive core confined inside the markers. Figure 4.3 illustrates the design of the capsule in GATE.

The capsule is moved in an orbiting trajectory around the z axis with a speed of 5 mm/s, combined with a translation movement along the z axis with a speed of 2.5 mm/s as illustrated in Fig. 4.6. This is to ensure that the positions of the markers change in all X, Y and Z directions during the movement of the capsule. Note that the orientation of the coordinate system in GATE is different with that of a regular Cartesian coordinate system. As can be seen in Fig. 4.1 and Fig. 4.6, x,y, and z axes in GATE are the lateral axis, vertical axis and longitudinal axis of the detector system, respectively. The capsule travels from a starting point at the location of (-57, 0, -45) mm to the stopping point at the location of (57, 0, 45) mm in 36 seconds. Initially, the capsule is placed in a vertical direction, thus the positions of the three markers are (-57, 12, -45) mm, (-57, 0, -40) mm, and (-57, 0, -50) mm, respectively. When the capsule finishes its journey, the markers' positions are (57, -12, 45) mm, (57, 0, 50) mm, and (57, 0, 40) mm, respectively.

4.3.1.4 Digitizer

In GATE, the signal processing chain of a PET scanner is simulated through a digitizer module. In order to produce coincidences, the main following elements need to be set up in the digitizer:

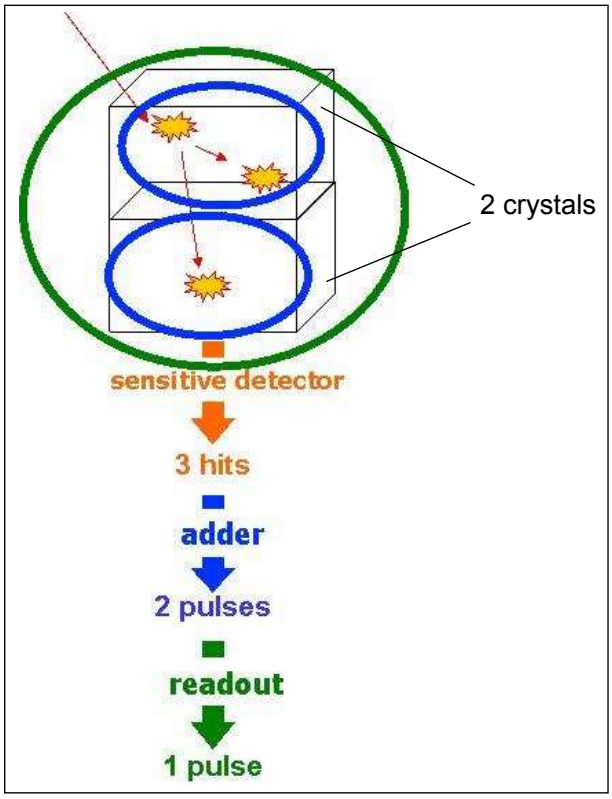

Figure 4.4: Actions of the adder and reader modules in GATE (http://wiki.opengatecollaboration.org).

- Adder: When a photon comes to the detector, it interacts many times with a crystal, and each interaction is called a hit. Since the electronics only measure an integrated signal and is unable to distinguish the hits within a crystal, the "adder" module is used to sum all the hits and creates a single pulse. The energy of the pulse is the sum of energies deposited by the hits in the crystal. The position of the pulse is the energy-weighted centroid of the hits' positions. The time of the pulse is the time of the first hit.

- Readout: Since a photon does not only interact with one crystal but also other crystals in a detector block, the "readout" module is used to sum all the pulses from all the crystals in the block to produce a single pulse (called a "*single*") as shown in Fig. 4.4. The energy of the "*single*" is the sum of energies of all the pulses, and its position is set to the position of the pulse with the highest energy deposited.

- Energy blurring: Depending on the scanner, the energy resolution of the detector is set to simulate Gaussian blurring of the energy spectrum of a pulse. The energy resolution of the Philips Allegro scanner is 0.15 at 511 keV.

- Energy window: Since a photon with an energy of much higher or much lower than 511 keV is unlikely to be generated from a coincidence event, an energy

discrimination window is set to discard low and high energy "*singles*". The thresholder and upholder values of the Philips Allegro scanner are 434.35 keV and 587.65 keV, respectively.

- Time window and time resolution: Two "*singles*" are considered to be in coincidence if they are detected within a time window. The time window is set to 7.5 ns and the time resolution is 3 ns.

4.3.1.5 Physics list

Based on the GEANT4 models for physical processes, GATE allows users to set up their interaction processes of interest. The following physics list (i.e. a list of command to add physical processes of interest) is selected in the simulation:

- Photoelectric effect: Standard model
- Compton scattering: Standard model
- Rayleigh scattering: Penelope model
- Electron Ionization: Standard model for both electron and positron
- Bremsstrahlung: Standard model for both electron and positron
- Positron and Electron Annihilation
- Multiple scattering for both electron and positron

4.3.1.6 Simulation execution and data collection

Localization time interval was chosen as 50 ms, i.e. coincidence lines were collected at a sampling frequency of 20 Hz. As mentioned above, the capsule completed the simulated trajectory in 36 seconds, therefore, there were $36 \times 20 = 720$ localization runs throughout the simulation. Due to the long duration of the simulation, the ASCII output file was extremely large and was thus disabled. Instead, the ROOT output was enabled. Using C++ codes, a list of Cartesian coordinates of the two endpoints of every recorded coincidence line can be extracted from the ROOT file for every localization run. These data were input in the implementation of the tracking algorithm in Matlab to evaluate the tracking performance. Figure 4.5 presents a flow-chart of the entire GATE simulation architecture.

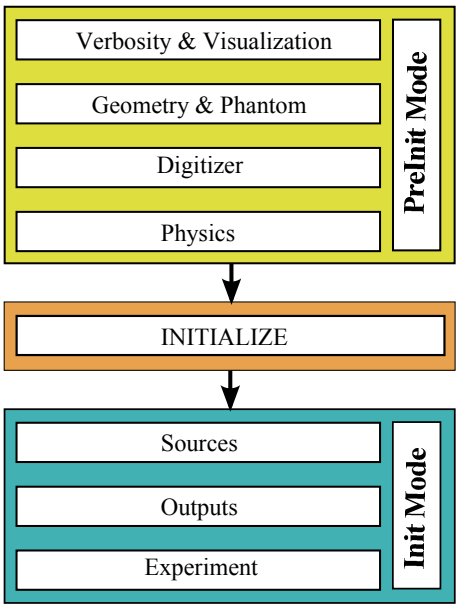

Figure 4.5: GATE simulation architecture (http://wiki.opengatecollaboration.org).

4.3.2 Performance evaluation using the full-ring model

Recorded in GATE, a total of 1,735,600 coincidence lines were acquired when the full-ring model based on the Philips Allegro scanner was used. Therefore, the average number of coincidence lines in each localization run was approximately 2,410. In GATE, it is possible to determine the actual number of random and scattered

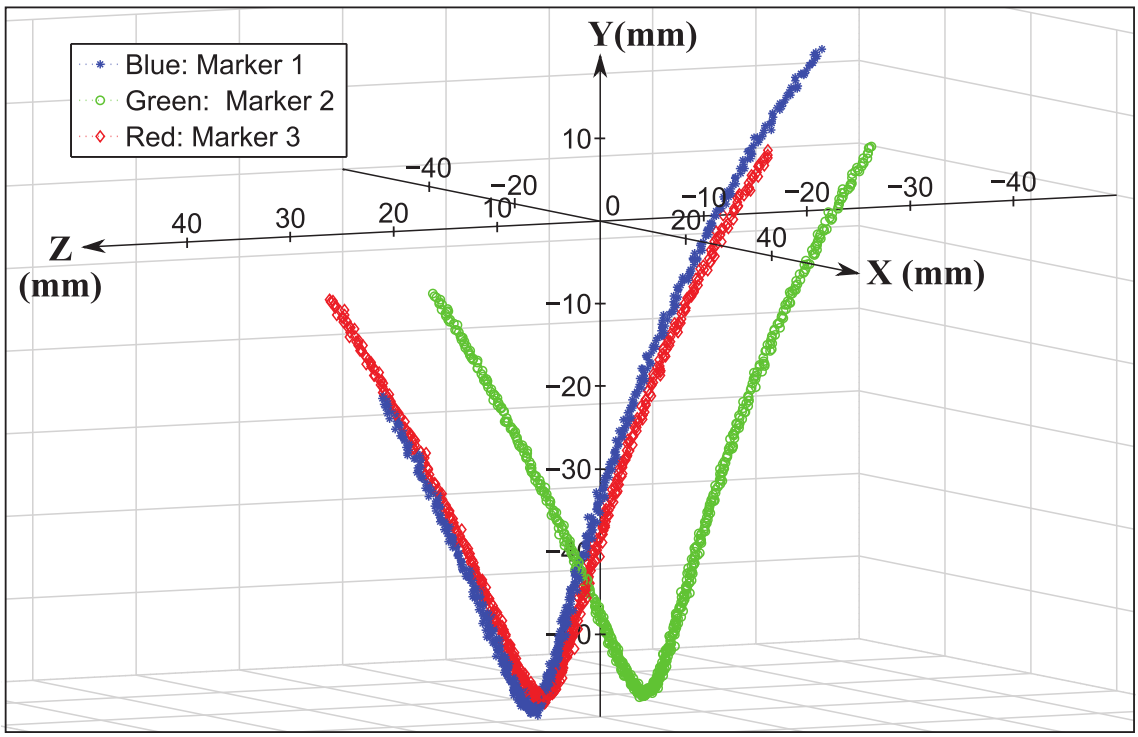

Figure 4.6: Computed 3D positions of the three markers in all localization runs.

coincidence events after the simulation is completed by processing ROOT output files using C++ codes. The total number of true coincidence events recorded was approximately 1,268,400 events, thus the fraction of true coincidence lines over the total number of coincidence lines was 73.1%.

After the tracking algorithm is implemented in Matlab (MathWorks, Inc.) using the data obtained in GATE, the localization was observed to be successful in all 720 localization runs. Fig. 4.6 presents a plot of calculated positions of the three markers in 3D for every localization run which forms three corresponding trajectories. These trajectories are closely related to the movement trajectory of the capsule. The localization performance is analyzed in detail in Sections 4.3.2.1 to 4.3.2.4.

4.3.2.1 Accuracy of finding triangle's centroid and effectiveness of removing corrupted lines

Although an average of 2410 lines are stored in each localization run, only 210 lines are used in the implementation of the tracking algorithm. This number of lines is sufficient to provide a reasonable tracking accuracy while speeding up the computation. A more important reason is to imitate the loss of sensitivity in the case of using a smaller detector system (as shown in Fig. 3.7) in practice. These 210 lines are selected by randomly choosing 21 lines from all the coincidence lines collected in each subinterval of 5 ms (the time-step of the GATE simulation).

The tracking algorithm uses $210 \times 720 = 151,200$ coincidence lines throughout 720 localization runs. However, approximately 37,800 coincidence lines are detected as corrupted lines and thus are discarded by the algorithm. Therefore, an average of

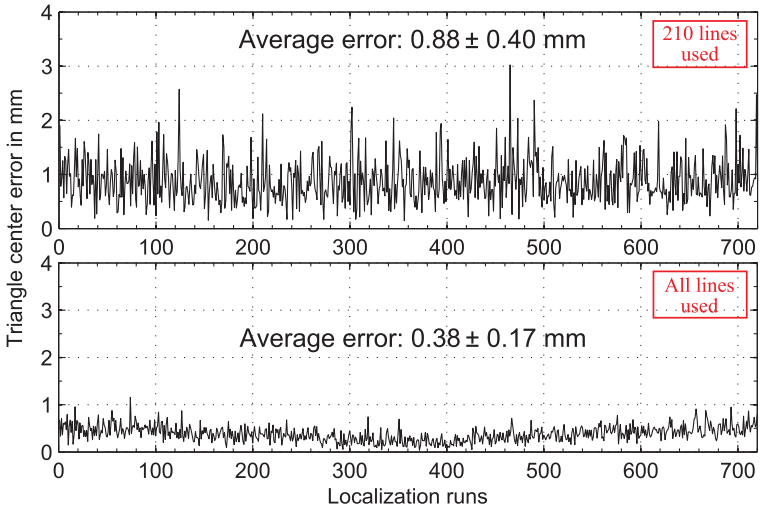

Figure 4.7: The triangle center error in every localization run when only 210 lines (top) or all 2410 lines (bottom) are used in each localization time interval.

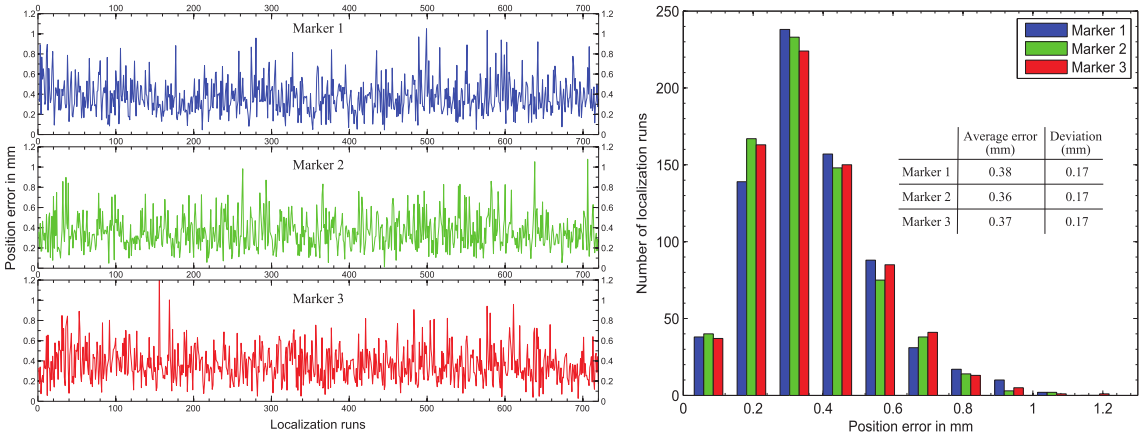

Figure 4.8: Position error of each marker in every localization run (left) with a histogram of the markers' position errors throughout 720 localization runs (right).

75% coincidence lines remain after applying the corrupted line removal method explained in Section 3.4.1. This fraction is almost the same as the rate of 73.1% true coincidence lines reported in GATE. The triangle centroid finding method successfully locates the triangle centroid in every localization run with an average error of 0.88 mm when 210 lines are used. The error could be improved to 0.38 mm when all 2410 lines are taken into account as shown in Fig. 4.7. However, the computational time is increased from 1.3 ms to 20.3 ms due to the large number of input data (computed by a 2.8 Ghz Intel Core i7 processor).

4.3.2.2 Position and orientation error

After the positions of the markers have been initialized by the initialization method in approximately 0.5 s for the first localization run, the Fuzzy C-mean clustering algorithm starts assigning the markers to their respective cluster of coincidence lines. For other localization runs, the prior knowledge of the markers' positions is used as initial points for the posterior run. With 210 coincidence lines (nearly 53 true coincidence lines for each marker) being used in each localization time interval, all three markers were localized successfully without any failures every 50 ms. On average, the whole algorithm takes 2.5 ms to complete locating three markers for each localization run.

In the GATE simulation, 3D locations of all annihilation events that occur during the capsule movement can be stored. The center of mass of these locations in each localization run is considered to be the true position of the marker. This information is then compared with the estimated position computed by the tracking algorithm to evaluate the position error of each marker. As seen in Fig. 4.8, the tracking algorithm achieves high accuracy with an average position error of approximately

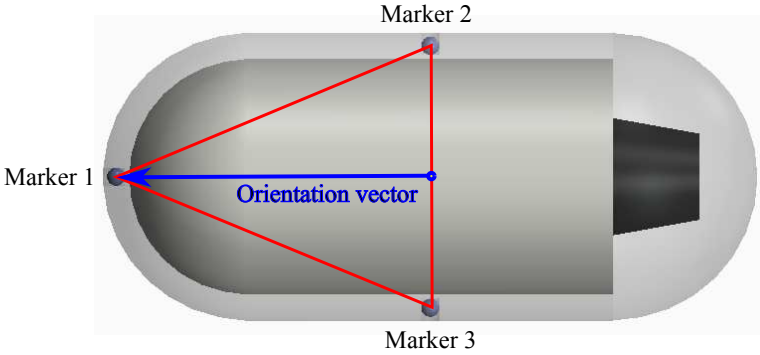

Figure 4.9: An orientation vector of a PECapsule.

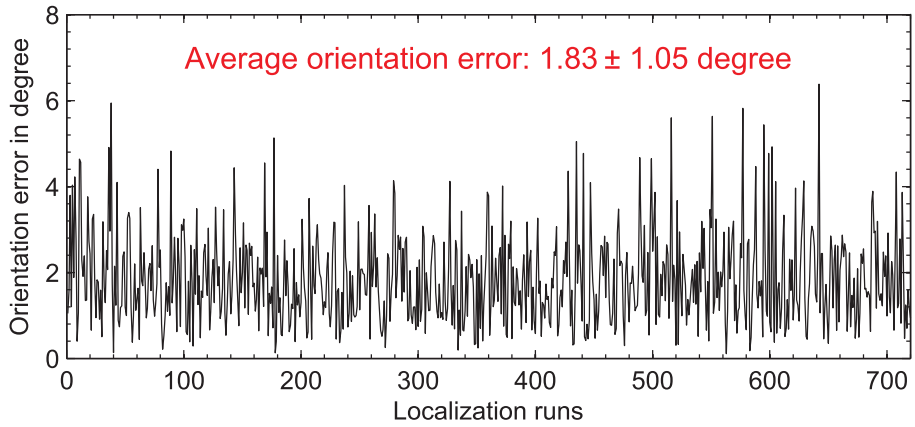

Figure 4.10: Orientation error of the capsule in every localization run.

0.37 mm ± 0.17 mm. In addition, Table 4.1 shows the estimation error of each marker's position in each XYZ axis. It seems that the error in the Z axis (i.e. the main axis of the detector system) is lower than that of the X and Y axes.

Based on the configuration of the markers in the capsule body as shown in Fig. 4.9, the centroid of the capsule is also the midpoint of the segment connecting the two closest markers. The other marker, which is furthest away from these two markers, lies on one tip of the capsule. Therefore, a vector that originates from the midpoint between the two closest markers to the furthest marker can be considered as an

Table 4.1: Estimation error of each marker's position in each XYZ axis.

Markers	Axes	Average error (mm)	Standard deviation (mm)
Marker 1	X	0.0097	0.2652
	Y	-0.0088	0.2395
	Z	-0.0035	0.2084
Marker 2	X	0.0184	0.2585
	Y	-0.0061	0.2515
	Z	0.0135	0.1648
Marker 3	X	0.0279	0.2589
	Y	-0.0260	0.2628
	Z	0.0028	0.1651

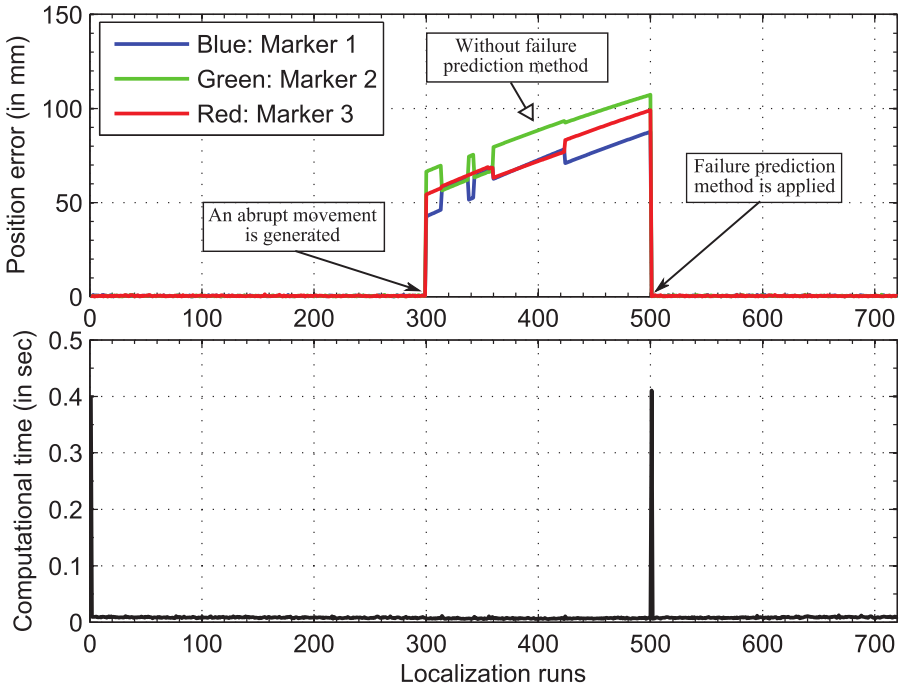

Figure 4.11: Markers' position errors (top) and computational time (bottom) with and without failure prediction method.

orientation vector of the capsule. The true orientation vector can thus be calculated in every localization run using the true positions of the markers. The different angle between a true orientation vector and an estimated orientation vector is considered as the orientation error of the capsule. As illustrated in Fig. 4.10, the average orientation error of the capsule is approximately 1.8°.

4.3.2.3 Failure prediction and initialization

In order to evaluate the effectiveness of the failure prediction method, an abrupt movement of the capsule is generated at the beginning of the 300th localization run. The capsule is suddenly dragged 50 mm away from its previous position. Without the failure prediction method, the Fuzzy C-mean clustering algorithm fails to locate the three markers. This is understandable as the initial values, which are based on previous markers' positions, are unreliable in this case (50 mm away). As a result, the markers' position errors are increased from an average of 0.4 mm to 50 mm. Since the failure is not detected, wrong initial values are continuously fed into the tracking algorithm. The position errors, therefore, increase in each subsequent localization, as shown in Fig. 4.11.

At the beginning of the 500^{th} localization run, the failure prediction method is added to the tracking algorithm. This additional check immediately detects a potential failure and stops the use of prior data as initial values for the current localization

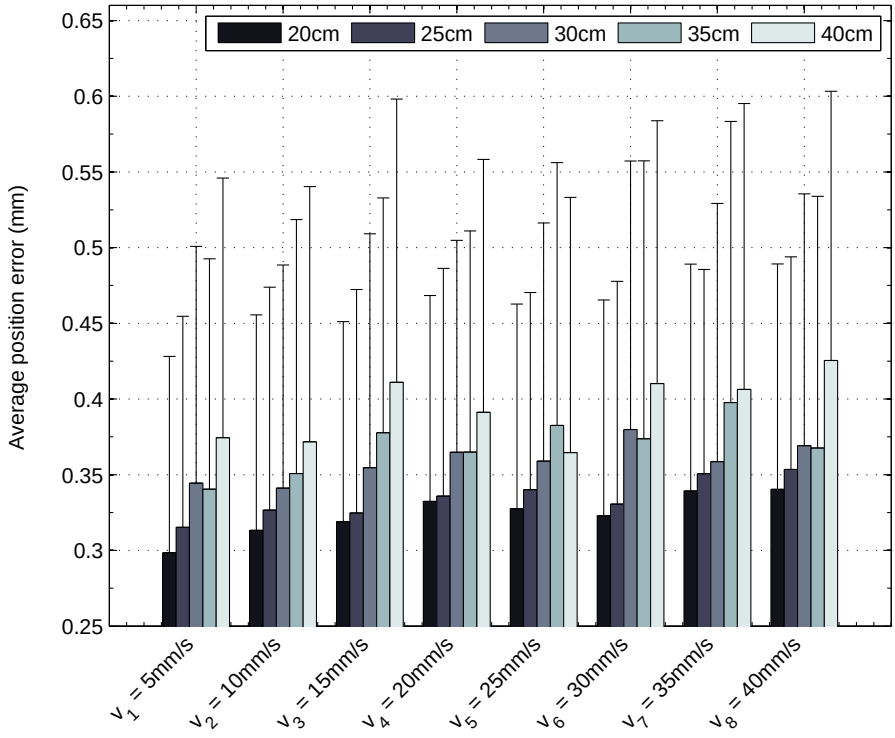

Figure 4.12: Average position error of the capsule over an entire dataset versus movement speeds of the capsule and phantom sizes. Five bars in each group represent five different diameters of the phantom (from 20 cm to 40 cm). One-side error bar is placed on the top of the main bar, which represents the standard deviation of the position error in one dataset.

run. The initialization method is then activated to estimate new initial inputs for the Fuzzy C-mean clustering algorithm. This procedure takes 0.41 s (shown as a surge on the bottom plot in Fig. 4.11) before the markers are back on track with a similar accuracy as the first 300 runs. This demonstrates the necessity and effectiveness of the failure prediction method in maintaining a high accuracy for the localization procedure.

4.3.2.4 Effect of phantom size and capsule movement speed on the tracking accuracy

Scattering of gamma rays in a patient's body affects the tracking accuracy. Scattering occurs more often in a larger patient's body than in a smaller body, thus different dimensions of the phantom are simulated to evaluate the effect of a patient's girth on the tracking performance. The phantom diameters considered are 20 cm, 25 cm, 30 cm, 35 cm, and 40 cm. As can be seen in Fig. 4.12, the average position error of an entire simulation is higher when the phantom's diameter is increased. This is because the larger the diameter of the phantom is, the more scattered coincidence events occur, or in other words, the less true coincidence lines being obtained. Re-

ported in GATE, the average percentage of true coincidence events in one entire simulation was 73.1%, 65.4%, 58.8%, 52.6%, and 47.3% when the phantom's diameter varies from 20 cm to 40 cm, respectively. Due to both attenuation and scattering characteristics of gamma rays, the total number of coincidence lines detected in each localization time interval is decreased in relation with the increase of the patient's size. Therefore, for comparison purposes the results shown in Fig. 4.12 are generated using all coincidence lines collected in one localization run instead of only 210 lines per run as previously.

In this section, the effect of the movement speed of the capsule on the tracking performance is also investigated. The capsule moves along the same trajectory as previously, however eight different movement speeds are simulated, which are 5 mm/s, 10 mm/s, 15 mm/s, 20 mm/s, 25 mm/s, 30 mm/s, 35 mm/s, and 40 mm/s orbiting around the z axis, combined with 2.5 mm/s, 5 mm/s, 7.5 mm/s, 10 mm/s, 12.5 mm/s, 15 mm/s, 17.5 mm/s, and 20 mm/s translation along the z axis, respectively. As shown in Fig. 4.12, the speed of the capsule movement has a slight effect on the tracking accuracy. The average position error becomes slightly higher when the capsule moves faster. In addition, the results have demonstrated a high reliability of the tracking algorithm as three markers are successfully located in the worst case when the thickest patient's body (40 cm) and the highest movement speed (40 mm/s) are simulated.

4.3.3 Performance comparison between the full-ring scanner and a smaller detector system

In the previous section, the performance of the tracking algorithm when a full-ring scanner is used has been evaluated. As mentioned above, the proposed localization method for WCE does not require a full-ring geometry, thus a second simulation dataset using a smaller detector system with two pairs of detector modules (as shown in Fig. 4.2) has been created to evaluate how a smaller detector geometry affects the tracking performance. The performance comparison between these two detector systems is presented in this section.

Due to the decreased number of the crystals, only 204,484 coincidence lines are recorded (when the phantom diameter is 20 cm) throughout 720 localization runs in this simulation (i.e. an average of 284 lines per run). Again, 210 lines out of 284 lines are input to the tracking algorithm in each localization run to speed up the algorithm computation. Fig. 4.13 illustrates a visual comparison between the coincidence lines collected in this simulation and those collected by the full-

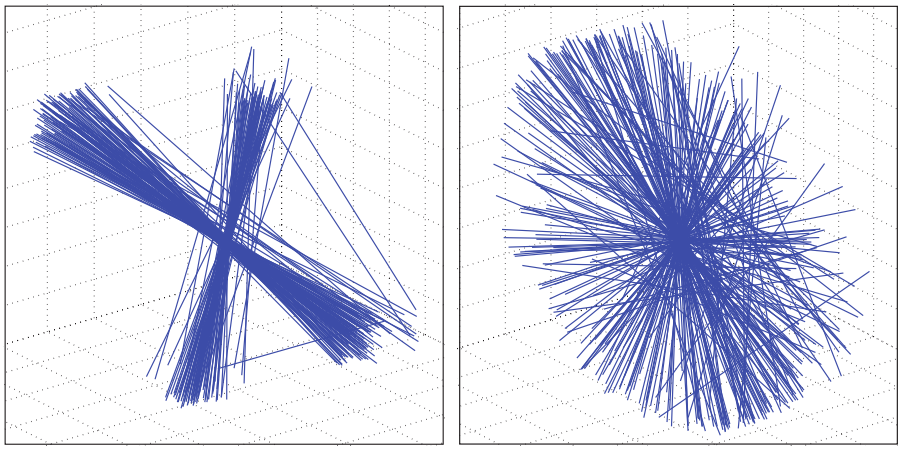

Figure 4.13: Coincidence lines collected by a small detector system (left) and by a full-ring scanner (right).

ring scanner. After the tracking algorithm is implemented, the average position error obtained is reduced slightly. The position errors of the three markers are 0.36 mm ± 0.18 mm, 0.36 mm ± 0.19 mm, and 0.35 mm ± 0.17 mm, respectively, and the success rate is maintained at 100%.

There are two reasons for why the average position error is slightly smaller than previously achieved when a full-ring scanner is used. Firstly, this is because of the increase in the true coincidence rate as shown in Table 4.2. Given a smaller number of detector blocks (4 compared to 28), the possibility of detecting scattered coincidence and random coincidence by the smaller detector system is reduced. Secondly, regardless of how many coincidence lines are recorded totally in each localization run, the same number of lines (210) is fed to the tracking algorithm for both datasets.

Table 4.2: A comparison between the full-ring scanner and a small detector system in the number of total coincidence lines, the number of true coincidence lines, the true coincidence rate, and the average number of coincidence lines in each localization run when different phantom sizes are simulated.

Phantom diameters (cm)	Detector systems	Number of total lines	Number of true lines	True coincidence rate (%)	Average number of lines per run
20	Full ring	1,735,600	1,268,390	73.1	2,410
	Reduced	*204,484*	*167,512*	*81.9*	*284*
25	Full ring	1,147,045	750,291	65.4	1,593
	Reduced	*131,947*	*100,194*	*75.9*	*183*
30	Full ring	768,010	451,483	58.8	1,067
	Reduced	*86,376*	*60,593*	*70.2*	*120*
35	Full ring	519,842	273,639	52.6	722
	Reduced	*57,360*	*36,809*	*64.2*	*80*
40	Full ring	354,354	167,442	47.3	492
	Reduced	*38,547*	*22,800*	*59.2*	*54*

Table 4.3: Effect of decreasing average number of coincidence lines per run to below 210 on the tracking performance when the reduced geometry is used.

Average number of lines per run	Average position error			Number of failed runs
	Marker 1 (mm)	Marker 2 (mm)	Marker 3 (mm)	
284	0.36 ± 0.18	0.36 ± 0.19	0.35 ± 0.17	0
183	0.41 ± 0.20	0.40 ± 0.22	0.39 ± 0.21	0
120	0.61 ± 0.67	0.56 ± 0.35	0.58 ± 0.64	7
80	0.78 ± 0.60	0.74 ± 0.61	0.70 ± 0.53	17
54	1.8 ± 3.6	1.4 ± 2.9	1.6 ± 3.2	118

Therefore, the tracking algorithm was implemented with a larger number of true coincidence lines for this simulation dataset.

Although the success rate using the reduced geometry (when the phantom diameter is 20 cm) is retained at 100%, the average number of coincidence lines recorded per run when a larger phantom diameter is used is expected to be less than the desired number of 210, which would decrease the tracking accuracy. Therefore, to evaluate how having less than 210 lines per run would affect the tracking performance, different phantom diameters have also been simulated. Table 4.2 presents a comparison in the number of coincidence lines and the true coincidence rate collected by both detector systems when different phantom diameters are used. As shown in Table 4.2, the average number of coincidence lines collected is reduced to 183, 120, 80, and 54 when the phantom diameters are 25 cm, 30cm, 35 cm, and 40 cm, respectively.

Reducing the average number of lines per run to less than 210 has a negative effect on the tracking accuracy. Table 4.3 presents the average position error of each marker corresponding to the decreasing average number of lines per run collected by the smaller detector system. With a decreasing number of lines input to the algorithm, the marker's position error increases significantly, especially for the case of 54 lines per run. The success rate also decreases from 720/720 to 602/720. The localization is considered a failure when the position error of any marker is larger than 3mm. Due to the localization failure which results in an extremely large position error, the standard deviation of the position error is higher than some of the average position error depicted in Table 4.3.

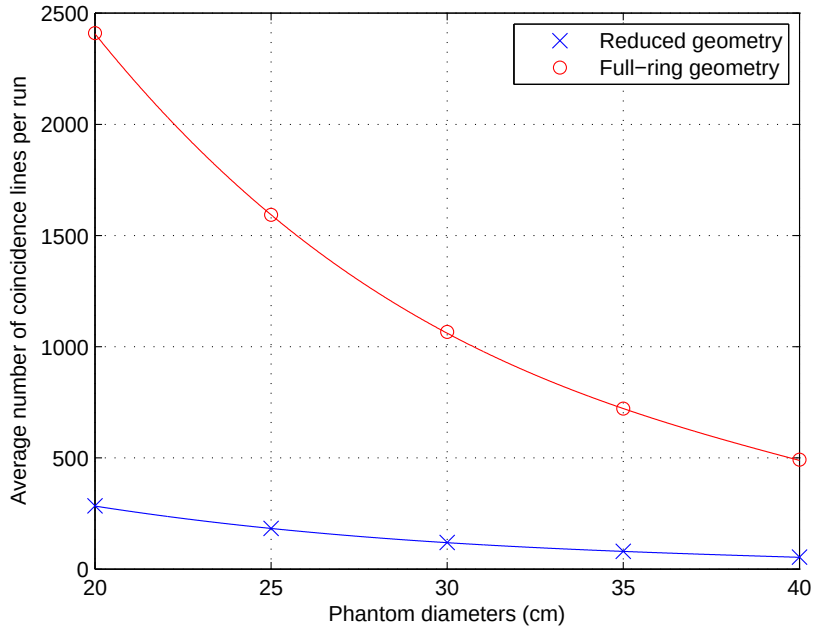

Figure 4.14: Average number of coincidence lines collected in each localization run by both scanners when different phantom diameters are simulated. These data, obtained when the activity of the isotope is set to 1.85 Mbq/marker, are fitted in two third-order polynomial curves colored correspondingly.

4.3.4 Marker activity selection

In order to ensure that sufficient coincidence lines are input to the tracking algorithm in every localization run when the smaller detector system is used, the activity of the markers needs to be chosen appropriately. Depending on the tracking frequency and the phantom size, the minimum activity requirement of the isotope contained in the markers can be approximated by

$$A_{min} = 1.85 \times \frac{f}{20} \times \frac{210}{n(d)} \tag{4.1}$$

$$= \frac{19.425 \times f}{n(d)} \quad \text{(MBq)} \tag{4.2}$$

where 1.85 MBq, 20 Hz, 210 lines are the activity, the tracking frequency and the desired number of lines per run chosen in this study, f is a required tracking frequency, and n(d) is the number of lines per run corresponding to a required phantom diameter (d) that can be selected from the fitted curves as shown in Fig. 4.14.

4.4 Voxelized phantom simulation

In the previous section, the tracking performance of the proposed localization method has been evaluated using the data obtained from the simulations with geometric phantoms. In this section, a new simulation dataset in which the capsule moves inside a more realistic human phantom, a 4D extended cardiac-torso (XCAT) phantom, is performed.

As has been presented above, the reduced detector system with two pairs of detector modules can provide similar tracking performance as the full-ring scanner as long as a sufficient number of coincidence lines (approximately 210 lines) are input to the tracking algorithm in each localization run. Therefore, in this new simulation dataset, only the reduced detector system is used to detect the gamma rays generated from the capsule.

4.4.1 Simulation procedure

Most of the steps of the GATE simulation architecture are retained as previously. However, the steps of setting up the phantom and the movement of the capsule are changed. Since geometric phantoms can be created by GATE itself while voxelized phantoms are generally imported using external data, setting up the phantom in this simulation is more complicated. This is explained in detail in the following subsections.

4.4.1.1 Voxelized phantom

Digital phantoms that provide virtual models of a patient's anatomy and physiology have been used and developed extensively in the past. They are generally used for computer-based simulations in many areas such as radiography, radiotherapy, nuclear medicine, and radiation protection [114]. These anatomically realistic phantoms can either be defined by mathematical equations (called mathematical phantoms) or voxel-based volume arrays (called voxelized phantoms).

In mathematical phantoms, the internal organs and tissues are modeled using mathematical functions or simple geometric primitives. Therefore, the organ shapes can be altered easily to model anatomical variations by applying a set of transformations to the original anatomies of the phantom. However, due to the simplicity of the mathematical equations that cannot accurately conform to the shape of real organs, the mathematical phantoms are not entirely realistic. Figure 4.15 shows

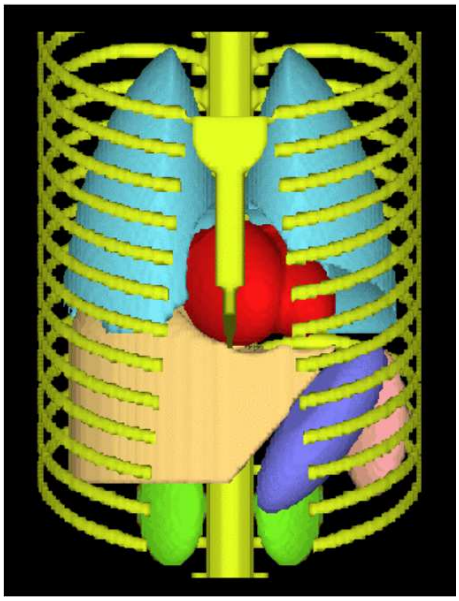

Figure 4.15: An example of a mathematical phantom: MCAT phantom [115].

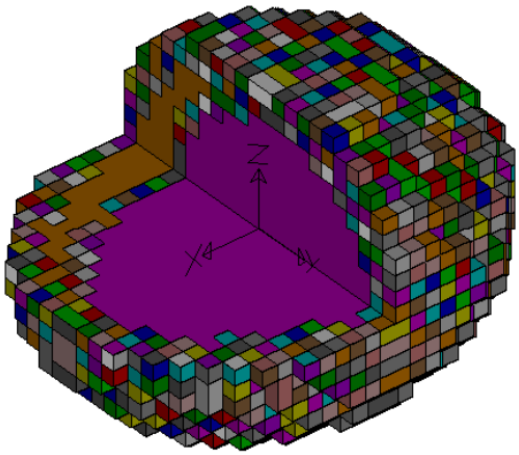

Figure 4.16: An example of a voxelized phantom [116].

3D surface rendering of the MCAT (Mathematical Cardiac-Torso) phantom [115], a mathematical phantom.

Alternatively, voxelized phantoms are human models based on 2D patient data obtained from MRI (magnetic resonance imaging) slices or CT (computed tomography) images. Pixels of a cross-sectional image can be extended into the third dimension to become cuboidal volume elements (called voxels). Each voxel is assigned a unique identifier or color depending on which particular organ or tissue it belongs to (segmentation process). A voxelized phantom is a 3D union of voxels of the same size. With the advancement of the medical imaging technology, high resolution MRI or CT images can now be produced. Therefore, voxelized phantoms are currently the most precise representation of the human anatomy. Figure 4.16 shows an example of a voxelized representation of an organ.

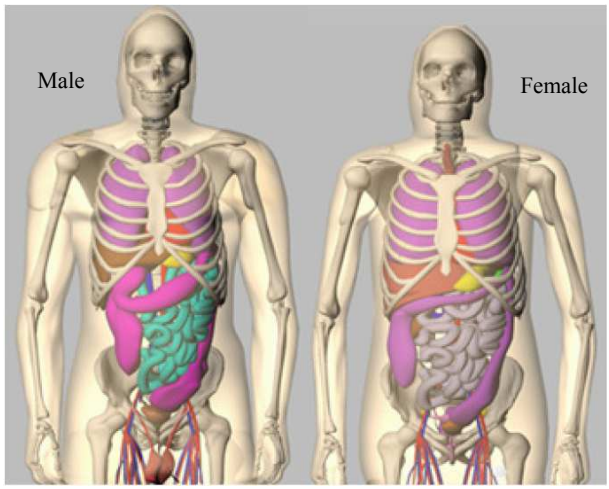

Figure 4.17: 3D renderings of male and female voxelized phantoms generated by XCAT v1.0 program [110].

One limitation of the voxelized phantoms is that they are not as flexible as mathematical phantoms in term of modeling anatomical variations. This is because of the fact that they are fixed to a particular patient anatomy that used to provide the patient data. To model a patient population, a number of different patient datasets need to be obtained which would be very time-consuming and require a lot of effort. Therefore, "hybrid" phantoms that take advantage of both the realism of a voxelized phantom and the flexibility of a mathematical phantom have been developed [115].

4.4.1.2 XCAT phantom

In this study, the voxelized phantom used for simulations is generated by the XCAT v1.0 program [110], a "hybrid" phantom generation program. Based on a variety of parameters defined by users, XCAT generates a corresponding voxelized phantom as shown in Fig. 4.17. The parameters that the users are able to modify can be seen in Appendix B. The XCAT phantom has been one of the most popular voxelized phantoms to be used in nuclear medicine. In addition, the phantom includes the model of a GI tract which is essential for the simulation in this study.

The main specifications of the voxelized phantom created in the simulation is detailed in Table 4.4. The output produced by the XCAT program is a 3D (32 bit float) binary image. Each data element of the 3D image represents a voxel of the voxelized phantom. The value of each element is the gamma-ray attenuation coefficient of the tissue or organ that the corresponding voxel belongs to. For example, the values of the elements that represent the voxels of the heart and the lung are approximately 0.0780 and 0.0215 cm^{-1} per voxel, respectively.

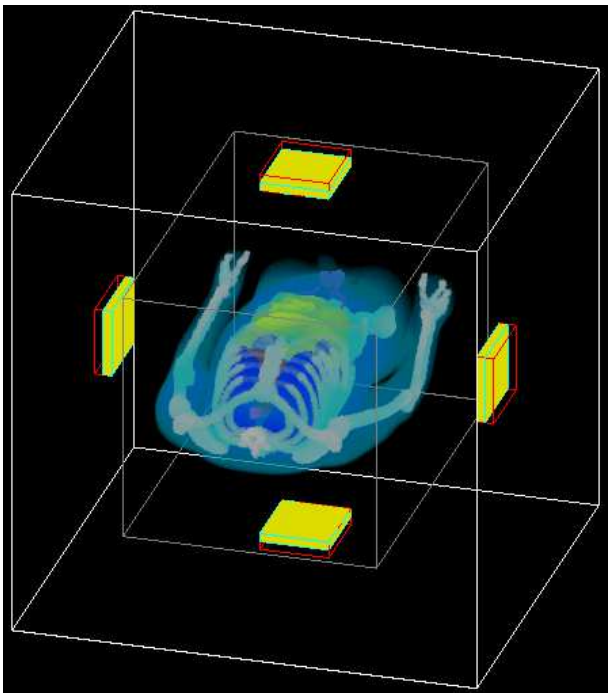

Figure 4.18: Visualization of the simulation with XCAT phantom.

4.4.1.3 Importing XCAT phantom into GATE

GATE is able to read voxelized phantom data stored in several medical image file formats such as ASCII, Interfile, Analyze, and Metalmage. The voxelized phantom imported into GATE is considered a inhomogeneous anthropomorphic attenuation map. Using a range translator, the value of each element of the 3D image (i.e., voxel value) can be converted to a material name listed in GATE's built-in material database.

Table 4.4: Main specifications of the voxelized phantom used in this study.

Parameter name	Value
Gender	Male
Body transverse length	34.5 cm
Body anterior-posterior length	27.5 cm
Body height	192 cm
Body weight	95.05 kg
Pixel width	0.4 cm
Slice width	0.4 cm
Array size	150
Start slice	235
End slice	412

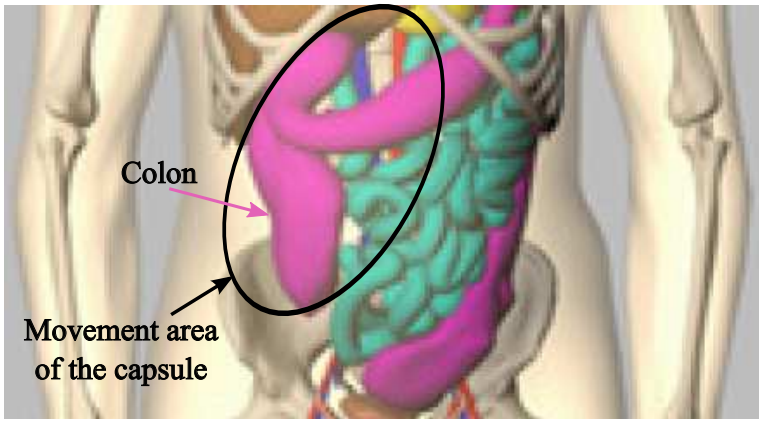

Figure 4.19: An intestinal section that the capsule moves inside in the simulation.

Since GATE can only read 16-bit unsigned integer data, the voxelized phantom is first converted from 32-bit float data into 16-bit unsigned data using Matlab. Next, the raw binary data are converted to the Interfile file format for GATE to read. This conversion step can be performed by using XMedCon, an open-source medical image conversion toolkit. A range translator is then created to translate the voxel values (i.e., attenuation coefficients as mentioned above) into different material names listed in the GATE materials database. Figure 4.18 presents the visualization of the simulation after the XCAT phantom has been imported into GATE.

4.4.1.4 Capsule movement

After the step of setting up the phantom is completed, a model of the capsule carrying the three ^{22}Na markers is built. This model is created in the same way as in the previous simulations using geometric phantoms. However, instead of having a simple orbiting trajectory as previously, the capsule in this simulation needs to move along the inside of the GI tract of the XCAT phantom.

Most of the sections in the GI tract of a human body are very narrow, especially the small intestine. Similar to the way food is moved in the digestive system, the capsule is squeezed and pushed through the GI tract by peristalsis. However, this cannot be done in the simulation as the generated phantom is a static model. The narrow intestinal sections are unable to dilate to allow the capsule to pass through. In addition, the small intestine folds upon itself many times, making the modeled capsule impossible to turn without overlapping the intestine.

For these reasons, the simulation was only performed with the capsule moving along the colon (shown as a purple tubular section in the black ellipse in Fig. 4.19). This is because the internal diameter of the colon in the generated XCAT phantom is much larger than the diameter of the modeled capsule. Therefore, there is enough space for

the capsule to move and turn in this section. The capsule movement created in the simulation is a generic movement comprising of several basic movements provided in GATE such as translation, orbit, and rotation. The capsule is moved with a velocity of 1 mm/s to make it similar to the case of a passive WCE traveling inside a human body.

The main factors affecting the accuracy of the localization method are the attenuation and scattering effects when gamma rays emitted from the capsule pass through a human body. In terms of attenuation and scattering, the medium inside the colon and other sections of the GI tract are almost the same. The gamma rays would have to penetrate the same organs or tissues before reaching the detectors. Therefore, the tracking performance obtained from the simulation with capsule movement in the other parts of the GI tract is expected to be similar with what could be achieved in the colon.

According to the thickness of the generated XCAT phantom (see Table 4.4) and the equation for choosing marker's activity in (4.2), the activity of each marker is chosen as approximately 5.5 Mbq to ensure that sufficient coincidence lines are input to the tracking algorithm in each localization run.

4.4.2 Running simulations on UOW HPC cluster

Since GATE, based on Monte Carlo method, is able to simulate the entire process of producing a LOR from the interaction and transportation of electrons, positrons, and photons to the detection of coincidence events, GATE simulation is generally very time consuming. Furthermore, the simulation using voxelized phantom takes much longer due to the high number of voxels contained in the phantom. With the parameters chosen in Table 4.4, the XCAT phantom used in the simulation consists of $150 \times 150 \times (412 - 235 + 1) = 4,005,000$ voxels. It takes approximately 12 hours to complete 5-second simulation by a single computer having a 2.8 Ghz Intel Core i7 processor and 8 GB memory. Therefore, it would take weeks or months to compute the simulation in which the capsule completes its entire movement trajectory specified in Section 4.4.1.4. This demonstrates the fact that the computational task is beyond the capability of only a single computer.

To overcome this computational issue, the UOW HPC (High Performance Computing) cluster, provided by Academic Computing and Innovation Unit, Information Technology Services, University of Wollongong, was employed to execute the simulation. As shown in Table 4.5, there are 22 nodes in the cluster, and each node consists of 64 cores which results in a total of 1408 cores. However, GATE is not a

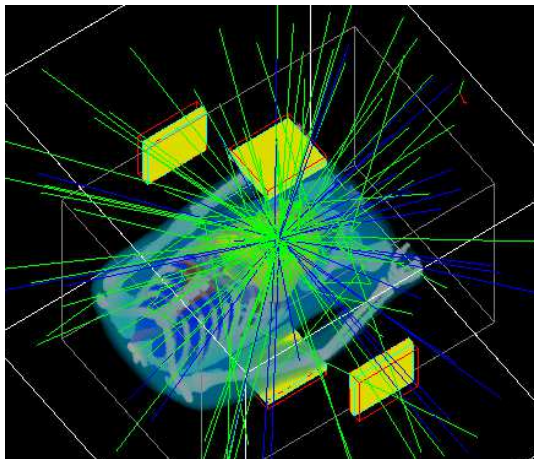

Figure 4.20: Gamma rays are generated from a capsule containing three ^{22}Na markers moving inside a XCAT phantom in a GATE simulation.

parallelized program, running GATE on multiple cores does not help speed up the simulation. A solution for this is to use the cluster tools (job splitter and file merger) provided in GATE to subdivide the simulation macro into a number of fully resolved, non-parameterized sub-macros. Each sub-macro is then executed independently on one core. The ROOT output files obtained from all the sub-simulations are merged into a final ROOT output file. Since the cluster is shared between many users, a maximum of 80 cores can be used by one user at a time. The overall execution time of the simulation can thus be reduced by up to 80 times. Figure 4.20 presents the visualization of the simulation when it is executed.

Table 4.5: Specifications of the current UOW HPC cluster.

Parameter name	Value
Compute Node Model	Dell PowerEdge C6145
Processor Model	16-Core 2.3 GHz AMD Opteron 6376
Processors per Node	4
Cores per Node	64
Memory per Node	256 GB
Number of Nodes	22
Total Cores	1408
Total Memory	5,632 GB
Network Connection	10 GbE
Operating System	CentOS 6.3
Queue System	Torque
Job Scheduler	Maui
Storage Capability	120 TB

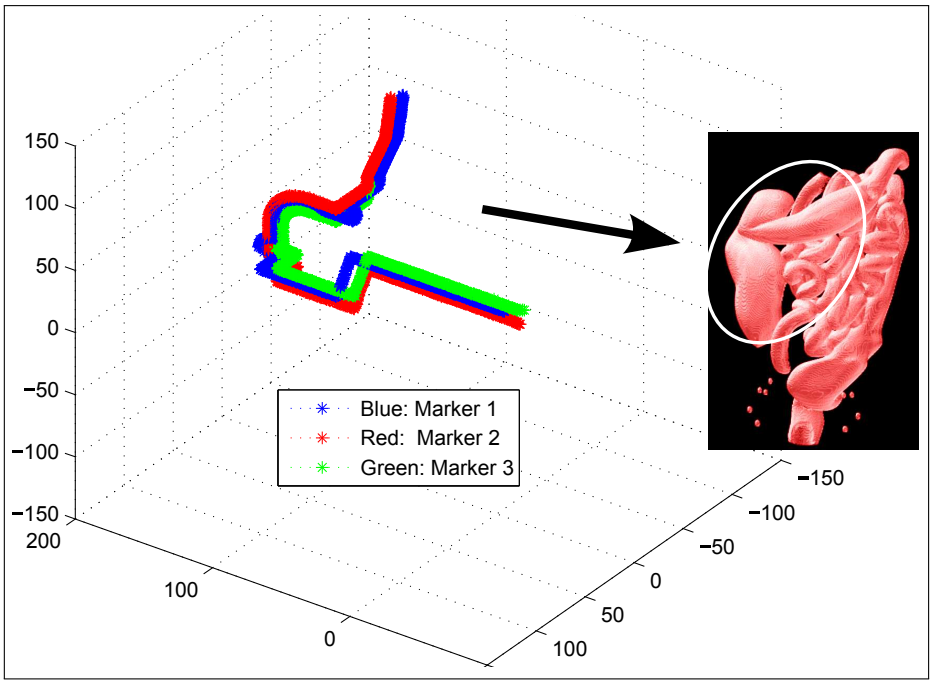

Figure 4.21: Computed 3D positions of the markers in all localization runs using data obtained from a voxelized phantom simulation, and 3D rendering of the GI tract of the XCAT phantom created by Amide software.

4.4.3 Results

With the capsule speed chosen above, it takes 471 seconds for the capsule to travel through the aforementioned colon section, the simulation time is thus set at 471 seconds. Hence, there are $471 \times 20 = 9420$ localization runs in the simulation. At the end of the acquisition, approximately 3.29 million coincidence lines are collected, leading to an average number of 349 coincidence lines per localization run. This average number of lines is sufficient for the tracking algorithm, and demonstrates that the activity level for the marker was chosen correctly.

Reported in GATE, approximately 2.02 million out of 3.29 million lines are true coincidence lines, thus the true coincidence fraction is 61.4%. This is understandable as the generated XCAT phantom is a large human phantom. As shown in Table 4.2, the true coincidence rate when a water geometric phantom with a similar diameter (35 cm) is simulated is 64.2%. This shows an agreement between the two simulation datasets. A slight difference between the two rates is due to the fact that some human organs have higher linear attenuation coefficients than water.

The simulation output data are converted and imported into Matlab for the implementation of the tracking algorithm. All of the coincidence lines collected in each localization run are used in the algorithm since the detector system simulated is already a reduced-geometry system and there is no need to compensate for the loss of

sensitivity. Figure 4.21 presents the 3D positions of the estimated markers for every localization run, which forms three trajectories having a similar shape to the colon section (highlighted in a white ellipse). Please note that the diameter of the capsule is very small compared to the width of the colon section in the XCAT phantom. Thus the shape of the movement trajectory does not have to be exactly the same as the shape of the colon as seen in Fig. 4.21.

The localization is observed to be successful in all 9420 localization runs. The plots of the position error of each marker, the orientation error of the capsule, the relative distances between the markers, and the computational time are illustrated in Fig 4.22. As shown in the figure, the maximum position error is approximately 4.5 mm, but the average error is less than 0.5 mm. Since there are a slightly more coincidence lines used in each localization run, the computation time per run is 3.3 ms compared to 2.5 ms in the previous simulation. The orientation error has a mean of 1.8° and a standard deviation of 1.2°.

4.5 Discussion and summary

The tracking algorithm developed in Section 3.4 is reliable in computing the position and orientation of the capsule. Owing to the effectiveness of the failure prediction method and the initialization method based on finding the center of the triangle, the localization was never observed to fail when a sufficient number of coincidence lines were collected in every localization run. Even in extreme cases where the capsule has an abrupt movement, the capsule can still be localized. The failure prediction method temporarily stops the use of the Fuzzy C-mean clustering algorithm in situations where initial positions of the markers are unacceptable, and waits until the initialization method is activated to provide more acceptable initial values to the clustering algorithm. In addition, given a reasonably accurate estimated position of the triangle centroid (an average position error of 0.88 mm as shown in Fig. 4.7), the initialization method is likely to generate adequate initial values.

Due to safety and patient comfort requirements, the capsule must not be allowed to move too fast inside the GI tract. Additionally, abrupt capsule movement can be detected effectively by the failure prediction method. Therefore, the tracking frequency used need not necessarily be as high as the frequency of 20 Hz used in this study. With a lower tracking rate, i.e. longer sampling time, the same level of activity of the marker will provide a proportionally higher number of coincidence lines collected in each localization run. The activity of the marker can thus be chosen at a lower value. However, for larger patients, the activity would have to be

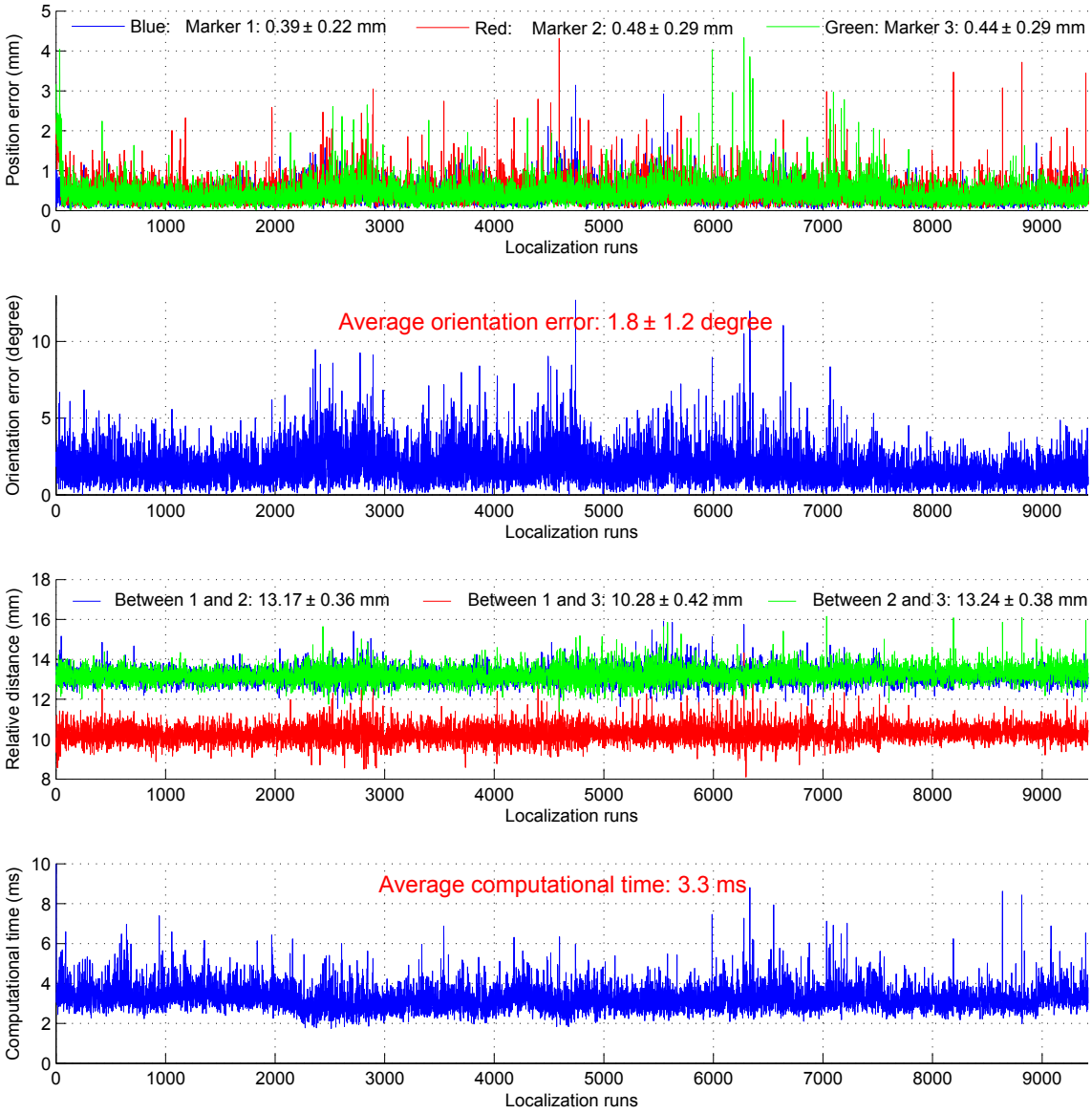

Figure 4.22: Plots of position error of each marker, orientation error of the capsule, relative distances between the markers, and computational time in every localization run.

increased to compensate the gamma rays that attenuate and scatter in the patient's body to ensure a sufficient number of coincidence lines are input to the tracking algorithm. Moreover, lower tracking frequencies would, to some extent, decrease the tracking accuracy.

One typical limitation of the conventional PET imaging technique is the field of view (FOV) constraint, in which radioactive sources that fall beyond the FOV would not be imaged. Similarly, in this localization method, the capsule would not be localized once its movement exceeds the FOV (illustrated as a volume inside the red box in Fig 4.23). However, thanks to the real-time tracking (a tracking frequency of 20 Hz in this study), this limitation can be overcome. Being located in real-time, it is possible to ensure that the capsule is always within the FOV. When the capsule

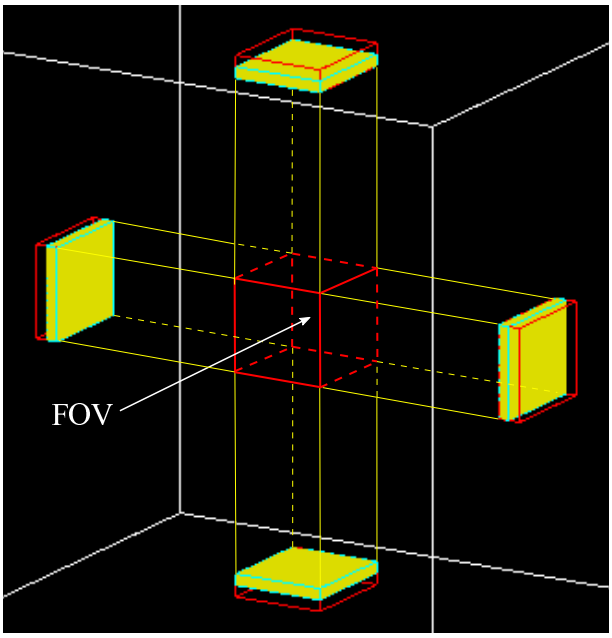

Figure 4.23: Field of view of the reduced detector system.

is close to the boundary of the FOV, the patient bed can be moved accordingly so that the current capsule position is approximately at the center of the FOV. In commercial PET systems, the patient bed position can be manipulated precisely in all lateral, vertical and longitudinal directions. The subsequent calculation to estimate the capsule's localization information is then compensated by adding the translation vector of the patient bed movement to the coordinates of the reference coordinate system.

Another important point that can be made from the above discussion is that in practice the size of each of the four detector blocks may be reduced to be smaller than has been simulated in this chapter. As shown in Fig 4.23, the volume of the FOV is dependent on the surface area of the detector blocks. If the capsule does not move very fast and the patient bed movement is controlled automatically to force the capsule to always be near the center of the FOV, using a smaller FOV would still deliver similar tracking performance. Accordingly, the number of crystals used in each detector block may be decreased. Since the proposed active WCE has not been available yet, the maximum speed of the capsule is unknown. Therefore, it would be impossible to determine an optimal size of the detector blocks at the time of writing.

Chapter 5

Experimental Evaluation

5.1 Introduction

In the previous chapter, the proposed localization method for WCE has been validated using simulation data obtained from the GATE toolkit with both geometric phantoms and a realistic XCAT phantom. The purpose of this chapter is to experimentally evaluate and quantify the performance of the localization method (i.e. determining the position and orientation of a capsule endoscope accurately).

Since the reduced-geometry detector system mentioned in Chapter 4 is not yet available in practice, the experimental validation was conducted using clinical PET scanners. For these experiments, an experimental apparatus was designed and fabricated using high-resolution 3D printers to create a predefined track for the capsule to move along inside a water phantom. Using this apparatus, the experiments were conducted in two different commercial PET scanners: Philips TF64 and Philips Allegro (Philips Medical Systems, Cleveland, USA). The data obtained from the experiments were then converted to have a usable data format before being used for the implementation of the tracking algorithm in Matlab. In this chapter, the experimental design and procedures are described. The data post-processing and the performance evaluation of the tracking algorithm are then presented.

5.2 Experimental apparatus

An ideal experiment would require a real patient to swallow a PEcapsule and a small detector system with 2 pairs of detector modules to be placed surrounding the patient's body to detect the gamma rays originating from the PEcapsule. However,

this is not possible in the proof-of-concept study in this thesis. Therefore, an experimental apparatus was fabricated to mimic the scenario in which a capsule carrying three positron emission markers moves inside a patient's body. Consequently, the design of the apparatus needs to satisfy the following criteria:

- A phantom filled with water is essential to imitate the photon attenuation properties of the human body. In PET, water phantoms are often used since gamma rays encounter similar attenuation and scattering characteristics when they travel through a patient's body.
- The capsule carrying the markers is able to move automatically in linear and non-linear trajectories with different orientations inside the enclosed water phantom.
- For performance evaluation, there needs to be a way to determine the actual position and orientation of the capsule during the experiments (visually, for example) in order to compare the actual data with estimated data obtained by the tracking algorithm.
- The testing procedure can be conducted repeatedly multiple times without the need for opening/closing the water phantom for re-assembling or calibrating the internal components in the phantom.

Based on these requirements, the experimental design was as follows.

5.2.1 Radioactive markers

In the experiments, three commercial spot markers MMS09 (Eckert & Ziegler Isotope Products Inc, US) were used (Fig. 5.1A) . Each marker contains 0.25 mm-diameter spherical radioactive core of ^{22}Na encapsulated at the centroid of a cubic acrylic cover with a size of 10 x 10 x 10 mm. The cover is used to seal the active core and to make the handling easier. The radioactivities of the markers on the day of experiment were measured as 1.60 MBq, 1.48 MBq and 1.47 MBq, respectively.

Although the size of the marker is larger than the conceptual design mentioned in Section 3.3.1 (due to the acrylic cover), this will not affect the proof-of-concept purpose of this study, or the feasibility of the proposed method. This is because the acrylic has very low gamma-ray attenuation coefficient and the two important factors (the size of the radioactive cores and their relative distances that would impact the tracking performance) are made exactly the same as in Fig. 3.6. In addition, the markers can be fabricated with custom designs using similar techniques that have been used to produce commercial brachytherapy seeds [96].

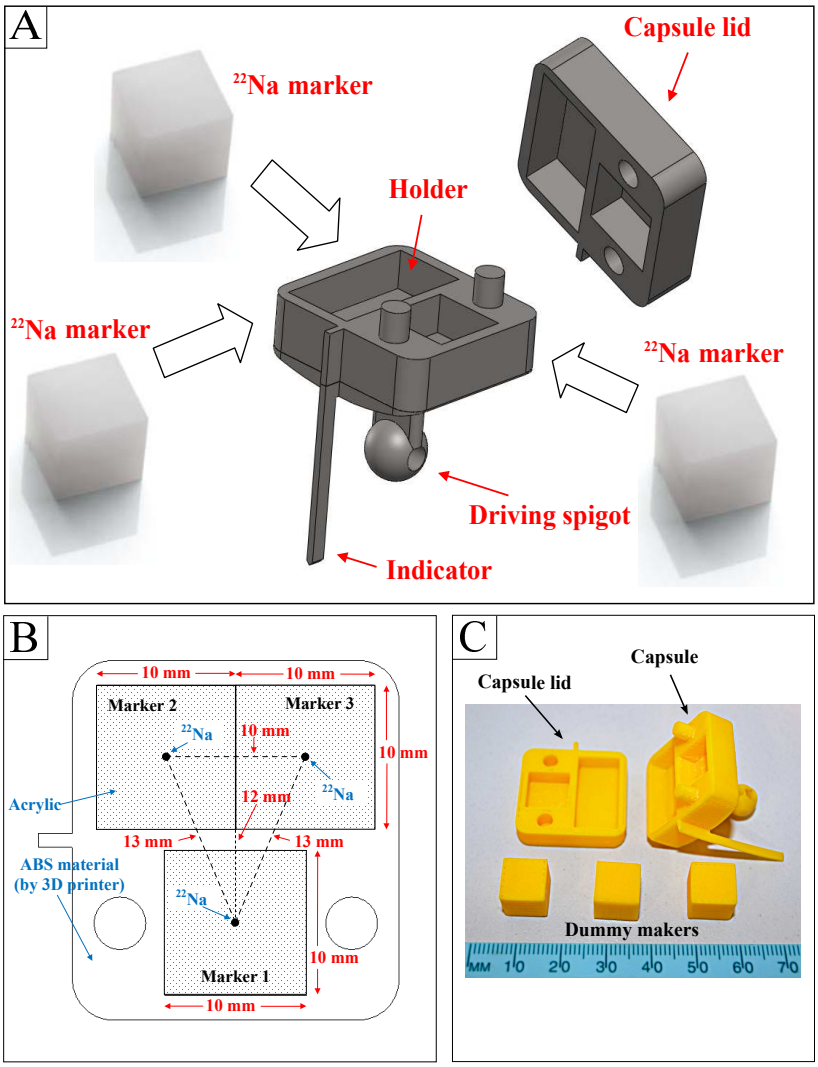

Figure 5.1: Design of the experimental capsule and markers. (A): 3D models of the capsule and markers. (B): 2D sketch of the top view of the capsule to show how the markers are arranged. (C): The size of a 3D-printed capsule with "dummy" markers for illustration

5.2.2 Experimental capsule

The tracking algorithm is able to localize not only a static capsule but also a moving one. Therefore, the experimental capsule was equipped with extra components for locomotion, which has not been available in commercial WCEs. The size of the experimental capsule in this study was not critical and thus not necessarily the same as that of commercial WCEs. The capsule has three parts: a driving spigot, a holder, and an indicator as shown in Fig. 5.1A. The driving spigot was connected with a cable through its center so that the capsule could be fed forward or backward along the track. The holder is able to retain the markers firmly, and to ensure their relative distances are always fixed at 13 mm, 13 mm and 10 mm respectively during the experiments. An indicator measures the position and orientation of the capsule when it moves along a designed track, and is described in more detail below.

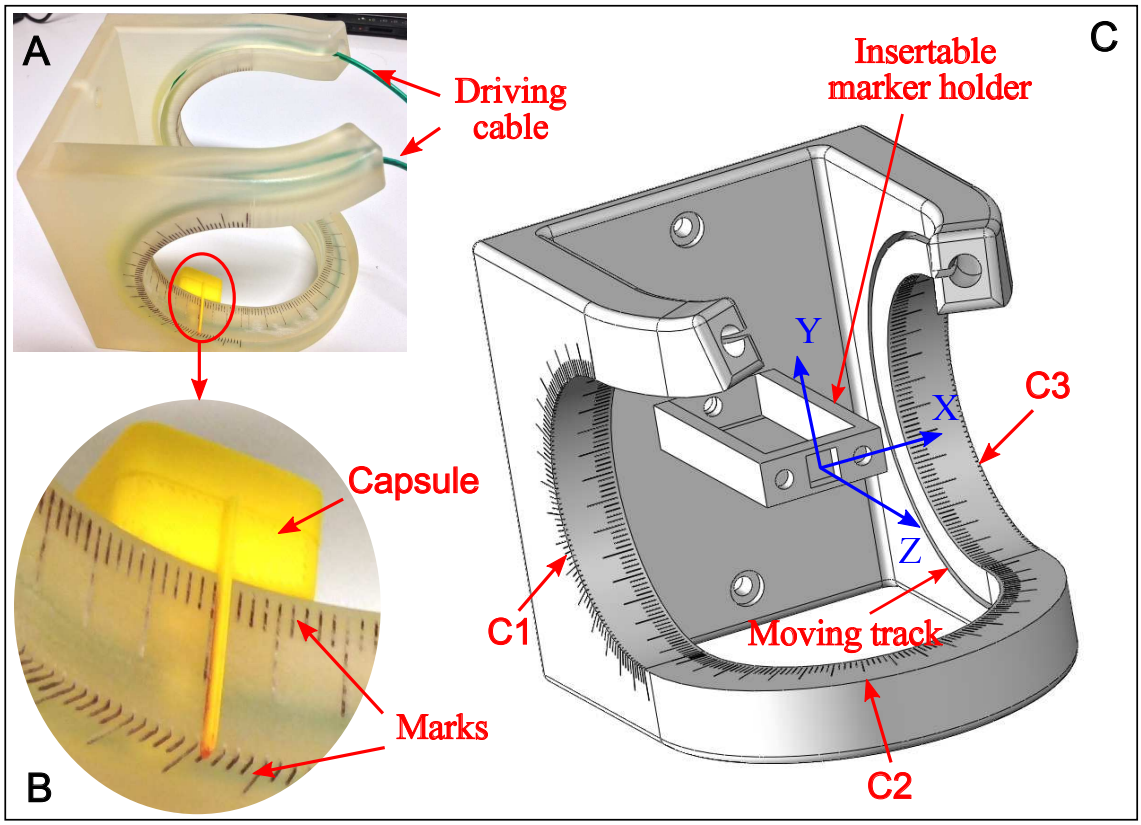

Figure 5.2: Design of the moving track. (A): A 3D-printed track along which a capsule attached with a driving cable moves. (B): The capsule is enlarged for clearer view of the indicator and the marks. (C): A 3D CAD model of the moving track. The track consists of three curves (C1, C2, and C3) which are three halves of three circles in the YZ, XZ, and YZ planes, respectively.

5.2.3 Moving track

In order to move the capsule along a known trajectory, a moving track was designed and printed by a 17 μm-resolution 3D printer (ProJet 3510 HDPlus Printer, 3D Systems Company) as shown in Fig. 5.2A. The cable attached to the driving spigot of the capsule was threaded through the entire captive track. By pulling each end of the cable, the capsule could be fed along the track in both directions. The track was composed of three halves of three circles (C1, C2 and C3) with diameters of 116 mm (in YZ plane), 112 mm (in XZ plane) and 116 mm (in YZ plane) respectively, as can be seen in Fig. 5.2C.

The two ends of the cable were connected to an external pulley system which has three pulleys with teeth as illustrated in Fig. 5.3. Each end of the cable went through each gap between the middle pulley and the other two pulleys. The middle pulley was driven by a DC motor. As soon as the motor operates, one end of the cable is pulled and the other end follows. A reversible speed controller, which controls the speed of the motor, allows the capsule to move with different speeds in opposite directions.

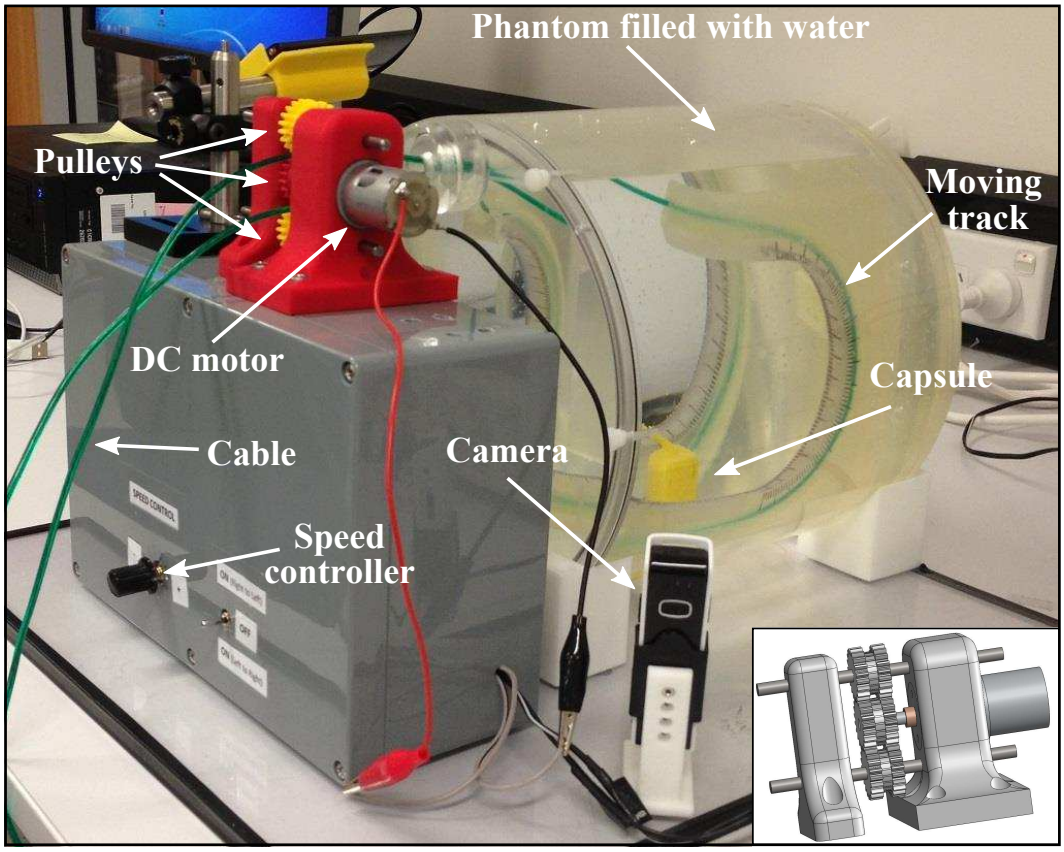

Figure 5.3: Overview of the experimental apparatus (the 3D design model of the drive system is shown at the right bottom of the figure)

By having the indicator and marks engraved on the track, the position of the capsule with respect to the track could be visually determined. Three small cameras were placed around the experimental apparatus to capture the movement of the capsule (Fig. 5.3) allowing the actual position coordinates and orientation of the capsule with respect to a reference coordinate system to be recorded during the experiments.

On the body of the track there was an insertable marker holder (Fig. 5.2C). This part was only inserted into the track at the beginning of the experiment for calibration which is explained in Section 5.3.

5.2.4 Phantom

A commercial Jaszczak Phantom (Fig. 5.3), which is widely used in PET studies, was employed in the experiments. The phantom was filled with water to simulate the photon attenuation of a human body. The cable was connected to the pulley system through a hole at the top of the phantom, placed horizontally. To fix the position of the track, it was attached to the bottom of the phantom by plastic screws.

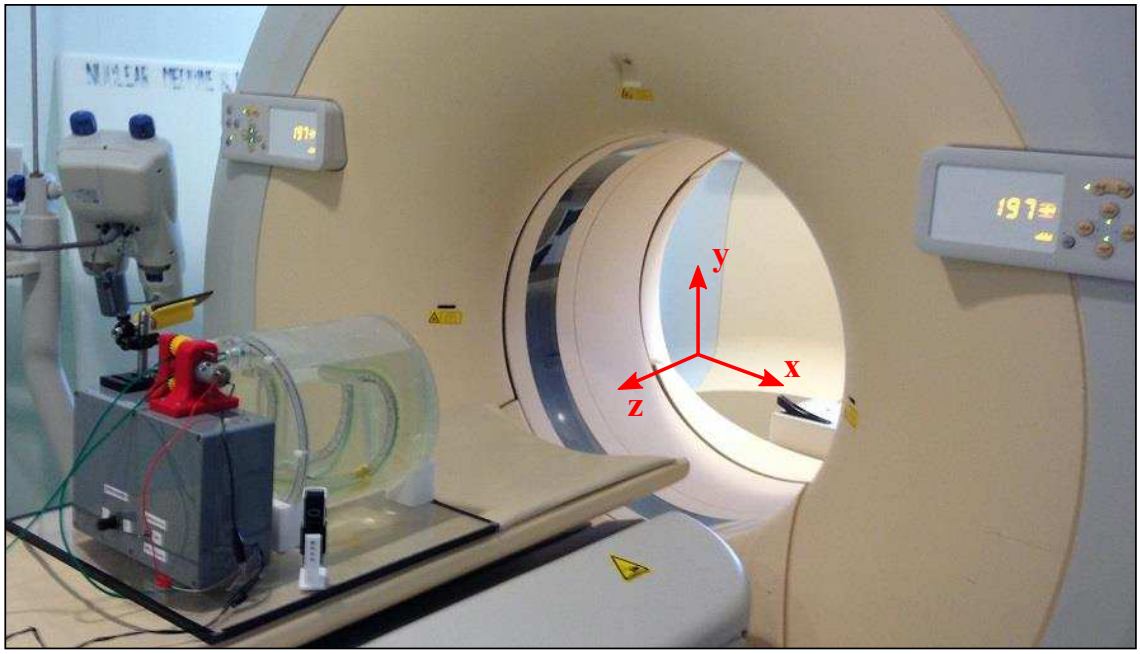

Figure 5.4: The experimental apparatus was placed on the patient bed of a Philips TF64 PET scanner before being moved to the centroid for scanning

5.3 Experimental procedure

Two sets of experiments were conducted on two different PET systems (a Philips Allegro/GEMINI PET system and a Philips TF64/GEMINI PET system) at the Austin Health Hospital, Melbourne, Australia. The experimental apparatus was placed on the patient bed (Fig. 5.4) and then moved to the centroid of the PET scanner. In each experiment, the apparatus was scanned with 5 different speeds of capsule movement (7.5, 12, 17, 21 and 27 mm/s). The capsule moved from one end to the other end of the track and returned before a new speed was set.

The input of the tracking algorithm is a list of Cartesian coordinates of two ends of coincidence lines. These data are dependent on the position and orientation of a reference coordinate system. For ease of calculation, we chose the centroid of the PET scanner as the origin of the reference coordinate system x,y,z axes of which are the lateral axis, vertical axis and longitudinal axis, respectively (as shown in Fig. 5.4).

In order to determine the actual position and orientation of the capsule with respect to the reference coordinate system, the local coordinate system of the track needs to be aligned with the reference coordinate system. This could be done by manually maneuvering the position of the patient bed with the aid of laser lights from the built-in alignment system. However, the centroid of the PET scanner could only be located roughly within a few millimeters of accuracy by the alignment system.

Therefore, an extra step (calibration step) was created before the main experiment started.

At the beginning of the calibration step, the marker holder (Fig. 5.2) was inserted into the track. One marker was then placed firmly on the holder. The actual position of the radioactive core of this marker was the origin of the local coordinate system of the track. A quick scan was performed so that the exact position of the marker could be determined. To ensure a high accuracy for this calibration step, the phantom was scanned without water to avoid scattered coincidences. It should be noted that the purpose of the calibration step was only to find the actual localization data of the capsule for later performance evaluation. For localization alone, it was unnecessary.

Once the calibration completed, the patient bed and the whole experimental apparatus were not allowed to move relatively in order to maintain the calibrated alignment between the two coordinate systems during the main experiment.

5.4 Processing experimental data

In the Philips PET system, there are several different acquisition modes. In order to extract the Cartesian coordinates of two ends of all coincidence lines, we used the Crystal Acquisition List Mode Format, in which the crystal row index and crystal number in the given row of the two crystals that have detected the coincidence gamma rays are stored. Based on the known geometry of the PET scanners, the list of pairs of index numbers were converted to a list of pairs of XYZ coordinates. The conversion process [117] is described as follows.

For each coincidence line, four indices are stored, which are (X_a, Z_a) and (X_b, Z_b). Where Z_a, Z_b are the row numbers and X_a, X_b are the crystal numbers in the given row Z_a, Z_b of the two crystals that have detected the coincidence gamma rays, respectively. Depending on the version of the Philips PET scanner, the full-ring scanner consists of n_{block} detector blocks, each with $n_{col} \times n_{row}$ crystals. Therefore, the scanner has n_{row} rows in the axial direction, and there are $(n_{block} \cdot n_{col})$ crystals in each row. Z_a, Z_b must be within 0 to $(n_{row} - 1)$, and X_a, X_b must be within 0 to $(n_{block} \cdot n_{col} - 1)$.

Obtained from the main header of the list-mode file, the crystal pitch in the axial direction is d_{pitch} (mm). Since we have chosen the origin of the coordinate system is

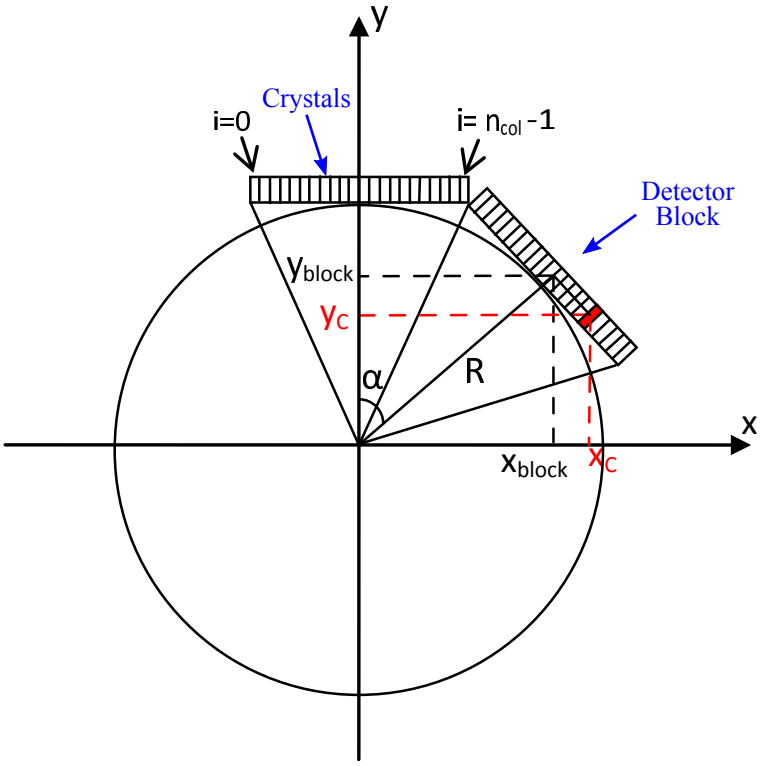

Figure 5.5: A sketch of a PET scanner for conversion of crystal indices to XYZ coordinates. The rectangle in solid red pattern is the crystal being converted

at the centroid of the scanner, the z-coordinate of a crystal (X_c, Z_c) is given by

$$z_c = d_{pitch}\Big(Z_c - (n_{row} - 1)/2\Big) \tag{5.1}$$

The angle between any two adjacent blocks seen from the centroid of the scanner is

$$\theta = 2\pi/n_{block} \tag{5.2}$$

The index of the block that contains the crystal is

$$i_{block} = (X_c \ \text{div} \ n_{col}) + 1 \tag{5.3}$$

The index of the crystal in $(i_{block})^{th}$ block is

$$i_{crystal} = X_c \ \text{mod} \ n_{col} \tag{5.4}$$

The angle between y-axis and the line connecting the origin of the coordinate system and the center of $(i_{block})^{th}$ block is

$$\alpha = (i_{block} - 1)\theta \tag{5.5}$$

Given the crystal depth d_{depth} (mm) and the radius of the scanner R (mm), the x

and y coordinates of the center of $(i_{block})^{th}$ block is

$$x_{block} = (R + d_{depth}/2)\sin\alpha \tag{5.6}$$

$$y_{block} = (R + d_{depth}/2)\cos\alpha \tag{5.7}$$

Given the crystal width d_{width}, distance from the crystal to the center of $(i_{block})^{th}$ block is

$$h = d_{width}\left(i_{crystal} - (n_{col} - 1)/2\right) \tag{5.8}$$

Therefore, the x and y coordinates of the crystal (Fig. 5.5) is

$$x_c = (R + d_{depth}/2)\sin\alpha + h\cos\alpha \tag{5.9}$$

$$y_c = (R + d_{depth}/2)\cos\alpha - h\sin\alpha \tag{5.10}$$

The values of R, n_{block}, n_{col}, n_{row}, d_{pitch}, d_{width}, and d_{depth} for each of the PET scanners can be looked up from Table 5.1.

Table 5.1: Specifications of Philips Allegro PET scanner and Philips TF64 PET scanner.

Variables	Definition	TF64 [118]	Allegro [106]
R	Radius of detector ring (mm)	451.7	432.05
n_{block}	Number of detector blocks	28	28
n_{col}	Number of crystal columns in a block	23	22
n_{row}	Number of crystal rows	44	29
d_{pitch}	Crystal pitch in axial direction (mm)	4 (+0.0750 gap)	6 (+0.3 gap)
d_{width}	Crystal width (mm)	4 (+0.0946 gap)	4 (+0.3 gap)
d_{depth}	Crystal depth (mm)	22	20

5.5 Results

After the data obtained from the PET systems had been converted, they were input into the tracking algorithm to evaluate the tracking performance. Matlab was used in both the conversion process and the implementation of the tracking algorithm. Approximately 16.63 million coincidence lines were recorded in the first experiment (8 minute scan by the TF64 scanner). In other words, there were on average 1,732 coincidence lines in each localization time interval (50 ms). Similar to the simulation study in Chapter 4, not all of the coincidence lines recorded in each run were used in

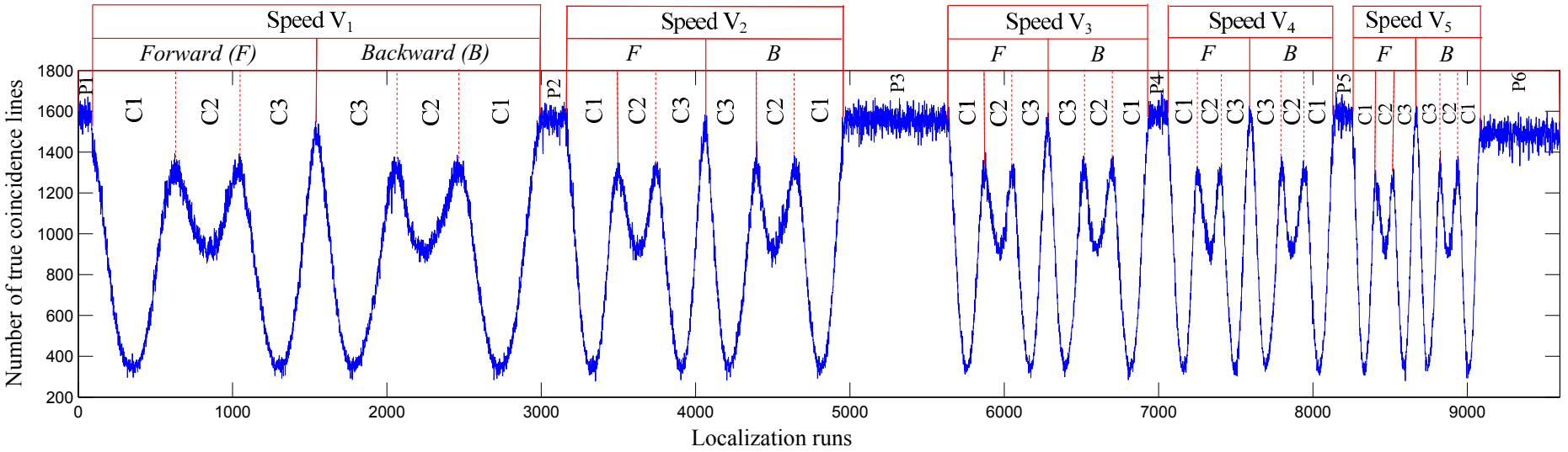

Figure 5.6: Number of true coincidence lines obtained in each localization run (50 ms) throughout 8-minute scanning by a TF64 PET scanner. V_1 (7.5 mm/s), V_2 (12 mm/s), V_3 (17 mm/s), V_4 (21 mm/s), and V_5 (27 mm/s) are five different capsule speeds tested in the experiment. In each speed, the capsule moved forward (F) from one end to the other end of the track and returned (backward-B) before its speed was changed. C1, C2 and C3 are the regions corresponding to three different curves of the track that the capsule passed as mentioned in Section 5.2.3. P1 to P6 are six intended pauses when the capsule stopped moving and its speed was set to the next level.

the tracking algorithm. To maintain a low computational time without significantly affecting the tracking accuracy, a fraction of them was sufficient.

Throughout a total of 9,600 localization runs, the capsule passed through the three different sections (C1, C2 and C3) of the track several times as illustrated in Fig. 5.6. The axial position of the capsule with respect to the PET scanner varied during its journey along the track. Surti *et al.* [118] have shown that the system sensitivity of a PET Gemini TF scanner drops off linearly with increasing axial separation from the scanner's centroid. Therefore, as expected, the number of true coincidence lines reduced linearly when the capsule moved axially from the scanner's centroid to the axial extremes. Figure 5.6 presents the number of true coincidence lines obtained in each localization run. As can be seen from the figure, the number of true coincidence lines recorded at the middle of the curves C1 and C3 were lowest. This is because these points were placed furthest away from the scanner's centroid in the experiments.

Because of this, a minor improvement has been made to the tracking algorithm. Instead of using a constant number of coincidence lines for every run as mentioned in the simulation study, a different number of coincidence lines is input to the tracking algorithm in each localization run. Depending on the sensitivity of the scanner at the previously estimated positions in the previous runs, the number of coincidence lines needed was calculated accordingly. This is because the axial positions of the capsule are assumed to be almost unchanged in two consecutive localization runs (50ms time difference). Regardless of the axial position of the capsule, this ensured that there were approximately 100 true coincidence lines per marker per run. In the first localization run, since the previous knowledge of the capsule's position is unknown, all recorded coincidence lines were used in the tracking algorithm. The estimate of initial values for the markers' position was thus more accurate.

Compared with the first experiment, only 11.02 million coincidence lines were recorded by the Allegro scanner in 8 minutes. This is understandable since TF64 is a newer PET scanner with higher resolution and detection efficiency (as shown in Table 5.1). Since the minimum acquisition time frame in an Allegro scanner is 100 ms, the length of a localization run for the second experiment was set at 100 ms. Therefore there were in total of 4,800 localization runs in the second experiment and an average of 2,296 coincidence lines recorded in each localization run.

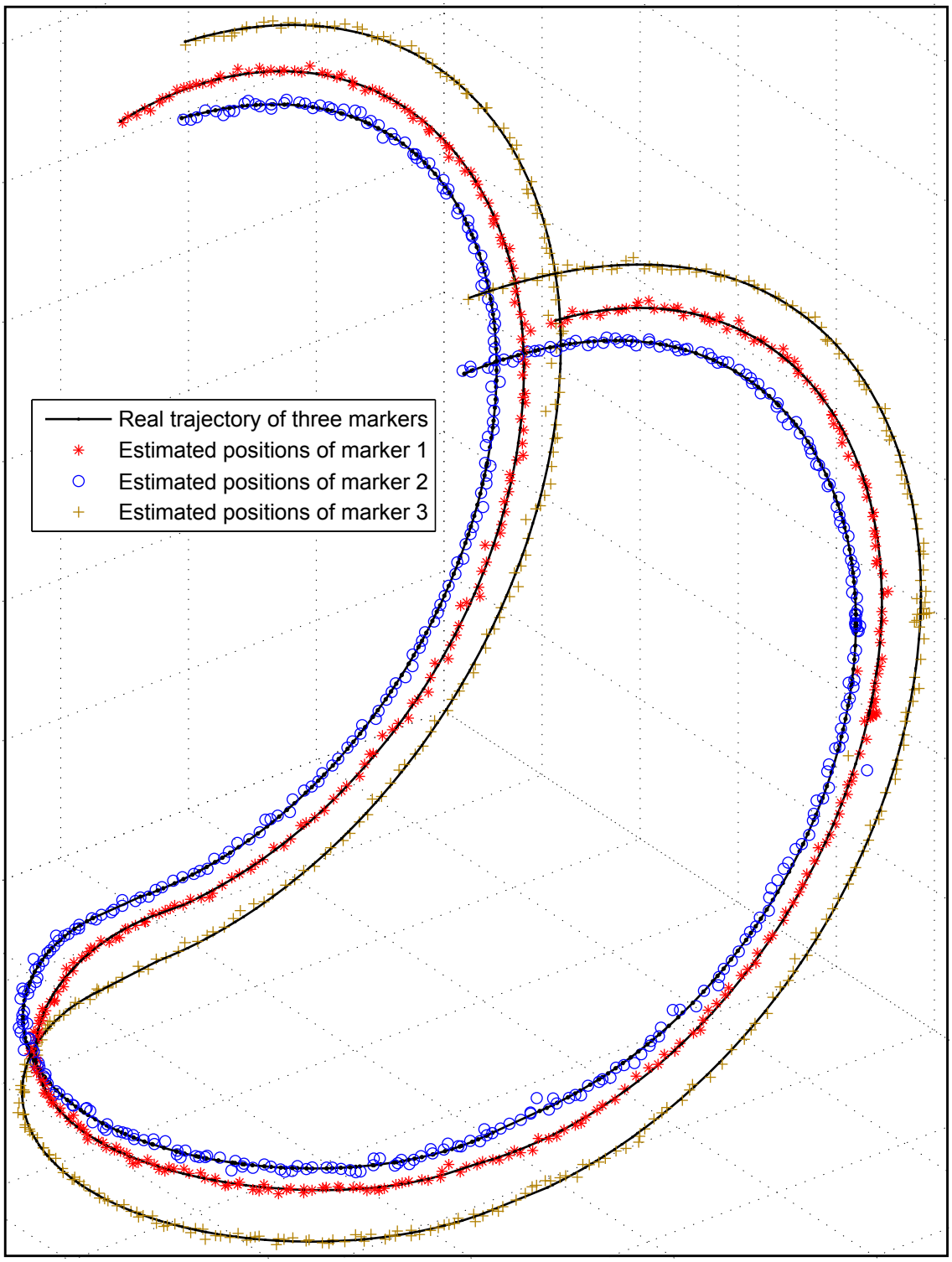

Figure 5.7: 3D trajectories of estimated positions and actual movement trajectories of the three markers on the same figure for comparison. These trajectories were plotted based on the data obtained when the capsule moved with the highest speed of 27 mm/s.

5.5.1 Position error of each marker

Over 9,600 localization runs (by the TF64 scanner), the tracking algorithm successfully located the three markers in 9,571 runs (99.7% success rate). The success

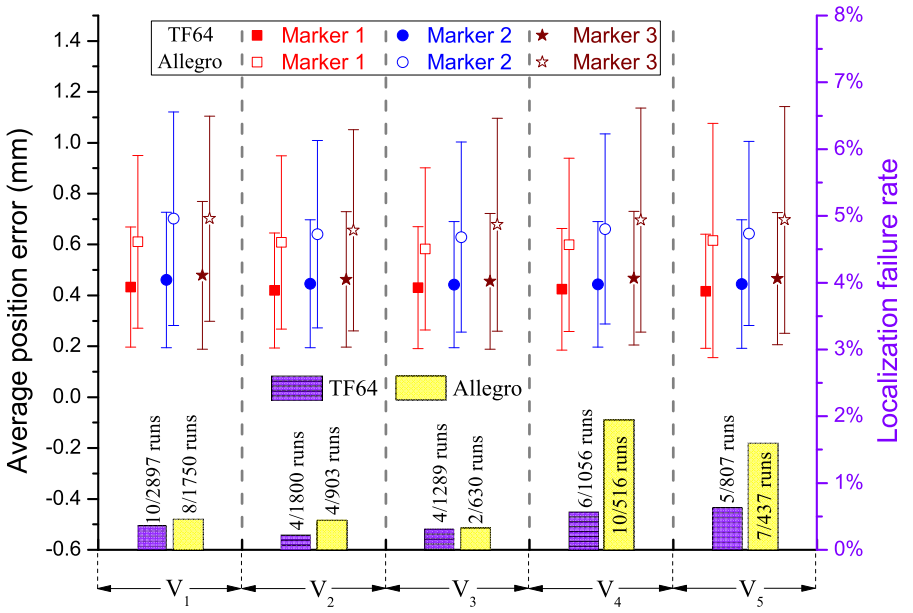

Figure 5.8: Top plot: Average position error (mean ± deviation) of each marker in different speed ranges of the capsule (V_1 to V_5). Bottom plot: Failure rates of the localization in different speed ranges of the capsule. Data obtained from both scanners (TF64 and Allegro) are presented for performance comparison.

rate in the second experiment (Allegro scanner) was 4,769/4,800 localization runs (99.35%). In both experiments, the localization failed at some runs because the input data collected in the runs were composed of only two clusters instead of three. This occurred only at some extreme locations in the axial field-of-view (FOV) of the PET scanner, which is explained in more detail in Section 5.6.

Figure 5.7 presents the 3D trajectories of estimated positions of the markers computed by the tracking algorithm, together with actual movement trajectories of the markers when the capsule moved with the highest speed of 27 mm/s. On average, the tracking algorithm took 6 ms to track the three markers in each localization run (computed by a 3.4 GHz Intel Core i7 processor).

The position errors of the three markers in each localization run can be evaluated by comparing the estimated positions computed by the tracking algorithm with the true positions recorded during the experiments. As demonstrated by the simulation study, the tracking algorithm is expected to achieve submillimeter accuracy. Therefore, the true positions of the markers need to be determined with a resolution of at least tens of micrometers every 50 ms. Although the true markers' positions could be obtained by visualization using the engraved marks and three cameras as described in Section 5.2.3, these data were not precise enough to be used as reference data in such a short time interval. However, the actual trajectory of the capsule movement is known based on the design of the track. The position errors can thus be computed by fitting estimated data to the designed trajectory of the track.

Figure 5.8 shows average position errors of the three markers in each speed range of the capsule movement for both two experimental data sets by TF64 and Allegro scanners. The localization failure rate in each speed range is also presented in the figure. Through observation, the localization is considered a failure when the relative activity of at least one marker drops below 0.01, or the relative distance between any two markers is less than 7 mm or larger than 16 mm. This is because the markers would not be classified correctly into their corresponding clusters if these values are reached. In this case, the tracking algorithm stops and proceeds to the next localization run. As shown in Fig. 5.8, the average position error of each marker falls between 0.4 mm to 0.5 mm when TF64 scanner is used, while the Allegro scanner provides approximately 0.6 mm to 0.7 mm average position error. Since the ^{22}Na marker that has highest activity (1.60 Mbq) was chosen as Marker 1 (Fig. 5.1), the average position error of this marker is always the smallest among the three markers as illustrated in Fig. 5.8.

5.5.2 Orientation error of the capsule

As explained in Chapter 4, a vector that originates from a midpoint between two closest markers to the furthest marker can be defined as the orientation vector of the capsule (Fig. 4.9). A different angle between an estimated orientation vector (found by three estimated positions of the markers) and a fitted orientation vector (based on three fitted positions of the markers on the actual trajectory) is considered the orientation error of the capsule. The average orientation error of the capsule for each movement speed range of the capsule is described in Table 5.2. As seen in the table, the average orientation error of the capsule was less than 2.4° when the TF64 scanner was used, and was less than 3.5° for data collected by the Allegro scanner.

Table 5.2: Average orientation error of the capsule in different speed levels of the capsule movement

Capsule speed	TF64 scanner	Allegro scanner
V_1 (7.5 mm/s)	$2.18° \pm 1.19°$	$3.26° \pm 1.77°$
V_2 (12 mm/s)	$2.22° \pm 1.21°$	$3.36° \pm 1.79°$
V_3 (17 mm/s)	$2.21° \pm 1.19°$	$3.35° \pm 1.75°$
V_4 (21 mm/s)	$2.31° \pm 1.21°$	$3.34° \pm 1.83°$
V_5 (27 mm/s)	$2.32° \pm 1.22°$	$3.46° \pm 1.92°$

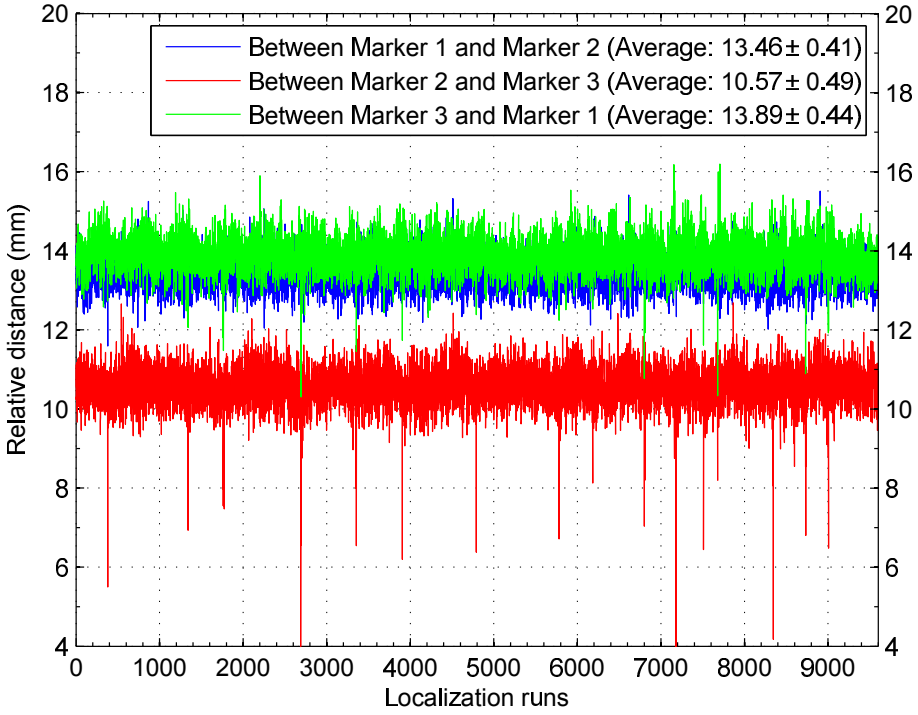

Figure 5.9: The relative distance between any two of the three estimated markers when TF64 scanner was used. The red points that fall below the majority of data points indicate the failed localization runs.

5.5.3 Relative distance error

Another important parameter in the evaluation of the tracking performance is the relative distance between any pairs of the three estimated markers. For 9600 localization runs (by the TF64 scanner), these data were calculated and plotted in Fig. 5.9. The figure shows that the average relative distances between the three markers for the entire data set were 10.57 ± 0.49 mm, 13.89 ± 0.44 mm and 13.46 ± 0.41 mm, respectively. Although the designed relative distances are 10 mm, 13 mm, 13 mm as mentioned in Section 3.3.1, due to manufacturing error the actual relative distances measured were a few hundred micrometers larger than the designed relative distances. Another source of error between the calculated relative distances and the designed distances is the position error of each marker. In the second experiment (by the Allegro scanner), over 4800 localization runs, the average relative distances were 10.96 ± 0.69 mm, 13.81 ± 0.68 mm and 13.72 ± 0.63 mm, respectively.

5.5.4 Precision of the tracking algorithm

During the experiment, there were several periods of time when the capsule remained stationary at one location, such as when the capsule completed the entire track and stopped before moving with a new speed, or at the end of the experiment when

Table 5.3: Precision of the tracking algorithm by evaluating the position change of each marker in the periods when the capsule remained stationary at one position

Scanners	Markers	Deviation in XYZ components			Distance to center
		X (mm)	Y (mm)	Z (mm)	of mass (mm)
TF64	Marker 1	0.29	0.30	0.22	0.44 ± 0.19
	Marker 2	0.32	0.32	0.25	0.47 ± 0.21
	Marker 3	0.30	0.27	0.24	0.43 ± 0.19
Allegro	Marker 1	0.43	0.45	0.30	0.62 ± 0.28
	Marker 2	0.53	0.52	0.44	0.78 ± 0.37
	Marker 3	0.48	0.45	0.40	0.69 ± 0.33

all the speeds had been tested (Fig. 5.6). Although different sets of gamma rays were generated in each localization run, the markers could still be located at almost the same location. In order to evaluate the precision of the tracking algorithm, the variation and deviation in the position change of each marker for the localization runs in which the capsule remained stationary were assessed.

The variation and deviation of a marker's position change over a period in which the marker remained stationary were calculated. This was based on the distance from the estimated position of the marker in each localization run to the center of mass of all the estimated positions of the marker for all the localization runs in this period. The average and standard deviation of these distances for both experiments are shown in Table 5.3. As seen from the table, these values are very close to the average position error mentioned in Section 5.5.1. In addition, the standard deviation of the position change in each of the XYZ components for each marker's estimated position is also included in Table 5.3.

5.6 Discussion

Although Fig. 5.8 shows that the average position error of each marker remains almost unchanged when the speed of the capsule movement varies from 7.5 mm/s to 27 mm/s, this does not mean that the movement speed of the capsule has no effect on the performance of the tracking algorithm. By increasing the movement speed, the position change of the capsule in one localization time interval is increased. This would result in a larger position error in the direction along the track. However as explained above the position error was calculated by taking residual errors after fitting estimated data into the known trajectory based on the experimental design. By doing this, the position error along the track was unintentionally omitted. Ex-

periments using a better method for determining the actual position of the capsule rather than visualization will be considered in a future work. Since the position error is expected to be less than 0.5 mm, the method needs to have a resolution of tens of μm in order to provide accurate reference data for calculating absolute position error.

Despite the above limitation, the experimental results in Fig. 5.8 have demonstrated a high robustness of the tracking algorithm. The tracking algorithm was able to locate the three markers when the capsule moved with a high speed of 27 mm/s. In conjunction with the evaluation of the relative distance and the evaluation of the precision explained above, the position error based on the residual error of fitting estimated data to actual movement trajectories is considered acceptable.

The high robustness of the tracking algorithm is also demonstrated through the capability of realizing failed localizations and getting back on track in the succeeding localization run. Over the entire experimental data set, the localization failed in several localization runs, but it successfully located the three markers in the subsequent runs. It should be noted that the failure was not caused by the algorithm itself, but it was due to the inadequate input data. As explained in Section 5.5, the number of true coincidence lines recorded at the middles of the curves C1 and C3 were lowest as these points were placed furthest away from the scanner's centroid in the experiments. When the capsule reached this location, due to the marker configuration in the capsule, Marker 3 which has lowest activity, was closer to the axial extremes of the PET scanner than the other two markers. This resulted in a significant difference in the number of true coincidence lines originated from Marker 3 and those arising from the other two markers. The input data of the tracking algorithm in this localization run was merely composed of two clusters of true coincidence lines. Therefore, it is understandable that the tracking algorithm was unable to extract the three markers from the given input data.

The limitation of the localization method at the locations that are too close to the axial extremes of the PET scanner can be overcome by moving the patient bed to ensure the current estimated positions of the capsule are always in the axial FOV of the scanner. The subsequent calculation can then be undertaken easily by adding the translation vector of the patient bed movement to the reference coordinate system.

The performance of the localization method was evaluated offline based on post-processed data. The tracking algorithm could not be implemented in real-time as soon as a sufficient number of coincidence lines were recorded in each localization time interval. This is understandable as the detector systems used in the experiments

were clinical PET scanners. The firmware of these systems is legally not able to be modified or updated. However, the average computational time of the tracking algorithm in each localization run is approximately 6 ms, much smaller than 50 ms sampling time. Therefore, the localization method has the potential to achieve real-time tracking when a custom detector system is built, instead of using clinical PET systems.

In this experimental study, the performance evaluation was performed using full-ring scanners. It would be ideal if the experiments were conducted in a smaller detector system similar to the system with two pairs of detector modules presented in the simulation study. Intentionally, a large number of coincidence lines recorded were not all used in the implementation of the tracking algorithm in order to make it similar to what is expected when a smaller detector system is used. Therefore, the activity of the marker in the future experiments with two pairs of detector modules is not expected to differ greatly from the activity level chosen in this study. The activity variation would mainly depend upon the patient's size.

Chapter 6

Algorithm Improvement

6.1 Introduction

The core part of the tracking algorithm developed and validated in the previous chapters is the clustering algorithm, by which a set of coincidence lines collected in each localization run is classified into three groups. The lines in the same group are assumed to originate from the same marker. However, the accuracy of the clustering is influenced by the balance in the number of coincidence lines between the three groups. The clustering is only accurate when the number of lines in the the three groups is not significantly different to each other. When one group has significantly less lines than the other two groups, it is likely that only two groups are recognized, resulting in two of the three markers being located at the same position. This is considered a tracking failure. As mentioned in Chapter 5, the imbalance in the number of lines occurs at some positions near the axial extreme of the FOV. In this chapter, an improved tracking algorithm is developed to reduce the tracking failure rate due to this imbalance, as well as to enhance the tracking accuracy.

The new tracking algorithm takes into account an important factor that has not been considered previously, which is the constant relative distance between any two of the three markers. As mentioned in the conceptual design of the PEcapsule in Section 3.3.1, the markers are fixed in the cover of the capsule which forms a rigid body (a triangle, as shown in Fig. 6.1). Regardless of the capsule's position and orientation, these relative distances remain unchanged. By considering this constraint, the failure cases in which two markers are estimated to be at the same position should not occur.

Although the objective of the tracking algorithm, which is to find the position of each marker, remains the same, the new tracking algorithm takes a different approach by

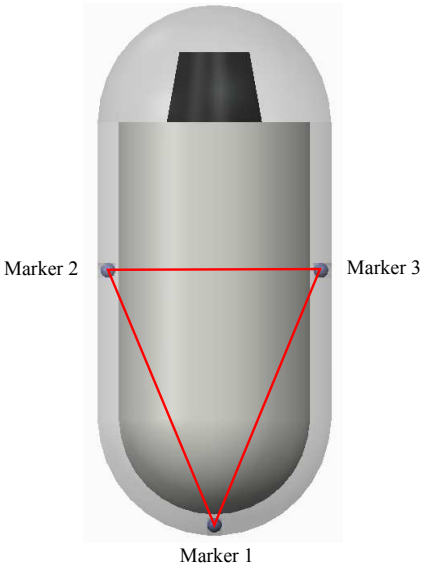

Figure 6.1: Three markers fixed on a capsule's cover form a rigid body (colored red).

exploiting the rigid-body constraint. In the previous algorithm, the marker's position is estimated by finding the point that is closest to all the lines in each classified group, i.e. each marker is the point that minimizes the sum of squared distances to all the lines in each group. The markers are thus treated as three independent objects. The required outputs are the values of nine variables (x_1, y_1, z_1), (x_2, y_2, z_2), (x_3, y_3, z_3), which are the Cartesian coordinates of the three markers, respectively. On the contrary, the new algorithm considers the three markers as a whole (one rigid object). The algorithm aims to best fit the triangle into the three groups of lines. In other words, it estimates the translation vector and rotation angles of the triangle such that the total sum of squared distances from its vertices to the corresponding lines is minimized, as shown in Fig. 6.2. The required outputs are thus the translation vector $\vec{t}(t_1, t_2, t_3)$ (i.e. the Cartesian coordinates of the triangle's centroid) and the rotation matrix (which is based on a rotation unit vector $\vec{r}(r_1, r_2, r_3)$ and a rotation angle θ). The vertices' positions (i.e. the markers' positions) can then be calculated from the estimated translation and rotation parameters of the triangle. By including the rigid-body constraint, the number of output variables has been decreased from nine to seven.

The new tracking algorithm reduces the tracking failure rate and enhances the tracking accuracy, and is described in more detail in the remainder of this chapter. In addition, a brief introduction about the classic rigid-body transformation is presented in Section 6.2, followed by a detailed explanation of how the tracking algorithm estimates the translation and rotation information of a rigid-body, in Section 6.3. The tracking performance of the algorithm is evaluated using both simulation data and experimental data, in Section 6.4.

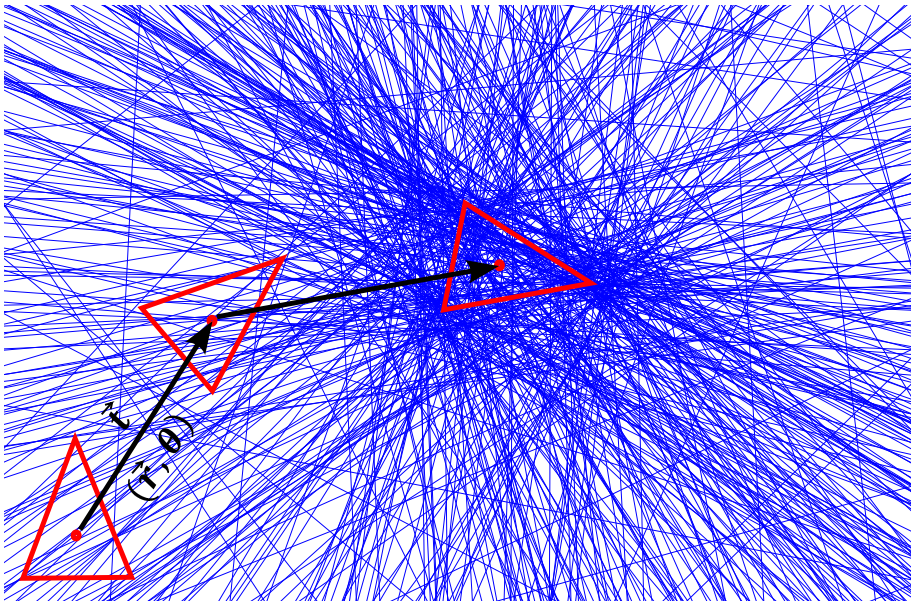

Figure 6.2: A simple diagram showing the principle of the tracking algorithm based on rigid-body transformation. Starting from an initial position, the triangle is iteratively transformed to a new estimated position and orientation until it best fits into the three groups of lines in 3D space. The transformation parameters are a translation vector $\vec{t}(t_1, t_2, t_3)$, a rotation unit vector $\vec{r}(r_1, r_2, r_3)$, and a rotation angle θ.

6.2 Rigid-body transformation

Finding the optimal rigid-body transformation (combination of rotation and translation) between two sets of corresponding 3D points has been a common problem in many applications such as robotics, computer vision, pattern recognition, bioinformatics, and so on. A rigid-body transformation is defined as that transformation enabling the distance between any two points of the transformed dataset to remain the same as in the original datatset. In the past, many algorithms have been developed to determine the transformation parameters to map, align or register one point set to the other. In general, the algorithm aims to minimize the sum of all the squared pairwise distances between the two datasets. The proposed solutions include closed-form solutions (such as using singular value decomposition (SVD) [119], exploiting the orthonormal properties of the rotation matrix [120], using unit quaternions [121]), and iterative estimation methods [122, 123].

Although many solutions for the estimation of rigid-body transformation between 3D point sets are already available, to the best of the author's knowledge, a solution to determine the transformation parameters to register a rigid body to groups of lines in 3D space has not yet been investigated. The latter is expected to be more complex than the former because of the following reasons. In 3D space, each line consists of 6 independent variables while the number of independent variables in a 3D point is only 3. A solution for the matching problem between points and lines would

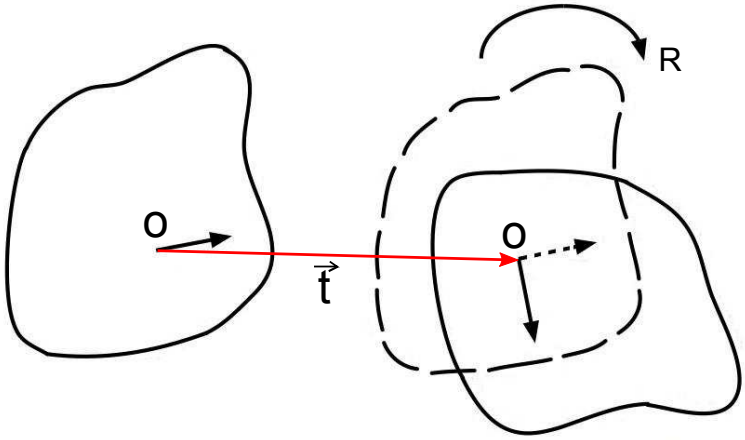

Figure 6.3: An example of rigid-body transformation. The left object is transformed to the right one.

have to deal with more independent variables. In general, for matching/registering type problems, the objective function that needs to be minimized is a function of squared distances between pairs of objects. In addition, the formula of the distance between a point and a line in 3D (which involves cross product) is much more complex than that of the distance between two points. Therefore, the minimization of the objective function becomes more difficult. This makes the matching problem with points and lines an interesting challenge to deal with. In the next section, an iterative method is developed to solve this problem.

6.3 Improved tracking algorithm based on rigid-body transformation

In this section, a new tracking algorithm based on rigid-body transformation is developed to determine the markers' positions. The algorithm iteratively estimates the transformation parameters (i.e. the translation vector and the rotation matrix) of a triangular rigid-body with sides of 10 mm, 13 mm, 13 mm until the rigid-body is best fitted into the three groups of lines. The final estimated transformation parameters are the ones that provide the minimized total sum of squared distances from the three vertices of the triangle to their corresponding lines. The final positions of the triangle's vertices are adopted to be the markers' positions.

6.3.1 Mathematical form of the problem

The problem can be summarized in a mathematical form as follows:

INPUT: The inputs of the tracking algorithm are

- Three vertices $\vec{P}_j$ $(j = 1, .., 3)$ of the triangle with sides of 13 mm, 13 mm, 10 mm at an initial stage. The triangle is initialized to be at the origin of the Cartesian coordinate system (i.e. the centroid of the detector system) and lie on the XY plane. Therefore, the initial values of $\vec{P}_1$, $\vec{P}_2$, and $\vec{P}_3$ can be set as below
$$\vec{P}_1 = [\text{-}5,\ \text{-}4,\ 0]^T\,;\quad \vec{P}_2 = [0,\ 8,\ 0]^T\,;\quad \vec{P}_3 = [5,\ \text{-}4,\ 0]^T \tag{6.1}$$
- N coincidence lines ℓ_i $(i = 1, .., N)$ with unit vectors $\vec{n}_i = [n_{ix}, n_{iy}, n_{iz}]^T$ $\big(\text{where } n_{ix}^2 + n_{iy}^2 + n_{iz}^2 = 1\big)$ and passing through points $\vec{a}_i = [a_{ix}, a_{iy}, a_{iz}]^T$.
- Degree of membership u_{ij} of each coincidence line ℓ_i to each vertex $\vec{P}_j$. The value of u_{ij} is obtained from the Fuzzy C-means clustering algorithm in Eq. (3.15).

OBJECTIVE FUNCTION: Starting from the initial stage, the algorithm iteratively rotates and translates the triangle which creates a new set of vertices:

$$\vec{M}_j = \Omega\vec{P}_j + \vec{t} \tag{6.2}$$

where Ω is a 3×3 matrix that represents the rotation and $\vec{t} = [t_x, t_y, t_z]^T$ is the translation vector. According to Rodrigue's rotation formula [124], any rotation matrix can be converted to a rotation around an arbitrary axis with a unit vector $\vec{r} = [r_x, r_y, r_z]$ (i.e. $r_x^2 + r_y^2 + r_z^2 = 1$) passing through the body's centroid at an angle θ. The formula of Ω is given by

$$\Omega = I\ \cos\theta + \sin\theta\,[\vec{r}]_\times + (1 - \cos\theta)\vec{r}\ \vec{r}^T \tag{6.3}$$

where I is a 3×3 identity matrix and $[\vec{r}]_\times$ is a skew-symmetric matrix defined by

$$[\vec{r}_j]_\times = \begin{bmatrix} 0 & -r_z & r_y \\ r_z & 0 & -r_x \\ -r_y & r_x & 0 \end{bmatrix} \tag{6.4}$$

As explained above, the objective of the algorithm is to find the optimal transformation parameters of the triangle to minimize the total sum of the squared perpendicular distances from each vertex to its corresponding lines. Therefore, the **objective function** is the total sum of squared distances, given by

$$f(\Omega, \vec{t}) = \sum_{j=1}^{3}\sum_{i=1}^{N} u_{ij}^q \left\|\vec{d}_{ij}\right\|^2 \tag{6.5}$$

where q is a weighting exponent which controls the fuzziness of the clusters as mentioned in Chapter 3, and $\vec{d}_{ij}$ is a distance vector from a vertex $\vec{M}_j$ to a coincidence line ℓ_i.

OUTPUT: The required outputs of the algorithm are the values of $\vec{r}$, θ, and $\vec{t}$. Using these data, the markers' positions can be easily obtained from (6.2).

6.3.2 Solution

In order to minimize the objective function $f(\Omega, \vec{t})$, the function needs to be derived and simplified so that its gradient can be obtained. This is described in detail as follows:

The distance vector from a vertex $\vec{M}_j$ to a coincidence line ℓ_i is

$$\vec{d}_{ij} = \left(\vec{a}_i - \vec{M}_j\right) - \left(\left(\vec{a}_i - \vec{M}_j\right) \cdot \vec{n}_i\right) \vec{n}_i \tag{6.6}$$

$$= \left(\vec{a}_i - \vec{M}_j\right) - \vec{n}_i^T \left(\vec{a}_i - \vec{M}_j\right) \vec{n}_i \tag{6.7}$$

$$= \left(\vec{a}_i - \vec{M}_j\right) - \vec{n}_i \, \vec{n}_i^T \left(\vec{a}_i - \vec{M}_j\right) \quad \left[\text{since } \vec{n}_i^T \left(\vec{a}_i - \vec{M}_j\right) \text{ is a number}\right] \tag{6.8}$$

$$= \left(I - \vec{n}_i \, \vec{n}_i^T\right) \left(\vec{a}_i - \vec{M}_j\right) \tag{6.9}$$

$$= \left[\vec{n}_i\right]_\times^2 \left(\vec{a}_i - \vec{M}_j\right) \tag{6.10}$$

$$= \left[\vec{n}_i\right]_\times^2 \vec{a}_i - \left[\vec{n}_i\right]_\times^2 \vec{M}_j \tag{6.11}$$

Therefore, the squared distance from a vertex $\vec{M}_j$ to a coincidence line ℓ_i is

$$\left\|\vec{d}_{ij}\right\|^2 = \vec{d}_{ij}^T \, \vec{d}_{ij} \tag{6.12}$$

$$= \left(\left[\vec{n}_i\right]_\times^2 \vec{a}_i - \left[\vec{n}_i\right]_\times^2 \vec{M}_j\right)^T \left(\left[\vec{n}_i\right]_\times^2 \vec{a}_i - \left[\vec{n}_i\right]_\times^2 \vec{M}_j\right) \tag{6.13}$$

$$= \left(\vec{a}_i^T \left[\vec{n}_i\right]_\times^2 - \vec{M}_j^T \left[\vec{n}_i\right]_\times^2\right) \left(\left[\vec{n}_i\right]_\times^2 \vec{a}_i - \left[\vec{n}_i\right]_\times^2 \vec{M}_j\right) \quad \left[\text{since } \left[\vec{n}_i\right]_\times^2 \text{ is symmetric}\right] \tag{6.14}$$

$$= \vec{a}_i^T \left[\vec{n}_i\right]_\times^2 \left[\vec{n}_i\right]_\times^2 \vec{a}_i - \vec{a}_i^T \left[\vec{n}_i\right]_\times^2 \left[\vec{n}_i\right]_\times^2 \vec{M}_j - \vec{M}_j^T \left[\vec{n}_i\right]_\times^2 \left[\vec{n}_i\right]_\times^2 \vec{a}_i + \vec{M}_j^T \left[\vec{n}_i\right]_\times^2 \left[\vec{n}_i\right]_\times^2 \vec{M}_j \tag{6.15}$$

Since $\left[\vec{n}_i\right]_\times^2 \left[\vec{n}_i\right]_\times^2 = -\left[\vec{n}_i\right]_\times^2$, we have

$$\left\|\vec{d}_{ij}\right\|^2 = -\vec{a}_i^T \left[\vec{n}_i\right]_\times^2 \vec{a}_i + \vec{a}_i^T \left[\vec{n}_i\right]_\times^2 \vec{M}_j + \vec{M}_j^T \left[\vec{n}_i\right]_\times^2 \vec{a}_i - \vec{M}_j^T \left[\vec{n}_i\right]_\times^2 \vec{M}_j \tag{6.16}$$

Moreover, $\vec{a}_i^T \left[\vec{n}_i\right]_\times^2 \vec{M}_j = \vec{a}_i^T \vec{M}_j - \vec{a}_i^T \vec{n}_i \vec{n}_i^T \vec{M}_j = \vec{M}_j^T \vec{a}_i - \vec{M}_j^T \vec{n}_i \vec{n}_i^T \vec{a}_i = \vec{M}_j^T \left[\vec{n}_i\right]_\times^2 \vec{a}_i$,

thus

$$\left\|\vec{d}_{ij}\right\|^2 = -\vec{a}_i^T \left[\vec{n}_i\right]_\times^2 \vec{a}_i + 2\vec{a}_i^T \left[\vec{n}_i\right]_\times^2 \vec{M}_j - \vec{M}_j^T \left[\vec{n}_i\right]_\times^2 \vec{M}_j \tag{6.17}$$

Substituting (6.17) into (6.5), we have

$$f(\Omega, \vec{t}) = \sum_{j=1}^{3}\sum_{i=1}^{N} u_{ij}^q \left(-\vec{a}_i^T \left[\vec{n}_i\right]_\times^2 \vec{a}_i + 2\vec{a}_i^T \left[\vec{n}_i\right]_\times^2 \vec{M}_j - \vec{M}_j^T \left[\vec{n}_i\right]_\times^2 \vec{M}_j\right) \tag{6.18}$$

$$= \sum_{j=1}^{3}\sum_{i=1}^{N} \left(-u_{ij}^q \vec{a}_i^T \left[\vec{n}_i\right]_\times^2 \vec{a}_i + 2u_{ij}^q \vec{a}_i^T \left[\vec{n}_i\right]_\times^2 \vec{M}_j - \vec{M}_j^T u_{ij}^q \left[\vec{n}_i\right]_\times^2 \vec{M}_j\right) \tag{6.19}$$

$$= \sum_{j=1}^{3} \left(\sum_{i=1}^{N} -u_{ij}^q \vec{a}_i^T \left[\vec{n}_i\right]_\times^2 \vec{a}_i + \left(\sum_{i=1}^{N} 2u_{ij}^q \vec{a}_i^T \left[\vec{n}_i\right]_\times^2\right)\vec{M}_j - \vec{M}_j^T \left(\sum_{i=1}^{N} u_{ij}^q \left[\vec{n}_i\right]_\times^2\right)\vec{M}_j\right) \tag{6.20}$$

$$= \sum_{j=1}^{3} \left(c_j + \vec{V}_j^T \vec{M}_j - \vec{M}_j^T A_j \vec{M}_j\right) \tag{6.21}$$

where

$$c_j = \sum_{i=1}^{N} -u_{ij}^q \vec{a}_i^T \left[\vec{n}_i\right]_\times^2 \vec{a}_i \tag{6.22}$$

$$\vec{V}_j^T = \sum_{i=1}^{N} 2u_{ij}^q \vec{a}_i^T \left[\vec{n}_i\right]_\times^2 \tag{6.23}$$

$$A_j = \sum_{i=1}^{N} u_{ij}^q \left[\vec{n}_i\right]_\times^2 = \begin{bmatrix} \sum_{i=1}^{N} u_{ij}^q (n_{ix}^2 - 1) & \sum_{i=1}^{N} u_{ij}^q (n_{ix}n_{iy}) & \sum_{i=1}^{N} u_{ij}^q (n_{ix}n_{iz}) \\ \sum_{i=1}^{N} u_{ij}^q (n_{ix}n_{iy}) & \sum_{i=1}^{N} u_{ij}^q (n_{iy}^2 - 1) & \sum_{i=1}^{N} u_{ij}^q (n_{iy}n_{iz}) \\ \sum_{i=1}^{N} u_{ij}^q (n_{ix}n_{iz}) & \sum_{i=1}^{N} u_{ij}^q (n_{iy}n_{iz}) & \sum_{i=1}^{N} u_{ij}^q (n_{iz}^2 - 1) \end{bmatrix} \tag{6.24}$$

To minimize the objective function with respect to the translation vector $\vec{t}$, the objective function is first differentiated with respect to $\vec{t}$ to satisfy the following equation

$$\frac{\partial f(\Omega, \vec{t})}{\partial \vec{t}} = \vec{0} \tag{6.25}$$

Substituting (6.2) and (6.21) to (6.25), we have

$$\frac{\partial \sum_{j=1}^{3} \left(c_j + \vec{V}_j^T \left(\Omega\vec{P}_j + \vec{t}\right) - \left(\Omega\vec{P}_j + \vec{t}\right)^T A_j \left(\Omega\vec{P}_j + \vec{t}\right)\right)}{\partial \vec{t}} = \vec{0}^T \tag{6.26}$$

$$\sum_{j=1}^{3} \left(\vec{V}_j^T - 2\left(\Omega\vec{P}_j + \vec{t}\right)^T A_j\right) = \vec{0}^T \tag{6.27}$$

$$\sum_{j=1}^{3} \vec{V}_j^T - 2\sum_{j=1}^{3} \left(\Omega \vec{P}_j\right)^T A_j - 2\vec{t}^T \sum_{j=1}^{3} A_j = \vec{0}^T \tag{6.28}$$

$$2\vec{t}^T \sum_{j=1}^{3} A_j = -2\sum_{j=1}^{3} \left(\Omega \vec{P}_j\right)^T A_j + \sum_{j=1}^{3} \vec{V}_j^T \tag{6.29}$$

$$\left(\sum_{j=1}^{3} A_j\right) \vec{t} = -\sum_{j=1}^{3} \left(A_j \Omega \vec{P}_j\right) + \frac{1}{2}\sum_{j=1}^{3} \vec{V}_j \quad \text{[since } A_j \text{ is symmetric]} \tag{6.30}$$

Therefore,

$$\vec{t} = -\sum_{j=1}^{3} \left(A^{-1} A_j \Omega \vec{P}_j\right) + A^{-1}\vec{A}_4 = -\sum_{j=1}^{3} \left(B_j \Omega \vec{P}_j\right) + \vec{B}_4 \tag{6.31}$$

$$\text{where } A = A_1 + A_2 + A_3 \tag{6.32}$$

$$\vec{A}_4 = \frac{1}{2}\sum_{j=1}^{3} \vec{V}_j = \sum_{j=1}^{3}\sum_{i=1}^{N} \left(u_{ij}^q \left(\left(\vec{a}_i \cdot \vec{n}_i\right)\vec{n}_i - \vec{a}_i\right)\right) \tag{6.33}$$

$$B_j = A^{-1} A_j \quad (j = 1, \ldots, 4) \tag{6.34}$$

Substituting (6.3) into (6.31), the translation vector is given by

$$\vec{t} = -\cos\theta \sum_{j=1}^{3} B_j \vec{P}_j - \sin\theta \sum_{j=1}^{3} B_j \left[\vec{r}\right]_\times \vec{P}_j - (1-\cos\theta)\sum_{j=1}^{3} \left(B_j \vec{r}\, \vec{r}^T \vec{P}_j\right) + \vec{B}_4 \tag{6.35}$$

Since $\left[\vec{r}\right]_\times \vec{P}_j = \left[\vec{P}_j\right]_\times^T \vec{r}$ and $(\vec{r}^T \vec{P}_j)$ is a number, thus

$$\vec{t} = -\cos\theta \sum_{j=1}^{3} B_j \vec{P}_j - \sin\theta \left(\sum_{j=1}^{3} B_j \left[\vec{P}_j\right]_\times^T\right)\vec{r} - (1-\cos\theta)\left(\sum_{j=1}^{3} \vec{r}^T \vec{P}_j B_j\right)\vec{r} + \vec{B}_4 \tag{6.36}$$

Substituting (6.3) and (6.36) into (6.2), the new vertices $\vec{M}_j$ are given by

$$\begin{aligned} \vec{M}_j = &-\cos\theta \left(\sum_{k=1}^{3} B_k \vec{P}_k - \vec{P}_j\right) - \sin\theta \left(\left(\sum_{k=1}^{3} B_k \left[\vec{P}_k\right]_\times^T\right) - \left[\vec{P}_j\right]_\times^T\right)\vec{r} - \ldots \\ &- (1-\cos\theta)\left(\left(\sum_{k=1}^{3} \vec{r}^T \vec{P}_k B_k\right) - \vec{r}^T \vec{P}_j I\right)\vec{r} + \vec{B}_4 \end{aligned} \tag{6.37}$$

$$\vec{M}_j = -(\cos\theta)\vec{E}_j - (\sin\theta) H_j \vec{r} - (1-\cos\theta)\left(\left(\sum_{k=1}^{3} \vec{r}^T \vec{P}_k B_k\right) - \vec{r}^T \vec{P}_j I\right)\vec{r} + \vec{B}_4 \tag{6.38}$$

$$\text{where } \vec{E}_j = \sum_{k=1}^{3} B_k \vec{P}_k - \vec{P}_j \tag{6.39}$$

$$H_j = \Big(\sum_{k=1}^{3} B_k \left[\vec{P}_k\right]_\times^T\Big) - \left[\vec{P}_j\right]_\times^T \tag{6.40}$$

Substituting (6.38) into (6.21), the objective function is simplified as below

$$\begin{aligned} f(\Omega,\vec{t}) = &\Big(s_1 - s_2\cos\theta - s_3(\cos\theta)^2\Big) + \Big(-(\sin\theta)\,\vec{K}_1^T - (\cos\theta\sin\theta)\,\vec{K}_2^T\Big)\vec{r} + \dots \\ &+ \vec{r}^T\Big(-(1-\cos\theta)\,R_1 - (1-\cos\theta)(\cos\theta)\,R_2 - (\sin\theta)^2\,R_3\Big)\vec{r} + \dots \\ &- 2(1-\cos\theta)(\sin\theta)\,\vec{r}^T\sum_{k=1}^{3}\Bigg(\vec{r}^T\vec{P}_k\Big(\Big(\sum_{j=1}^{3}H_j^T A_j\Big)B_k - H_k^T A_k\Big)\Bigg)\vec{r} + \dots \\ &- (1-\cos\theta)^2\,\vec{r}^T\Bigg(\sum_{j=1}^{3}\sum_{k=1}^{3}\vec{r}^T\vec{P}_j\left(B_j^T A\,B_k - B_j^T A_k - A_j B_k\right)\vec{P}_k^T\vec{r} + \sum_{j=1}^{3}\vec{r}^T\vec{P}_j A_j\vec{P}_j^T\vec{r}\Bigg)\vec{r} \end{aligned} \tag{6.41}$$

where $$s_1 = \sum_{j=1}^{3}\Big(c_j + \vec{V}_j^T\vec{B}_4 - \vec{B}_4^T A_j\vec{B}_4\Big) \tag{6.42}$$

$$s_2 = \sum_{j=1}^{3}\Big(\vec{V}_j^T\vec{E}_j - 2\vec{B}_4^T A_j\vec{E}_j\Big) \tag{6.43}$$

$$s_3 = \sum_{j=1}^{3}\vec{E}_j^T A_j\vec{E}_j \tag{6.44}$$

$$\vec{K}_1^T = \sum_{j=1}^{3}\Big(\vec{V}_j^T H_j - 2\vec{B}_4^T A_j H_j\Big) \tag{6.45}$$

$$\vec{K}_2^T = \sum_{j=1}^{3}\Big(2\vec{E}_j^T A_j H_j\Big) \tag{6.46}$$

$$R_1 = \sum_{j=1}^{3}\Bigg(\sum_{k=1}^{3}\vec{P}_k\vec{V}_j^T B_k - \vec{P}_j\vec{V}_j^T - 2\Big(\sum_{k=1}^{3}\vec{P}_k\vec{B}_4^T A_j B_k - \vec{P}_j\vec{B}_4^T A_j\Big)\Bigg) \tag{6.47}$$

$$R_2 = 2\sum_{j=1}^{3}\Bigg(\sum_{k=1}^{3}\vec{P}_k\vec{E}_j^T A_j B_k - \vec{P}_j\vec{E}_j^T A_j\Bigg) \tag{6.48}$$

$$R_3 = \sum_{j=1}^{3}H_j^T A_j H_j \tag{6.49}$$

The gradient of the objective function can thus be given by

$$\begin{aligned} \nabla_{\vec{r}} f = &\Big(-(\sin\theta)\,\vec{K}_1^T - 0.5(\sin 2\theta)\,\vec{K}_2^T\Big) + \dots \\ &+ \vec{r}^T\Big(-(1-\cos\theta)\left(R_1 + R_1^T\right) - (1-\cos\theta)(\cos\theta)\left(R_2 + R_2^T\right) - (\sin\theta)^2\left(R_3 + R_3^T\right)\Big) + \dots \\ &+ (\sin 2\theta - 2\sin\theta)\,\vec{r}^T\sum_{k=1}^{3}\Bigg(\vec{r}^T\vec{P}_k\Big(\Big(\sum_{j=1}^{3}H_j^T A_j\Big)B_k + B_k^T\sum_{j=1}^{3}A_j^T H_j - H_k^T A_k - A_k^T H_k\Big) + \dots \end{aligned}$$

$$+\left(\left(\sum_{j=1}^{3} H_j^T A_j\right) B_k - H_k^T A_k\right)\vec{r}\vec{P}_k^T\Bigg) + \ldots$$

$$-(1-\cos\theta)^2\,\vec{r}^T\Bigg(\sum_{j=1}^{3}\sum_{k=1}^{3}\vec{r}^T\vec{P}_j\left(B_j^T A\,B_k + B_k^T A\,B_j - B_j^T A_k - A_k B_j - A_j B_k - B_k^T A_j\right)\vec{P}_k^T\vec{r} + \ldots$$

$$+\sum_{j=1}^{3}\sum_{k=1}^{3}\left(B_j^T A\,B_k - B_j^T A_k - A_j B_k\right)\vec{r}\left(\vec{P}_j^T\vec{r}\vec{P}_k^T + \vec{P}_k^T\vec{r}\vec{P}_j^T\right) + \ldots$$

$$+2\sum_{j=1}^{3}\vec{r}^T\vec{P}_j A_j\vec{P}_j^T\vec{r} + 2\sum_{j=1}^{3} A_j\vec{r}\vec{P}_j^T\vec{r}\vec{P}_j^T\Bigg) \tag{6.50}$$

$$\nabla_\theta f = \left(s_2\sin\theta + s_3\left(\sin 2\theta\right)\right) + \left(-\left(\cos\theta\right)\vec{K}_1^T - \left(\cos 2\theta\right)\vec{K}_2^T\right)\vec{r} + \ldots$$

$$+\,\vec{r}^T\left(-\left(\sin\theta\right)R_1 + \left(\sin\theta - \sin 2\theta\right)R_2 - \left(\sin 2\theta\right)R_3\right)\vec{r} + \ldots$$

$$+\,2\left(\cos 2\theta - \cos\theta\right)\vec{r}^T\sum_{k=1}^{3}\left(\vec{r}^T\vec{P}_k\left(\left(\sum_{j=1}^{3} H_j^T A_j\right)B_k - H_k^T A_k\right)\right)\vec{r} + \ldots$$

$$+\left(\sin 2\theta - 2\sin\theta\right)\vec{r}^T\Bigg(\sum_{j=1}^{3}\sum_{k=1}^{3}\vec{r}^T\vec{P}_j\left(B_j^T A\,B_k - B_j^T A_k - A_j B_k\right)\vec{P}_k^T\vec{r} + \ldots$$

$$+\sum_{j=1}^{3}\vec{r}^T\vec{P}_j A_j\vec{P}_j^T\vec{r}\Bigg)\vec{r} \tag{6.51}$$

Since the objective function f and its gradients ($\nabla_\theta f$ and $\nabla_{\vec{r}} f$) are functions of four variables (r_x, r_y, r_z, θ) with a constraint $r_x^2 + r_y^2 + r_z^2 = 1$, finding the minimum of the objective function can be achieved by using the built-in Matlab function "*fmincon*", a constrained nonlinear optimization function.

6.4 Performance evaluation of the new tracking algorithm

Based on the above equations, the new tracking algorithm was programmed in Matlab. The same simulation data using the XCAT voxelized phantom (in Chapter 4) and the same experimental data (in Chapter 5) were imported into Matlab to evaluate the performance of the new tracking algorithm.

Table 6.1: A comparison between the previous algorithm and the new algorithm based on rigid-body transformation in terms of position error of the markers. Experimental data obtained from the **Allegro** scanner were used for the comparison.

Speeds	Algorithms	Position error (mean±std) in mm		
		Marker 1	Marker 2	Marker 3
V_1 (7.5 mm/s)	No rigid constraint	0.61 ± 0.34	0.70 ± 0.42	0.70 ± 0.40
	With rigid constraint	0.59 ± 0.33	0.57 ± 0.32	0.62 ± 0.46
V_2 (12 mm/s)	No rigid constraint	0.61 ± 0.34	0.64 ± 0.37	0.66 ± 0.40
	With rigid constraint	0.55 ± 0.34	0.57 ± 0.33	0.56 ± 0.34
V_3 (17 mm/s)	No rigid constraint	0.58 ± 0.32	0.63 ± 0.37	0.68 ± 0.42
	With rigid constraint	0.55 ± 0.31	0.56 ± 0.32	0.55 ± 0.31
V_4 (21 mm/s)	No rigid constraint	0.60 ± 0.34	0.66 ± 0.37	0.70 ± 0.44
	With rigid constraint	0.56 ± 0.32	0.57 ± 0.33	0.54 ± 0.32
V_5 (27 mm/s)	No rigid constraint	0.62 ± 0.46	0.64 ± 0.36	0.70 ± 0.45
	With rigid constraint	0.55 ± 0.31	0.59 ± 0.36	0.54 ± 0.31

6.4.1 Performance evaluation using experimental data

By using the new tracking algorithm, the localization achieved better performance. The failure rates were decreased from 29/9600 to 18/9600 localization runs by the TF64 scanner, and from 31/4800 to 14/4800 localization runs by the Allegro scanner. This demonstrates that the rigid-body constraint, when added to the tracking algorithm, has prevented the localization from assigning two markers to the same group, and thus reduced the failure rate to some extent. The localization is considered a failure when at least one marker has a position error larger than 5 mm (i.e. a half of the relative distance between the two closest markers).

The tracking performance is not only enhanced in success rate, but it is also in improved position accuracy. Tables 6.1 and 6.2 show comparisons between the tracking accuracy achieved by the two tracking algorithms using experimental data from both PET scanners. Interesting results were obtained. As mentioned in the previous chapter, the marker with the highest activity (Marker 1) was placed further away from the axial extremes of the FOV than the other two markers. Therefore, more coincidence lines originating from this marker were collected. Since the previous tracking algorithm treats the markers independently, Marker 1 was most of the time located with a higher accuracy than the other two markers in the previous results. However, using the new tracking algorithm with the rigid-body constraint

Table 6.2: A comparison between the previous algorithm and the new algorithm based on rigid-body transformation in terms of position error of the markers. Experimental data obtained from the **TF64** scanner were used for the comparison.

Speeds	Algorithms	Position error (mean±std) in mm		
		Marker 1	**Marker 2**	**Marker 3**
V_1 (7.5 mm/s)	No rigid constraint	0.43 ± 0.24	0.46 ± 0.27	0.48 ± 0.29
	With rigid constraint	0.41 ± 0.23	0.41 ± 0.22	0.41 ± 0.24
V_2 (12 mm/s)	No rigid constraint	0.42 ± 0.23	0.45 ± 0.25	0.46 ± 0.27
	With rigid constraint	0.40 ± 0.23	0.40 ± 0.22	0.40 ± 0.23
V_3 (17 mm/s)	No rigid constraint	0.43 ± 0.24	0.44 ± 0.25	0.46 ± 0.27
	With rigid constraint	0.39 ± 0.22	0.41 ± 0.22	0.42 ± 0.42
V_4 (21 mm/s)	No rigid constraint	0.42 ± 0.24	0.44 ± 0.25	0.47 ± 0.26
	With rigid constraint	0.42 ± 0.24	0.42 ± 0.24	0.42 ± 0.28
V_5 (27 mm/s)	No rigid constraint	0.42 ± 0.22	0.44 ± 0.25	0.47 ± 0.26
	With rigid constraint	0.40 ± 0.21	0.41 ± 0.23	0.40 ± 0.22

included, the position errors of the three markers were almost equal to each other, regardless of how different the number of coincidence lines in each group were. This demonstrates that the rigid-body constraint tends to find the best positions for the three markers as a whole, not individually. As illustrated in Tables 6.1 and 6.2, the enhancement in the position accuracy of Markers 2 and 3 (approximately 0.15 mm for Allegro and 0.05 mm for TF64) were thus more significant than that of Marker 1 (approximately 0.04 mm and 0.02 mm for Allegro and TF64, respectively).

6.4.2 Performance evaluation using simulation data

Similar to the experimental results, the tracking accuracy is also enhanced when the tracking algorithm is executed with the voxelized simulation data. The average position error of the markers have been reduced from (0.39 mm, 0.48 mm, 0.44 mm) to (0.40 mm, 0.41 mm, 0.37 mm), respectively. As seen in Fig. 6.4, due to the rigid-body constraint, the relative distances between the markers are always kept at 13 mm, 13 mm, and 10 mm. Since there are more mathematical calculations involved in the new tracking algorithm, the average computational time is increased from 3.3 ms to approximately 18 ms.

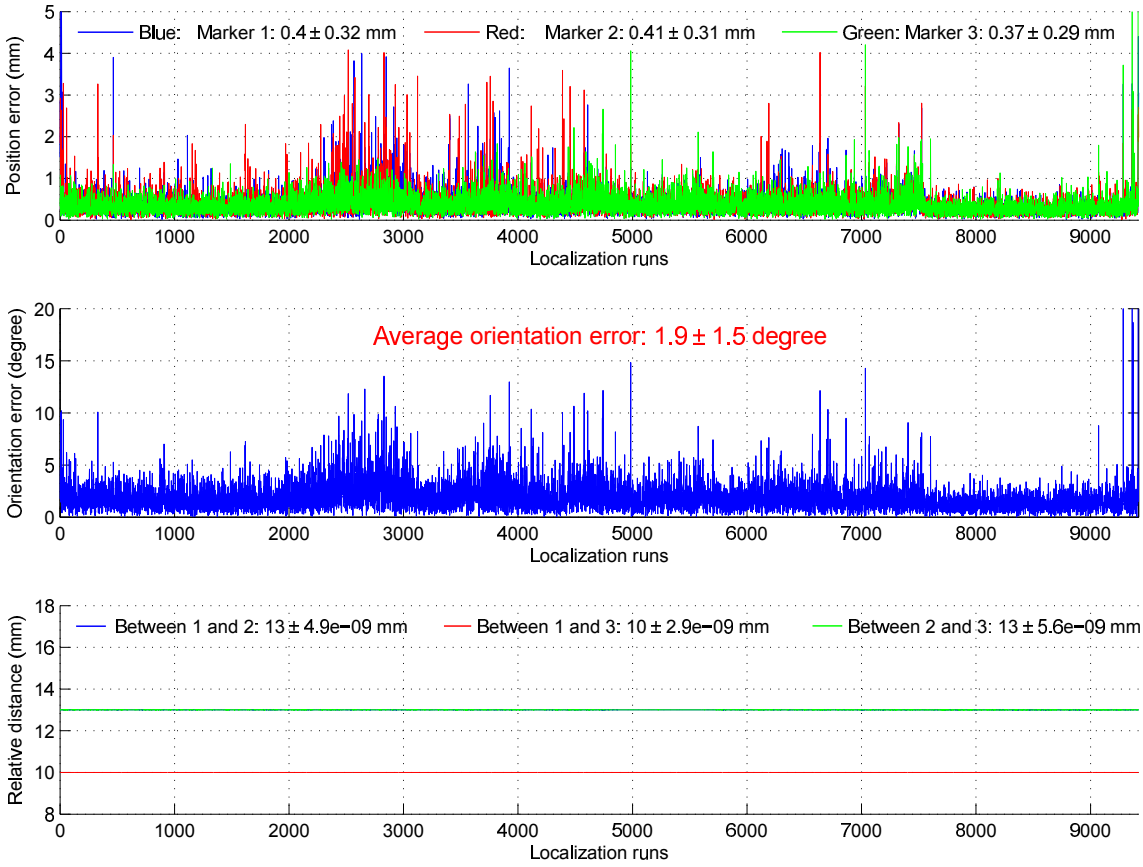

Figure 6.4: Plots of position error of each marker, orientation error of the capsule, relative distances between the markers, and computational time in every localization run using a new tracking algorithm based on rigid-body transformation and voxelized simulation data.

6.5 Discussion and summary

In the previous algorithm developed in Chapter 3, the marker position was estimated by finding the minimum-distance point in each clustered group of lines. One may argue that the relative distance constraint can also be added to the algorithm by registering the rigid-body to the final minimum-distance points. The classic problem of rigid-body transformation from a group of points to another group of points can thus be utilized in this case. Although this approach is simpler, it is not a globally optimal solution. This is due to the fact that the minimum-distance point is just a locally optimal point in each group. Registering the rigid-body to locally optimal points would not ensure the final result is globally optimized. Moreover, when one group has significantly less number of coincidence lines than the other two groups, it may be that only two groups are classified (i.e. only two minimum-distance points are found). It would lead to infinite results to transform a triangle to a group of only two points.

In this particular study, the number of markers used for localization was selected

as three to minimize the radiation dose and the cost. However, in other cases, a larger number of markers can be employed to increase the tracking accuracy. The new tracking algorithm based on rigid-body transformation is expected to be more accurate with more markers used. Assume that we have two datasets: one with 3 markers generating 3 groups of lines consisting of 2 'good' groups and 1 'bad' group; and the other one with 5 markers generating 5 groups of lines in which 4 groups are 'good' and 1 group is 'bad'. The previous tracking algorithm would fail in both datasets as the minimum-distance points of the 'bad' groups would not be found. However, as the new rigid-body based tracking algorithm treats all the groups as a whole, the increased ratio of 'good' groups over 'bad' groups (from 2/1 to 4/1) would enhance the success probability. This is because the objective function is the total sum of squared distances from each vertex to its corresponding lines. Having a greater fraction between 'good' groups and 'bad' groups would deliver a better objective function and hence result in more accurate optimization results.

To summarize, this chapter has presented a new tracking algorithm in which the constant relative distances between the markers were taken into account. In the previous algorithm, the marker position was estimated by finding the minimum-distance point in each clustered group of lines. By this way, the markers were considered as three independent objects, which did not reflect the real physical configuration of the markers on the capsule body. This resulted in localization failures at some extreme positions in the axial FOV. Based on a rigid-body transformation, the new tracking algorithm considered the markers as a whole. By finding the best position and orientation for the rigid object, the localization failure rate has been decreased significantly and the position accuracy was also enhanced.

Chapter 7

Discussion and Conclusion

7.1 Discussion

As demonstrated in the previous chapters, the proposed localization method achieved better localization performance than other localization methods that have been presented in the literature. This tracking performance can be influenced (either positively or negatively) by several factors:

- *Positron range:* The range of the positrons has an impact on the tracking accuracy. The larger the positron range, the lower the accuracy achieved. If other isotopes with higher positron range are to be used in the method, the spherical cover of the markers may be made from gold or tungsten to confine the positrons before they annihilate with electrons.
- *Non-collinearity:* Ideally, two gamma rays generated from an annihilation event travel at an angle of 180° to each other. However, due to non-collinearity, some photons are emitted not exactly 180° apart which produces wrong coincidence lines. This negatively affects the tracking accuracy. The further the distance between two opposite detector blocks is, the higher this effect contributes to the tracking performance. Therefore, the configuration of the four detector modules must be designed appropriately.
- *Patient girth:* Larger patients block more gamma rays which increases the position error. To compensate for the loss of coincidence lines input to the tracking algorithm, the radioactivity needs to be selected appropriately before the localization procedure.
- *Crystal dimension:* Since the Cartesian coordinates of the two endpoints of each coincidence line are calculated based on the position of the centroid of the

crystal that has detected the gamma ray, the width and length of the crystals have an effect on the tracking accuracy. Using smaller crystals provides a lower marker position error, but increases the cost of the detector system.

- *Detector module dimensions:* As mentioned in Chapter 4, using larger detector modules would create a larger FOV. As the capsule approaches the boundary of the FOV, the system sensitivity decreases which causes an increase in the position error. However, due to the high tracking frequency of this method, and the fact that the capsule is not allowed to move quickly in the patient's GI tract, the loss of sensitivity can be compensated by moving the patient's bed to ensure the capsule is always near the centroid of the FOV. Therefore, the dimension of each detector module does not need to be too large, and should be designed optimally depending on the speed of the capsule.

The localization parameters (position and orientation) obtained from the proposed method may be beneficial for providing feedback to actuation systems, for measuring the distance that the capsule has traveled (by which the information about which region of the GI tract the capsule is located can also be estimated), and for drug delivery, biopsy, or microsurgery. In some cases, where the endoscopists may require the anatomic location of the capsule with respect to the intestine, the proposed method can be used in conjunction with the CT imaging. Many commercial PET/CT systems take advantage of both PET and CT techniques. A CT scan can be performed first to create a reference dataset before the localization. Based on this, the anatomic position of the capsule can be estimated from its computed Cartesian coordinates.

In this proposed method, a patient is required to swallow a capsule containing three radioactive markers. In case a long half-life isotope is used in the marker, there needs to be a 100% secure method to ensure the markers not to fall out of the capsule and remain inside the patient's body. In general, similar to food, the capsule is removed from the body by normal excretion procedure after approximately eight hours (without active control). If retention occurs (very rarely), the capsule would need to be taken out by surgical means or be driven out by external magnetic fields since the capsule containing the markers could still be tracked. Another option is to use short-lived isotopes with a few hours half life. The markers then need to be produced at the clinics, ready for immediate use.

The localization method proposed in this thesis is not limited to the application of robotic endoscopic capsules, and it can be extended to track other medical devices where position and orientation information is required in diagnosis and treatment of disease. In such applications, the number of the markers embedded in the device

can be varied (i.e. more than three) with various configurations, and they would be likely to be located by an algorithm similar to the tracking algorithms presented in this thesis.

The proposed localization method is a real-time method because of the following reasons. Firstly, in this study, the localization time interval in both simulation and experimental studies were chosen as 50 ms. In other words, the proposed method was tested with a tracking frequency of 20 Hz. With this frequency, the simulation evaluation in Chapter 4 has shown that the capsule can be localized successfully when it moves with a speed of up to 40 mm/s. Similarly, successful tracking could also be achieved for a capsule moving with a speed of 27 mm/s in the experimental study in Chapter 5. These tested speeds are much greater than the maximum allowable speed of a real WCE (as it would cause discomfort to the patient if moving too fast). In addition, the computational time of the tracking algorithm for every localization time interval of 50 ms is only 3 to 6 ms. This demonstrates that real-time tracking can be delivered if the proposed method becomes reality.

7.2 Limitations

There are a few limitations of this research. Firstly, the use of three cameras for capturing the actual positions of the experimental capsule was not sufficient for the evaluation of the tracking performance. The position error was thus estimated by fitting calculated markers' positions into the pre-determined trajectory based on the experimental design. Since the position error is less than 0.5 mm, a tracking method with a high resolution of tens of μm is required to provide accurate reference data for the estimate of absolute position errors.

Secondly, due to the fact that a reduced detector system is not yet available, the experiments were conducted in clinical PET scanners whose firmware was legally not able to be modified. The performance evaluation was thus performed offline which could not demonstrate the real-time tracking benefit of the method. If online tracking is to be achieved, the loss of system sensitivity when the capsule approaches the boundary of the FOV could be compensated by moving the patient bed.

Another limitation is that the roll angle of the capsule can only be determined in a range of 0 to 180° (i.e. a roll angle change of greater than 180° will not be recognized). This is due to the configuration of the markers on the capsule's body which forms a triangle with two equal sides of 13mm. Rotating the capsule around its main axis by an angle $\alpha > 180°$ between two localization runs would be detected as $(\alpha - 180°)$. However, a capsule rotating too fast inside a GI tract would cause

discomfort to the patient. Therefore, rotating the capsule by more than 180° in a time interval of 50 ms may not be possible. One solution for this issue could be for one marker on the side of the capsule's cover to be repositioned to create a scalene triangle instead of a isosceles triangle.

7.3 Conclusion

This thesis has presented a novel localization method for robotic endoscopic capsules based on the tracking of three positron emission markers embedded in the cover of the capsule. Using both simulation data in GATE, and experimental data obtained from clinical PET scanners, the performance of the proposed method has been evaluated. The results show that this method can potentially achieve real-time tracking with an average position error of less than 0.5 mm and an average orientation error of less than 2.4°. Other important benefits of this method are that it does not occupy any space inside the capsule, it does not consume any power from the built-in battery, and that it is likely to be compatible with other actuation systems for controlling capsule movement, especially the magnetic actuation systems.

The limitations of the proposed method include the use of expensive PET scanning equipment. However, by using a significantly reduced geometry PET scanner, the cost of this method should be much lower than a commercial PET scanner. Radiation exposure to the patient could also be a disadvantage, but the radioactivity used in this localization method is significantly lower than regular levels in clinical PET imaging.

7.4 Main contributions

The main contributions of this study are:

- Development of a novel localization method for robotic endoscopic capsules by tracking multiple positron emission markers embedded in the capsule's cover. To the best of the author's knowledge, the evaluation results obtained in this thesis has shown better localization performance than other localization methods that have been reported in the literature. In addition, the proposed method overcomes other two challenging problems that the scientists are facing when developing a localization system for WCE. Firstly, due to the size constraint of the capsule, it is desired that no additional components are inserted into the capsule to maintain the battery life and to ensure the capsule

size is small enough to be swallowable. The proposed method meets this requirement since it does not occupy any capsule's inner space or consume any battery power. Secondly, magnetic actuation is anticipated to be the future solution for controlling the capsule movement. Therefore, a localization system for WCE is required to be compatible with the magnetic actuation. Since there are no interactions between gamma rays and magnetic fields, the proposed method will not encounter the interference problem between the two systems.

- Development of two tracking algorithms that can effectively determine the markers' positions from a list of two end points of coincidence lines in 3D space. In particular, the second tracking algorithm that is based on finding rigid-body transformation between multiple points and lines is much more complex than the classic matching problem that involves only two sets of points. The implementation of the algorithms was optimized to minimize the computational time while providing a high accuracy.
- Development and implementation of a number of simulations in which different models of the proposed localization systems are built in GATE.
- Design and fabrication of an experimental apparatus using the high-resolution 3D printing technique.
- Performing a performance evaluation of the proposed localization method using both simulation data and experimental data (obtained from the experiments using clinical PET scanners in the Nepean and Austin Health hospitals).

The results of this work have led to several peer-reviewed publications, as listed in Appendix C.

7.5 Recommendations for future research

The most important recommendation for future work in this study would be the development of a gamma-ray detection system similar to a conventional PET scanner but having optimally reduced geometry. This involves the optimization of crystal size, crystal type, dimensions of each of the four detector modules, the distance between two facing modules, the angle between the two pairs of modules, and so on. The experiments for system validation would need a 3D model of the GI tract in a realistic phantom together with a high resolution imaging/tracking method (CT for example) to evaluate the tracking accuracy.

It would be beneficial if the total radiation exposure from the three markers to a patient after the capsule has completed traveling through the entire GI tract could be estimated via simulation. In order to do this, the voxelized phantom needs to be a dynamic model so that the intestine can be dilated at times for the capsule to travel through. The total 3D radiation dose map can then be obtained easily using the dose actor in GATE. However, having a dynamic model of the intestine in GATE would still be a challenge.

Another future work may include the investigation of the time-of-flight (TOF) method for improving the tracking performance of the localization method. TOF has been widely used in modern commercial PET scanners to enhance the image resolution and to reduce the radioactivity requirements. Since scattered and random coincidence lines can be removed by the tracking algorithm from this study, the question of whether employing TOF would bring more benefits to the method needs still to be investigated.

References

[1] M. Yu, "M2a capsule endoscopy: A breakthrough diagnostic tool for small intestine imaging," *Gastroenterol. Nurs.*, vol. 25, no. 1, pp. 24–27, 2002.

[2] B. Laulicht, N. J. Gidmark, A. Tripathi, and E. Mathiowitz, "Localization of magnetic pills," *Proc. Natl. Acad. Sci. USA*, vol. 108, no. 6, pp. 2252–2257, 2011.

[3] J. L. Gorlewicz, S. Battaglia, B. F. Smith, G. Ciuti, J. Gerding, A. Menciassi, K. L. Obstein, P. Valdastri, and R. J. Webster, "Wireless insufflation of the gastrointestinal tract," *IEEE Trans. Biomed. Eng.*, vol. 60, no. 5, pp. 1225–1233, 2013.

[4] Y. Kusuda, "A further step beyond wireless capsule endoscopy," *Sens. Rev*, vol. 25, no. 4, pp. 259 – 260, 2005.

[5] J. D. Mellinger, "Upper gastrointestinal endoscopy: Current status," *Surg. Innov.*, vol. 10, no. 1, pp. 3–12, 2003.

[6] D. E. Fleischer, "Motion in the direction of making the video capsule our primary endoscope," *Gastrointest. Endosc.*, vol. 72, no. 2, pp. 388–391, 2010.

[7] G. Iddan, G. Meron, A. Glukhovsky, and P. Swain, "Wireless capsule endoscopy," *Nature*, vol. 405, no. 6785, pp. 417–417, 2000.

[8] A. Glukhovsky, "Wireless capsule endoscopy," *Sens. Rev*, vol. 23, no. 2, pp. 128–133, 2003.

[9] A. Moglia, A. Menciassi, S. Marc Oliver, and P. Dario, "Wireless capsule endoscopy: from diagnostic devices to multipurpose robotic systems," *Biomed. Microdevices*, vol. 9, no. 2, pp. 235–43, 2007.

[10] A. Moglia, A. Menciassi, P. Dario, and A. Cuschieri, "Capsule endoscopy: progress update and challenges ahead," *Nat. Rev. Gastroenterol. Hepatol.*, vol. 6, no. 6, pp. 353–362, 2009.

[11] A. Koulaouzidis, E. Rondonotti, and A. Karargyris, "Small-bowel capsule endoscopy: a ten-point contemporary review," *World J. Gastroenterol.*, vol. 19, no. 24, pp. 3726–46, 2013.

[12] J. L. Toennies, G. Tortora, M. Simi, P. Valdastri, and R. J. Webster, "Swallowable medical devices for diagnosis and surgery: the state of the art," *Proc. Inst. Mech. Eng. C J. Mech. Eng. Sci.*, vol. 224, no. 7, pp. 1397–1414, 2010.

[13] G. Ciuti, A. Menciassi, and P. Dario, "Capsule endoscopy: From current achievements to open challenges," *IEEE Rev. Biomed. Eng*, vol. 4, pp. 59–72, 2011.

[14] X. Wang and M. Q. H. Meng, "Perspective of active capsule endoscope: actuation and localisation," *Int. J. Mech. Autom*, vol. 1, pp. 38–45, 2011.

[15] U. Kopylov and E. G. Seidman, "Clinical applications of small bowel capsule endoscopy," *Clin. Exp. Gastroenterol*, vol. 6, pp. 129–37, 2013.

[16] K. Kong, D. Jeon, S. Yim, and S. Choi, "A robotic biopsy device for capsule endoscopy," *J. Med. Devices*, vol. 6, no. 3, pp. 031 004–031 012, 2012.

[17] S. P. Woods and T. G. Constandinou, "Wireless capsule endoscope for targeted drug delivery: Mechanics and design considerations," *IEEE Trans. Biomed. Eng.*, vol. 60, no. 4, pp. 945–953, 2013.

[18] K. Pahlavan, G. Bao, Y. Ye, S. Makarov, U. Khan, P. Swar, D. Cave, A. Karellas, P. Krishnamurthy, and K. Sayrafian, "Rf localization for wireless video capsule endoscopy," *Int. J. Wireless Inform. Network*, vol. 19, no. 4, pp. 326–340, 2012.

[19] F. Munoz, G. Alici, and W. Li, "A review of drug delivery systems for capsule endoscopy," *Adv. Drug Deliv. Rev.*, vol. 71, no. 0, pp. 77–85, 2014.

[20] B. J. Nelson, I. K. Kaliakatsos, and J. J. Abbott, "Microrobots for minimally invasive medicine," *Annu. Rev. Biomed. Eng.*, vol. 12, pp. 55–85, 2010.

[21] A. Arezzo, A. Menciassi, P. Valdastri, G. Ciuti, G. Lucarini, M. Salerno, C. Di Natali, M. Verra, P. Dario, and M. Morino, "Experimental assessment of a novel robotically-driven endoscopic capsule compared to traditional colonoscopy," *Dig. Liver Dis.*, vol. 45, no. 8, pp. 657–662, 2013.

[22] T. D. Than, G. Alici, H. Zhou, and W. Li, "A review of localization systems for robotic endoscopic capsules," *IEEE Trans. Biomed. Eng.*, vol. 59, no. 9, pp. 2387–2399, 2012.

[23] H. Chao, L. Mao, S. Shuang, Y. Wan'an, Z. Rui, and M. Q. H. Meng, "A cubic 3-axis magnetic sensor array for wirelessly tracking magnet position and orientation," *IEEE Sens. J.*, vol. 10, no. 5, pp. 903–913, 2010.

[24] N. C. Atuegwu and R. L. Galloway, "Volumetric characterization of the aurora magnetic tracker system for image-guided transorbital endoscopic procedures," *Phys. Med. Biol.*, vol. 53, no. 16, p. 4355, 2008.

[25] G. Ciuti, P. Valdastri, A. Menciassi, and P. Dario, "Robotic magnetic steering and locomotion of capsule endoscope for diagnostic and surgical endoluminal procedures," *Robotica*, vol. 28, no. Special Issue 02, pp. 199–207, 2010.

[26] F. Carpi, N. Kastelein, M. Talcott, and C. Pappone, "Magnetically controllable gastrointestinal steering of video capsules," *IEEE Trans. Biomed. Eng.*, vol. 58, no. 2, pp. 231–234, 2011.

[27] G. Mingyuan, H. Chengzhi, C. Zhenzhi, Z. Honghai, and L. Sheng, "Design and fabrication of a magnetic propulsion system for self-propelled capsule endoscope," *IEEE Trans. Biomed. Eng.*, vol. 57, no. 12, pp. 2891–2902, 2010.

[28] J. S. Lee, B. Kim, and Y. S. Hong, "A flexible chain-based screw propeller for capsule endoscopes," *Int. J. Precis. Eng. Manuf.*, vol. 10, no. 4, pp. 27–34, 2009.

[29] A. Uchiyama, H. Kawano, K. Arai, K. Ishiyama, and M. Sendoh, "Medical device guidance system," *U. S. Patent*, no. 7711408, 2010.

[30] Z. Yongshun, J. Shengyuan, Z. Xuewen, R. Xiaoyan, and G. Dongming, "A variable-diameter capsule robot based on multiple wedge effects," *IEEE/ASME T. Mech*, vol. 16, no. 2, pp. 241–254, 2011.

[31] C. Yu, J. Kim, H. Choi, J. Choi, S. Jeong, K. Cha, J.-o. Park, and S. Park, "Novel electromagnetic actuation system for three-dimensional locomotion and drilling of intravascular microrobot," *Sensor. Actuat. A-Phys*, vol. 161, no. 1-2, pp. 297–304, 2010.

[32] M. Lam and M. Mintchev, "Diamagnetically stabilized levitation control of an intraluminal magnetic capsule," *Physiol. Meas.*, vol. 30, no. 8, p. 763, 2009.

[33] I. K. Mohammed, B. S. Sharif, J. A. Neasham, and D. Giaouris, "Novel mimo 4-dof position control for capsule endoscope," in *2011 IEEE International Symposium on Circuits and Systems (ISCAS)*, 2011, pp. 909–912.

[34] P. Swain, A. Toor, F. Volke, J. Keller, J. Gerber, E. Rabinovitz, and R. I. Rothstein, "Remote magnetic manipulation of a wireless capsule endoscope in

the esophagus and stomach of humans (with videos)," *Gastrointest. Endosc.*, vol. 71, no. 7, pp. 1290–1293, 2010.

[35] J. Coey, *Magnetism and Magnetic Materials*. Cambridge University Press, 2010.

[36] W. Weitschies, J. Wedemeyer, R. Stehr, and L. Trahms, "Magnetic markers as a noninvasive tool to monitor gastrointestinal transit," *IEEE Trans. Biomed. Eng.*, vol. 41, no. 2, pp. 192–195, 1994.

[37] W. Weitschies, R. Ktitz, D. Cordini, and L. Trahms, "High-resolution monitoring of the gastrointestinal transit of a magnetically marked capsule," *J. Pharm. Sci.*, vol. 86, no. 11, pp. 1218–1222, 1997.

[38] V. Schlageter, P. A. Besse, R. S. Popovic, and P. Kucera, "Tracking system with five degrees of freedom using a 2d-array of hall sensors and a permanent magnet," *Sensor. Actuat. A-Phys*, vol. 92, no. 1-3, pp. 37–42, 2001.

[39] V. Schlageter, P. Drljaca, R. S. Popovic, Ku, and P. Era, "A magnetic tracking system based on highly sensitive integrated hall sensors," *JSME International Journal Series C Mechanical Systems, Machine Elements and Manufacturing*, vol. 45, no. 4, pp. 967–973, 2002.

[40] S. M. Aziz, M. Grcic, and T. Vaithianathan, *A Real-Time Tracking System for an Endoscopic Capsule using Multiple Magnetic Sensors*, ser. Lecture Notes in Electrical Engineering. Springer Berlin Heidelberg, 2008, vol. 20, pp. 201–218.

[41] X. Wu, W. Hou, C. Peng, X. Zheng, X. Fang, and J. He, "Wearable magnetic locating and tracking system for mems medical capsule," *Sensor. Actuat. A-Phys*, vol. 141, no. 2, pp. 432–439, 2008.

[42] A. Plotkin and E. Paperno, "3-d magnetic tracking of a single subminiature coil with a large 2-d array of uniaxial transmitters," *IEEE Trans. Magn.*, vol. 39, no. 5, pp. 3295–3297, 2003.

[43] A. Plotkin, V. Kucher, Y. Horen, and E. Paperno, "A new calibration procedure for magnetic tracking systems," *IEEE Trans. Magn.*, vol. 44, no. 11, pp. 4525–4528, 2008.

[44] B. J. Kroger, M. Pouplier, and M. K. Tiede, "An evaluation of the aurora system as a flesh-point tracking tool for speech production research," *J. Speech Lang. Hear. Res.*, vol. 51, no. 4, pp. 914–21, 2008.

[45] T. Nagaoka and A. Uchiyama, "Development of a small wireless position sensor for medical capsule devices," in *26th Annual International Conference of the*

IEEE Engineering in Medicine and Biology Society (IEMBS), vol. 1, 2004, pp. 2137–2140.

[46] X. Guo, G. Yan, and W. He, "A novel method of three-dimensional localization based on a neural network algorithm," *J. Med. Eng. Technol.*, vol. 33, no. 3, pp. 192–198, 2009.

[47] X. Guo, G. Yan, W. He, and P. Jiang, "Improved modeling of electromagnetic localization for implantable wireless capsules," *Biomed. Instrum. Technol*, vol. 44, no. 4, pp. 354–359, 2010.

[48] X. Guo, C. Wang, and R. Yan, "An electromagnetic localization method for medical micro-devices based on adaptive particle swarm optimization with neighborhood search," *Measurement*, vol. 44, no. 5, pp. 852–858, 2011.

[49] D. Roetenberg, C. T. Baten, and P. H. Veltink, "Estimating body segment orientation by applying inertial and magnetic sensing near ferromagnetic materials," *IEEE Trans. Neural Syst. Rehabil. Eng.*, vol. 15, no. 3, pp. 469–71, 2007.

[50] I. Aoki, A. Uchiyama, K. Arai, K. Ishiyama, and S. Yabukami, "Detecting system of position and posture of capsule medical device," *U. S. Patent*, no. US7815563 B2, pp. 1–58, 2010.

[51] S. Hashi, S. Yabukami, H. Kanetaka, K. Ishiyama, and K. I. Arai, "Wireless magnetic position-sensing system using optimized pickup coils for higher accuracy," *IEEE Trans. Magn.*, vol. 47, no. 10, pp. 3542–3545, 2011.

[52] S. Hashi, S. Yabukami, H. Kanetaka, K. Ishiyama, and K. I. Arai, "Numerical study on the improvement of detection accuracy for a wireless motion capture system," *IEEE Trans. Magn.*, vol. 45, no. 6, pp. 2736–2739, 2009.

[53] R. Graumann, "Cable-free endoscopy method and system for determining in vivo position and orientation of an endoscopy capsule," *U. S. Patent*, no. 20050187479, 2005.

[54] M.-G. Kim, Y.-S. Hong, and E.-J. Lim, "Position and orientation detection of capsule endoscopes in spiral motion," *Int. J. Precis. Eng. Manuf.*, vol. 11, no. 1, pp. 31–37, 2010.

[55] K. M. Miller, A. W. Mahoney, T. Schmid, and J. J. Abbott, "Proprioceptive magnetic-field sensing for closed-loop control of magnetic capsule endoscopes," in *2012 IEEE/RSJ International Conference on Intelligent Robots and Systems (IROS)*, 2012, pp. 1994–1999.

[56] M. Salerno, G. Ciuti, G. Lucarini, R. Rizzo, P. Valdastri, A. Menciassi, A. Landi, and P. Dario, "A discrete-time localization method for capsule endoscopy based on on-board magnetic sensing," *Meas. Sci. Technol*, vol. 23, no. 1, pp. 015 701–015 710, 2012.

[57] C. Di Natali, M. Beccani, and P. Valdastri, "Real-time pose detection for magnetic medical devices," *IEEE Trans. Magn.*, vol. 49, no. 7, pp. 3524–3527, 2013.

[58] M. R. Basar, F. Malek, K. M. Juni, M. S. Idris, and M. I. M. Saleh, "Ingestible wireless capsule technology: A review of development and future indication," *Int. J. Antenn. Propag*, vol. 2012, pp. 1–14, 2012.

[59] K. Yu, I. Sharp, and Y. Guo, *Ground-Based Wireless Positioning*, ser. Ground-Based Wireless Positioning. Wiley, 2009.

[60] Y. Kegen, F. Gengfa, and E. Dutkiewicz, "Position and orientation accuracy analysis for wireless endoscope magnetic field based localization system design," in *2010 IEEE Wireless Communications and Networking Conference (WCNC)*, 2010, pp. 1–6.

[61] K. Arshak, F. Adepoju, and D. Waldron, "A review and adaptation of methods of object tracking to telemetry capsules," *Int. J. Comput. Med. Sci. Image Process*, vol. 1, no. 1, pp. 35–46, 2007.

[62] K. Arshak and F. Adepoju, "Adaptive linearized methods for tracking a moving telemetry capsule," in *IEEE International Symposium on Industrial Electronics (IEEE-ISIE)*, 2007, pp. 2703–2708.

[63] D. Fischer, R. Shreiber, G. Meron, M. Frisch, H. Jacob, A. Glukhovsky, and A. Engel, "Localization of the wireless capsule endoscope in its passage through the gi tract," *Gastrointest. Endosc.*, vol. 53, no. 5, p. AB126, 2001.

[64] D. Fischer, R. Schreiber, D. Levi, and R. Eliakim, "Capsule endoscopy: the localization system," *Gastrointest. Endosc. Clin. N. Am.*, vol. 14, no. 1, pp. 25–31, 2004.

[65] V. Erceg, L. J. Greenstein, S. Y. Tjandra, S. R. Parkoff, A. Gupta, B. Kulic, A. A. Julius, and R. Bianchi, "An empirically based path loss model for wireless channels in suburban environments," *IEEE J. Select. Areas Commun*, vol. 17, no. 7, pp. 1205–1211, 1999.

[66] T. Shah, S. M. Aziz, and T. Vaithianathan, "Development of a tracking algorithm for an in-vivo rf capsule prototype," in *International Conference on Electrical and Computer Engineering (ICECE)*, 2006, pp. 173–176.

[67] W. Lujia, H. Chao, T. Longqiang, L. Mao, and M. Q. H. Meng, "A novel radio propagation radiation model for location of the capsule in gi tract," in *2009 IEEE International Conference on Robotics and Biomimetics (ROBIO)*, 2009, pp. 2332–2337.

[68] W. Lujia, L. Li, H. Chao, and M. Q. H. Meng, "A novel rf-based propagation model with tissue absorption for location of the gi tract," in *2010 Annual International Conference of the IEEE Engineering in Medicine and Biology Society (EMBC)*, 2010, pp. 654–657.

[69] W. Yi, F. Ruijun, Y. Yunxing, U. Khan, and K. Pahlavan, "Performance bounds for rf positioning of endoscopy camera capsules," in *2011 IEEE Topical Conference on Biomedical Wireless Technologies, Networks, and Sensing Systems (BioWireleSS)*, 2011, pp. 71–74.

[70] H. Jinlong, Z. Yongxin, Z. Le, F. Yuzhuo, Z. Feng, Y. Li, and R. Guoguang, "Design and implementation of a high resolution localization system for in-vivo capsule endoscopy," in *8th IEEE International Conference on Dependable, Autonomic and Secure Computing (DASC)*, 2009, pp. 209–214.

[71] Z. Le, Z. Yongxin, M. Tingting, H. Jinlong, and H. Hao, "Design of 3d positioning algorithm based on rfid receiver array for in vivo micro-robot," in *8th IEEE International Conference on Dependable, Autonomic and Secure Computing (DASC)*, 2009, pp. 749–753.

[72] L. Zhang, Y. Zhu, T. Mo, J. Hou, and G. Rong, "Design and implementation of 3d positioning algorithms based on rf signal radiation patterns for in vivo micro-robot," in *2010 International Conference on Body Sensor Networks (BSN)*, 2010, pp. 255–260.

[73] C. Hekimian-Williams, B. Grant, L. Xiuwen, Z. Zhenghao, and P. Kumar, "Accurate localization of rfid tags using phase difference," in *2010 IEEE International Conference on RFID*, 2010, pp. 89–96.

[74] A. Wille, M. Broll, and S. Winter, "Phase difference based rfid navigation for medical applications," in *Proc. IEEE Int. Conf. Radio Freq. Identif.*, 2011, pp. 98–105.

[75] R. Chandra, A. J. Johansson, and F. Tufvesson, "Localization of an rf source inside the human body for wireless capsule endoscopy," in *Proceedings of the 8th International Conference on Body Area Networks (BodyNets)*. ICST, 2013, pp. 48–54.

[76] K. Duda, T. Zielinski, R. Fraczek, J. Bulat, and M. Duplaga, "Localization of endoscopic capsule in the gi tract based on mpeg-7 visual descriptors," in *IEEE International Workshop on Imaging Systems and Techniques (IST)*, 2007, pp. 1–4.

[77] J. Bulat, K. Duda, M. Duplaga, R. Fraczek, A. Skalski, M. Socha, P. Turcza, and T. P. Zielinski, "Data processing tasks in wireless gi endoscopy: Image-based capsule localization, navigation and video compression," in *29th Annual International Conference of the IEEE Engineering in Medicine and Biology Society (EMBS).*, 2007, pp. 2815–2818.

[78] J. Lee, J. Oh, S. K. Shah, X. Yuan, and S. J. Tang, "Automatic classification of digestive organs in wireless capsule endoscopy videos," in *Proceedings of the 2007 ACM symposium on Applied computing*, 2007, pp. 1041–1045.

[79] D. K. Iakovidis, E. Spyrou, D. Diamantis, and I. Tsiompanidis, "Capsule endoscope localization based on visual features," in *2013 IEEE 13th International Conference on Bioinformatics and Bioengineering (BIBE)*, 2013, pp. 1–4.

[80] S. Evaggelos and K. I. Dimitris, "Video-based measurements for wireless capsule endoscope tracking," *Meas. Sci. Technol*, vol. 25, no. 1, p. 015002, 2014.

[81] L. Li, H. Chao, C. Wentao, and M. Q. H. Meng, "Capsule endoscope localization based on computer vision technique," in *Annual International Conference of the IEEE Engineering in Medicine and Biology Society (EMBC)*, 2009, pp. 3711–3714.

[82] R. Kuth, J. Reinschke, and R. Rockelein, "Method for determining the position and orientation of an endoscopy capsule guided through an examination object by using a navigating magnetic field generated by means of a navigation device," *U. S. Patent*, no. 20070038063, 2007.

[83] J. Boese, N. Rahn, and B. Sandkamp, "Method for determining the position and orientation of an object, especially of a catheter, from two-dimensional x-ray images," *U. S. Patent*, no. 7801342, 2010.

[84] I. Wilding, P. Hirst, and A. Connor, "Development of a new engineering-based capsule for human drug absorption studies," *Pharm. Sci. Technol. To*, vol. 3, no. 11, pp. 385–392, 2000.

[85] I. R. Wilding, A. J. Coupe, and S. S. Davis, "The role of [gamma]-scintigraphy in oral drug delivery," *Adv. Drug Deliv. Rev.*, vol. 46, no. 1-3, pp. 103–124, 2001.

[86] C. L. Dumoulin, S. P. Souza, and R. D. Darrow, "Real-time position monitoring of invasive devices using magnetic resonance," *Magn. Reson. Med*, vol. 29, no. 3, pp. 411–415, 1993.

[87] S. Martel, M. Mohammadi, O. Felfoul, Z. Lu, and P. Pouponneau, "Flagellated magnetotactic bacteria as controlled mri-trackable propulsion and steering systems for medical nanorobots operating in the human microvasculature," *Int. J. Robot. Res*, vol. 28, no. 4, pp. 571–582, 2009.

[88] A. Krieger, R. C. Susil, C. Menard, J. A. Coleman, G. Fichtinger, E. Atalar, and L. L. Whitcomb, "Design of a novel mri compatible manipulator for image guided prostate interventions," *IEEE Trans. Biomed. Eng.*, vol. 52, no. 2, pp. 306–313, 2005.

[89] A. Krieger, G. Metzger, G. Fichtinger, E. Atalar, and L. L. Whitcomb, "A hybrid method for 6-dof tracking of mri-compatible robotic interventional devices," in *2006 IEEE International Conference on Robotics and Automation (ICRA)*, 2006, pp. 3844–3849.

[90] A. Krieger, I. I. Iordachita, P. Guion, A. K. Singh, A. Kaushal, C. Menard, P. A. Pinto, K. Camphausen, G. Fichtinger, and L. L. Whitcomb, "An mri-compatible robotic system with hybrid tracking for mri-guided prostate intervention," *IEEE Trans. Biomed. Eng.*, vol. 58, no. 11, pp. 3049–3060, 2011.

[91] M. Fluckiger and B. J. Nelson, "Ultrasound emitter localization in heterogeneous media," in *29th Annual International Conference of the IEEE Engineering in Medicine and Biology Society (EMBC)*, 2007, pp. 2867–2870.

[92] K. Arshak and F. Adepoju, "Object tracking in the gi tract: a novel microcontroller approach," in *9th IEEE International Workshop on Advanced Motion Control (AMC)*, 2006, pp. 494–499.

[93] Z. Nagy, M. Fluckiger, O. Ergeneman, S. Pane, M. Probst, and B. J. Nelson, "A wireless acoustic emitter for passive localization in liquids," in *Proc. IEEE Int. Conf. Robot. Autom (ICRA)*, 2009, pp. 2593–2598.

[94] F. Carpi and H. Shaheed, "Grand challenges in magnetic capsule endoscopy," *Expert Rev. Med. Devices*, vol. 10, no. 4, pp. 433–6, 2013.

[95] T. K. Lewellen, "Recent developments in pet detector technology," *Phys. Med. Biol.*, vol. 53, no. 17, p. R287, 2008.

[96] T. Xu, J. T. Wong, P. M. Shikhaliev, J. L. Ducote, M. S. Al-Ghazi, and S. Molloi, "Real-time tumor tracking using implanted positron emission markers: Concept and simulation study," *Med. Phys.*, vol. 33, no. 7, pp. 2598–2609, 2006.

[97] M. Chamberland, R. Wassenaar, B. Spencer, and T. Xu, "Performance evaluation of real-time motion tracking using positron emission fiducial markers," *Med. Phys.*, vol. 38, no. 2, pp. 810–819, 2011.

[98] T. D. Than, G. Alici, S. Harvey, H. Zhou, and W. Li, "Concept and simulation study of a novel localization method for robotic endoscopic capsules using multiple positron emission markers," *Med. Phys.*, vol. 41, no. 7, p. 072501, 2014.

[99] N. W. Churchill, M. Chamberland, and T. Xu, "Algorithm and simulation for real-time positron emission based tumor tracking using a linear fiducial marker," *Med. Phys.*, vol. 36, no. 5, pp. 1576–1586, 2009.

[100] J. C. Bezdek, *Pattern Recognition with Fuzzy Objective Function Algorithms.* Kluwer Academic Publishers, 1981.

[101] A. Wheeler and A. Ganji, *Introduction to Engineering Experimentation.* Pearson Higher Education, 2010.

[102] C. Schiepers and M. Dahlbom, "Molecular imaging in oncology: the acceptance of pet/ct and the emergence of mr/pet imaging," *Eur. Radiol.*, vol. 21, no. 3, pp. 548–54, 2011.

[103] H. Cember and T. Johnson, *Introduction to Health Physics: Fourth Edition.* Mcgraw-hill, 2008.

[104] J. H. Hubbell and S. M. Seltzer, *Tables of X-ray Mass Attenuation Coefficients and Mass Energy-Absorption Coefficients from 1 keV to 20 MeV for Elements Z = 1 to 92 and 48 Additional Substances of Dosimetric Interest*, 43rd ed. U.S. Department of Commerce, Gaithersburg, MD, 1996.

[105] S. Jan, G. Santin, D. Strul, S. Staelens, K. Assi, D. Autret, S. Avner, R. Barbier, M. Bardis, P. M. Bloomfield, D. Brasse, V. Breton, P. Bruyndonckx, I. Buvat, A. F. Chatziioannou, Y. Choi, Y. H. Chung, C. Comtat, D. Donnarieix, L. Ferrer, S. J. Glick, C. J. Groiselle, D. Guez, P.-F. Honore, S. Kerhoas-Cavata, A. S. Kirov, V. Kohli, M. Koole, M. Krieguer, D. J. v. d. Laan, F. Lamare, G. Largeron, C. Lartizien, D. Lazaro, M. C. Maas, L. Maigne, F. Mayet, F. Melot, C. Merheb, E. Pennacchio, J. Perez, U. Pietrzyk, F. R. Rannou, M. Rey, D. R. Schaart, C. R. Schmidtlein, L. Simon, T. Y. Song, J.-M. Vieira, D. Visvikis, R. V. d. Walle, E. Wiers, and C. Morel, "Gate: a simulation toolkit for pet and spect," *Phys. Med. Biol.*, vol. 49, no. 19, p. 4543, 2004.

[106] F. Lamare, A. Turzo, Y. Bizais, C. C. L. Rest, and D. Visvikis, "Validation of a monte carlo simulation of the philips allegro/gemini pet systems using gate," *Phys. Med. Biol.*, vol. 51, no. 4, p. 943, 2006.

[107] C. Merheb, S. Nicol, Y. Petegnief, J.-N. Talbot, and I. Buvat, "Assessment of the mosaic animal pet system response using list-mode data for validation of gate monte carlo modelling," *Nucl. Instr. Meth. Phys. Res. A*, vol. 569, no. 2, pp. 220–224, 2006.

[108] C. R. Schmidtlein, A. S. Kirov, S. A. Nehmeh, Y. E. Erdi, J. L. Humm, H. I. Amols, L. M. Bidaut, A. Ganin, C. W. Stearns, D. L. McDaniel, and K. A. Hamacher, "Validation of gate monte carlo simulations of the ge advance/discovery ls pet scanners," *Med. Phys.*, vol. 33, no. 1, pp. 198–208, 2006.

[109] F. Bataille, C. Comtat, S. Jan, and R. Trebossen, "Monte carlo simulation for the ecat hrrt using gate," in *2004 IEEE Nucl. Sci. Conf. R*, vol. 4, 2004, pp. 2570–2574.

[110] W. P. Segars, G. Sturgeon, S. Mendonca, J. Grimes, and B. M. Tsui, "4d xcat phantom for multimodality imaging research," *Med. Phys.*, vol. 37, no. 9, pp. 4902–15, 2010.

[111] S. Agostinelli, J. Allison, K. Amako, J. Apostolakis, H. Araujo, P. Arce, M. Asai, D. Axen, S. Banerjee, G. Barrand, F. Behner, L. Bellagamba, J. Boudreau, L. Broglia, A. Brunengo, H. Burkhardt, S. Chauvie, J. Chuma, R. Chytracek, G. Cooperman, G. Cosmo, P. Degtyarenko, A. Dell'Acqua, G. Depaola, D. Dietrich, R. Enami, A. Feliciello, C. Ferguson, H. Fesefeldt, G. Folger, F. Foppiano, A. Forti, S. Garelli, S. Giani, R. Giannitrapani, D. Gibin, J. J. Gmez Cadenas, I. Gonzlez, G. Gracia Abril, G. Greeniaus, W. Greiner, V. Grichine, A. Grossheim, S. Guatelli, P. Gumplinger, R. Hamatsu, K. Hashimoto, H. Hasui, A. Heikkinen, A. Howard, V. Ivanchenko, A. Johnson, F. W. Jones, J. Kallenbach, N. Kanaya, M. Kawabata, Y. Kawabata, M. Kawaguti, S. Kelner, P. Kent, A. Kimura, T. Kodama, R. Kokoulin, M. Kossov, H. Kurashige, E. Lamanna, T. Lampn, V. Lara, V. Lefebure, F. Lei, M. Liendl, W. Lockman, F. Longo, S. Magni, M. Maire, E. Medernach, K. Minamimoto, P. Mora de Freitas, Y. Morita, K. Murakami, M. Nagamatu, R. Nartallo, P. Nieminen, T. Nishimura, K. Ohtsubo, M. Okamura, S. O'Neale, Y. Oohata, K. Paech, J. Perl, A. Pfeiffer, M. G. Pia, F. Ranjard, A. Rybin, S. Sadilov, E. Di Salvo, G. Santin, T. Sasaki, N. Savvas, Y. Sawada *et al.*, "Geant4a simulation toolkit," *Nucl. Instr. Meth. Phys. Res. A*, vol. 506, no. 3, pp. 250–303, 2003.

[112] J. Allison, K. Amako, J. Apostolakis, H. Araujo, P. A. Dubois, M. Asai, G. Barrand, R. Capra, S. Chauvie, R. Chytracek, G. A. P. Cirrone, G. Cooperman, G. Cosmo, G. Cuttone, G. G. Daquino, M. Donszelmann, M. Dressel, G. Folger, F. Foppiano, J. Generowicz, V. Grichine, S. Guatelli, P. Gumplinger, A. Heikkinen, I. Hrivnacova, A. Howard, S. Incerti, V. Ivanchenko, T. Johnson,

F. Jones, T. Koi, R. Kokoulin, M. Kossov, H. Kurashige, V. Lara, S. Larsson, F. Lei, O. Link, F. Longo, M. Maire, A. Mantero, B. Mascialino, I. McLaren, P. M. Lorenzo, K. Minamimoto, K. Murakami, P. Nieminen, L. Pandola, S. Parlati, L. Peralta, J. Perl, A. Pfeiffer, M. G. Pia, A. Ribon, P. Rodrigues, G. Russo, S. Sadilov, G. Santin, T. Sasaki, D. Smith, N. Starkov, S. Tanaka, E. Tcherniaev, B. Tome, A. Trindade, P. Truscott, L. Urban, M. Verderi, A. Walkden, J. P. Wellisch, D. C. Williams, D. Wright, and H. Yoshida, "Geant4 developments and applications," *Nuclear Science, IEEE Transactions on*, vol. 53, no. 1, pp. 270–278, 2006.

[113] S. Jan, D. Benoit, E. Becheva, T. Carlier, F. Cassol, P. Descourt, T. Frisson, L. Grevillot, L. Guigues, L. Maigne, C. Morel, Y. Perrot, N. Rehfeld, D. Sarrut, D. R. Schaart, S. Stute, U. Pietrzyk, D. Visvikis, N. Zahra, and I. Buvat, "Gate v6: a major enhancement of the gate simulation platform enabling modelling of ct and radiotherapy," *Phys. Med. Biol.*, vol. 56, no. 4, p. 881, 2011.

[114] M. Caon, "Voxel-based computational models of real human anatomy: a review," *Radiat. Environ. Biophys.*, vol. 42, no. 4, pp. 229–35, 2004.

[115] W. P. Segars and B. M. W. Tsui, "Mcat to xcat: The evolution of 4-d computerized phantoms for imaging research," *Proceedings of the IEEE*, vol. 97, no. 12, pp. 1954–1968, 2009.

[116] V. Abella, R. Miro, B. Juste, and G. Verdu, "Computation of a voxelized antropomorphic phantom from computer tomography slices and 3d dose distribution calculation utilizing the mcnp5 code," in *Proceedings of the Seventh International Topical Meeting on Industrial Radiation and Radioisotope Measurement Application*, 2008.

[117] M. Chamberland, "Performance evaluation and algorithm development for real-time tumour tracking using positron emission markers," Master thesis, Carleton University, 2009.

[118] S. Surti, A. Kuhn, M. E. Werner, A. E. Perkins, J. Kolthammer, and J. S. Karp, "Performance of philips gemini tf pet/ct scanner with special consideration for its time-of-flight imaging capabilities," *J. Nucl. Med.*, vol. 48, no. 3, pp. 471–80, 2007.

[119] K. S. Arun, T. S. Huang, and S. D. Blostein, "Least-squares fitting of two 3-d point sets," *IEEE Trans. Pattern Anal. Machine. Intell*, vol. PAMI-9, no. 5, pp. 698–700, 1987.

[120] B. K. P. Horn, H. M. Hilden, and S. Negahdaripour, "Closed-form solution of absolute orientation using orthonormal matrices," *J. Opt. Soc. Am. A*, vol. 5, no. 7, pp. 1127–1135, 1988.

[121] B. K. P. Horn, "Closed-form solution of absolute orientation using unit quaternions," *J. Opt. Soc. Am. A*, vol. 4, no. 4, pp. 629–642, 1987.

[122] M. Hersch, A. Billard, and S. Bergmann, "Iterative estimation of rigid-body transformations," *J Math Imaging Vis*, vol. 43, no. 1, pp. 1–9, 2012.

[123] K. Halvorsen, T. Soderstrom, V. Stokes, and H. Lanshammar, "Using an extended kalman filter for rigid body pose estimation," *J. Biomech. Eng.*, vol. 127, no. 3, pp. 475–83, 2005.

[124] D. Koks, *Explorations in Mathematical Physics: The Concepts Behind an Elegant Language*. Springer, 2006.

Appendix A
GATE macros

1. GATE macros for designing a full-ring detector system based on Phillips Allegro PET scanner

```
# WORLD
/gate/world/geometry/setXLength 110. cm
/gate/world/geometry/setYLength 110. cm
/gate/world/geometry/setZLength 50. cm

# CYLINDRICAL
/gate/world/daughters/name cylindricalPET
/gate/world/daughters/insert cylinder
/gate/cylindricalPET/setMaterial Air
/gate/cylindricalPET/geometry/setRmax 52. cm
/gate/cylindricalPET/geometry/setRmin 28. cm
/gate/cylindricalPET/geometry/setHeight 18.3 cm
/gate/cylindricalPET/vis/forceWireframe
/gate/cylindricalPET/vis/setVisible 0

# RSECTOR
/gate/cylindricalPET/daughters/name rsector
/gate/cylindricalPET/daughters/insert box
/gate/rsector/geometry/setXLength 40 mm
/gate/rsector/geometry/setYLength 94.5 mm
/gate/rsector/geometry/setZLength 18.3 cm
/gate/rsector/setMaterial Glass
/gate/rsector/placement/setTranslation 45.2 0 0 cm
/gate/rsector/vis/forceWireframe
/gate/rsector/vis/setColor red
```

```
#/gate/rsector/vis/setVisible 0

# MODULE
/gate/rsector/daughters/name module
/gate/rsector/daughters/insert box
/gate/module/geometry/setXLength 20. mm
/gate/module/geometry/setYLength 94.5 mm
/gate/module/geometry/setZLength 18.3 cm
/gate/module/setMaterial PTFE
/gate/module/placement/setTranslation -10. 0 0 mm
/gate/module/vis/forceWireframe
/gate/module/vis/setColor cyan
#/gate/module/vis/setVisible 0

# CRYSTAL
/gate/module/daughters/name crystal
/gate/module/daughters/insert box
/gate/crystal/geometry/setXLength 20. mm
/gate/crystal/geometry/setYLength 4 mm
/gate/crystal/geometry/setZLength 6 mm
/gate/crystal/setMaterial GSO
/gate/crystal/vis/setColor yellow
#/gate/crystal/vis/setVisible 0

# LAYER GSO
/gate/crystal/daughters/name GSO
/gate/crystal/daughters/insert box
/gate/GSO/geometry/setXLength 20. mm
/gate/GSO/geometry/setYLength 4 mm
/gate/GSO/geometry/setZLength 6 mm
/gate/GSO/setMaterial GSO
/gate/GSO/vis/setColor yellow
#/gate/GSO/vis/setVisible 0

# REPEAT CRYSTAL INTO THE WHOLE MODULE
/gate/crystal/repeaters/insert cubicArray
/gate/crystal/cubicArray/setRepeatNumberX 1
/gate/crystal/cubicArray/setRepeatNumberY 22
/gate/crystal/cubicArray/setRepeatNumberZ 29
/gate/crystal/cubicArray/setRepeatVector 0. 4.3 6.3 mm

# REPEAT THE RSECTOR INTO THE WHOLE RING
```

```
/gate/rsector/repeaters/insert ring
/gate/rsector/ring/setRepeatNumber 28

# ATTACH SYSTEM
/gate/systems/cylindricalPET/rsector/attach rsector
/gate/systems/cylindricalPET/module/attach module
/gate/systems/cylindricalPET/crystal/attach crystal
/gate/systems/cylindricalPET/layer0/attach GSO

# ATTACH CRYSTAL
/gate/GSO/attachCrystalSD
/gate/rsector/attachPhantomSD
/gate/module/attachPhantomSD
```

2. GATE macros for designing a reduced detector system with two pairs of detector modules

```
# WORLD
/gate/world/geometry/setXLength 110. cm
/gate/world/geometry/setYLength 110. cm
/gate/world/geometry/setZLength 50. cm

# CYLINDRICAL
/gate/world/daughters/name cylindricalPET
/gate/world/daughters/insert cylinder
/gate/cylindricalPET/setMaterial Air
/gate/cylindricalPET/geometry/setRmax 52. cm
/gate/cylindricalPET/geometry/setRmin 28. cm
/gate/cylindricalPET/geometry/setHeight 18.3 cm
/gate/cylindricalPET/vis/forceWireframe
/gate/cylindricalPET/vis/setVisible 0

# RSECTOR
/gate/cylindricalPET/daughters/name rsector
/gate/cylindricalPET/daughters/insert box
/gate/rsector/geometry/setXLength 40 mm
/gate/rsector/geometry/setYLength 163.5 mm
/gate/rsector/geometry/setZLength 18.3 cm
/gate/rsector/setMaterial Glass
/gate/rsector/placement/setTranslation 45.2 0 0 cm
```

```
/gate/rsector/vis/forceWireframe
/gate/rsector/vis/setColor red
#/gate/rsector/vis/setVisible 0

# MODULE
/gate/rsector/daughters/name module
/gate/rsector/daughters/insert box
/gate/module/geometry/setXLength 20. mm
/gate/module/geometry/setYLength 163.5 mm
/gate/module/geometry/setZLength 18.3 cm
/gate/module/setMaterial PTFE
/gate/module/placement/setTranslation -10. 0 0 mm
/gate/module/vis/forceWireframe
/gate/module/vis/setColor cyan
#/gate/module/vis/setVisible 0

# CRYSTAL
/gate/module/daughters/name crystal
/gate/module/daughters/insert box
/gate/crystal/geometry/setXLength 20. mm
/gate/crystal/geometry/setYLength 4 mm
/gate/crystal/geometry/setZLength 6 mm
/gate/crystal/setMaterial GSO
/gate/crystal/vis/setColor yellow
#/gate/crystal/vis/setVisible 0

# LAYER GSO
/gate/crystal/daughters/name GSO
/gate/crystal/daughters/insert box
/gate/GSO/geometry/setXLength 20. mm
/gate/GSO/geometry/setYLength 4 mm
/gate/GSO/geometry/setZLength 6 mm
/gate/GSO/setMaterial GSO
/gate/GSO/vis/setColor yellow
#/gate/GSO/vis/setVisible 0

# REPEAT CRYSTAL INTO THE WHOLE MODULE
/gate/crystal/repeaters/insert cubicArray
/gate/crystal/cubicArray/setRepeatNumberX 1
/gate/crystal/cubicArray/setRepeatNumberY 38
/gate/crystal/cubicArray/setRepeatNumberZ 29
```

```
/gate/crystal/cubicArray/setRepeatVector 0. 4.3 6.3 mm

# REPEAT THE RSECTOR INTO THE WHOLE RING
/gate/rsector/repeaters/insert ring
/gate/rsector/ring/setRepeatNumber 4

# ATTACH SYSTEM
/gate/systems/cylindricalPET/rsector/attach rsector
/gate/systems/cylindricalPET/module/attach module
/gate/systems/cylindricalPET/crystal/attach crystal
/gate/systems/cylindricalPET/layer0/attach GSO

# ATTACH CRYSTAL
/gate/GSO/attachCrystalSD
/gate/rsector/attachPhantomSD
/gate/module/attachPhantomSD
```

3. GATE macros for creating a geometric phantom

```
# GEOMETRIC PHANTOM
/gate/world/daughters/name phantom
/gate/world/daughters/insert cylinder
/gate/phantom/geometry/setRmax 10 cm
/gate/phantom/geometry/setRmin 0. cm
/gate/phantom/geometry/setHeight 20. cm
/gate/phantom/setMaterial Water
/gate/phantom/vis/setColor white
#/gate/phantom/vis/forceWireframe
/gate/phantom/vis/forceSolid
```

4. GATE macros for importing the XCAT voxelized phantom

```
# XCAT PHANTOM
/gate/world/daughters/name XCATphantom
/gate/world/daughters/insert regularMatrix
/gate/XCATphantom/setSkipEqualMaterials 0
```

```
/gate/XCATphantom/geometry/insertReader interfile
/gate/XCATphantom/interfileReader/insertTranslator range
/gate/XCATphantom/interfileReader/rangeTranslator/readTable range.dat
/gate/XCATphantom/interfileReader/rangeTranslator/describe 1
/gate/XCATphantom/interfileReader/readFile XCATphan.h33

#/gate/XCATphantom/placement/setTranslation 0. 0. 100. mm
#/gate/XCATphantom/placement/setRotationAxis 0 0 1
#/gate/XCATphantom/placement/setRotationAngle 180 deg

/gate/XCATphantom/attachVoxelPhantomSD
/gate/XCATphantom/addOutput doseOutput
/gate/output/doseOutput/saveUncertainty true
/gate/output/doseOutput/setFileName Dose.bin
```

5. GATE macros for designing a capsule carrying three markers

```
# CAPSULE BOUNDARY
/gate/phantom/daughters/name capsule
/gate/phantom/daughters/insert cylinder
/gate/capsule/geometry/setRmax 6 mm
/gate/capsule/geometry/setRmin 0. mm
/gate/capsule/geometry/setHeight 26 mm
/gate/capsule/placement/setTranslation -57 0 -45 mm
/gate/capsule/setMaterial Air
/gate/capsule/vis/setVisible 0

# FRAME 2 (CAPSULE'S MAIN BODY)
/gate/capsule/daughters/name frame2
/gate/capsule/daughters/insert cylinder
/gate/frame2/geometry/setRmax 6 mm
/gate/frame2/geometry/setRmin 4 mm
/gate/frame2/geometry/setHeight 14 mm
/gate/frame2/setMaterial Plastic
/gate/frame2/vis/setColor red
#/gate/frame2/vis/forceSolid
/gate/frame2/vis/forceWireframe
#/gate/frame2/vis/setVisible 0
```

```
# FRAME 1 (CAPSULE'S TOP)
/gate/capsule/daughters/name frame1
/gate/capsule/daughters/insert sphere
/gate/frame1/geometry/setRmax 6 mm
/gate/frame1/geometry/setRmin 4 mm
/gate/frame1/geometry/setThetaStart 90 deg
/gate/frame1/geometry/setDeltaTheta 180 deg
/gate/frame1/placement/setTranslation 0 0 -7 mm
/gate/frame1/setMaterial Plastic
/gate/frame1/vis/setColor red
#/gate/frame1/vis/forceSolid
/gate/frame1/vis/forceWireframe
#/gate/frame1/vis/setVisible 0

# FRAME 3 (CAPSULE'S BOTTOM)
/gate/capsule/daughters/name frame3
/gate/capsule/daughters/insert sphere
/gate/frame3/geometry/setRmax 6 mm
/gate/frame3/geometry/setRmin 4 mm
/gate/frame3/geometry/setThetaStart 90 deg
/gate/frame3/geometry/setDeltaTheta 180 deg
/gate/frame3/placement/setRotationAxis 1 0 0
/gate/frame3/placement/setRotationAngle 180 deg
/gate/frame3/placement/setTranslation 0 0 7 mm
/gate/frame3/setMaterial Plastic
/gate/frame3/vis/setColor red
#/gate/frame3/vis/forceSolid
/gate/frame3/vis/forceWireframe
#/gate/frame3/vis/setVisible 0

# MARKER 1
/gate/frame1/daughters/name marker1
/gate/frame1/daughters/insert sphere
/gate/marker1/geometry/setRmax 0.5 mm
/gate/marker1/geometry/setRmin 0.25 mm
/gate/marker1/placement/setTranslation 0 0 -5 mm
/gate/marker1/setMaterial Acrylic
/gate/marker1/vis/setColor white
/gate/marker1/vis/forceWireframe

# MARKER 2
```

```
/gate/frame2/daughters/name marker2
/gate/frame2/daughters/insert sphere
/gate/marker2/geometry/setRmax 0.5 mm
/gate/marker2/geometry/setRmin 0.25 mm
/gate/marker2/placement/setTranslation 0 -5 0 mm
/gate/marker2/setMaterial Acrylic
/gate/marker2/vis/setColor red
/gate/marker2/vis/forceWireframe

# MARKER 3
/gate/frame2/daughters/name marker3
/gate/frame2/daughters/insert sphere
/gate/marker3/geometry/setRmax 0.5 mm
/gate/marker3/geometry/setRmin 0.25 mm
/gate/marker3/placement/setTranslation 0 5 0 mm
/gate/marker3/setMaterial Acrylic
/gate/marker3/vis/setColor yellow
/gate/marker3/vis/forceWireframe

# ATTACH PHANTOMSD
/gate/capsule/attachPhantomSD
/gate/marker1/attachPhantomSD
/gate/marker2/attachPhantomSD
/gate/marker3/attachPhantomSD
```

6. GATE macros for defining isotope confined in the markers

```
# SOURCE 1
/gate/source/addSource source1
/gate/source/source1/setActivity 0.000050 curie
/gate/source/source1/gps/particle ion
/gate/source/source1/gps/ion 11 22 0 0
/gate/source/source1/gps/monoenergy 0. eV
/gate/source/source1/setForcedUnstableFlag true
/gate/source/source1/setForcedHalfLife 81993600. s
/gate/source/source1/gps/angtype iso
/gate/source/source1/gps/type Volume
/gate/source/source1/gps/shape Sphere
```

```
/gate/source/source1/gps/radius 0.25 mm
/gate/source/source1/attachTo marker1

# SOURCE 2
/gate/source/addSource source2
/gate/source/source2/setActivity 0.000050 curie
/gate/source/source2/gps/particle ion
/gate/source/source2/gps/ion 11 22 0 0
/gate/source/source2/gps/monoenergy 0. eV
/gate/source/source2/setForcedUnstableFlag true
/gate/source/source2/setForcedHalfLife 81993600. s
/gate/source/source2/gps/angtype iso
/gate/source/source2/gps/type Volume
/gate/source/source2/gps/shape Sphere
/gate/source/source2/gps/radius 0.25 mm
/gate/source/source2/attachTo marker2

# SOURCE 3
/gate/source/addSource source3
/gate/source/source3/setActivity 0.000050 curie
/gate/source/source3/gps/particle ion
/gate/source/source3/gps/ion 11 22 0 0
/gate/source/source3/gps/monoenergy 0. eV
/gate/source/source3/setForcedUnstableFlag true
/gate/source/source3/setForcedHalfLife 81993600. s
/gate/source/source3/gps/angtype iso
/gate/source/source3/gps/type Volume
/gate/source/source3/gps/shape Sphere
/gate/source/source3/gps/radius 0.25 mm
/gate/source/source3/attachTo marker3
```

Appendix B
XCAT phantom parameters

The content of the general parameter file for generating the DYNAMIC XCAT phantom (version 1.0) is shown as follows

0 : activity_phantom_each_frame (1=save phantom to file, 0=don't save)
1 : attenuation_coeff_phantom_each_frame (1=save phantom to file, 0=don't save)
0 : activity_phantom_average (1=save , 0=don't save) see NOTE 0
0 : attenuation_coeff_phantom_average (1=save, 0=don't save) see NOTE 0

0 : motion_option (0=beating heart only, 1=respiratory motion only, 2=both motions) see NOTE 1
5 : output_period (SECS) (if <= 0, then output_period=time_per_frame*output_frames)
0 : time_per_frame (SECS) (**IGNORED unless output_period<=0**)
1 : output_frames (# of output time frames)

1 : hrt_period (SECS) (length of beating heart cycle; normal = 1s) see NOTE 2
0.0 : hrt_start_phase_index (range=0 to 1; ED=0, ES=0.4) see NOTE 2
heart_base : basename for heart files
10 : resp_period (SECS) (length of respiratory cycle; normal breathing = 5s) see NOTE 2
0.0 : resp_start_phase_index (range=0 to 1, full exhale= 0.0, full inhale=0.4) see NOTE 2
2.0 : max_diaphragm_motion (extent in cm's of diaphragm motion; normal breathing = 2 cm) see NOTE 3
1.2 : max_AP_expansion (extent in cm's of the AP expansion of the chest; normal breathing = 1.2 cm) see NOTE 3
diaphragm_curve.dat : name of curve defining diaphragm motion during respiration
ap_curve.dat : name of curve defining chest anterior-posterior motion during respiration
1.0 : lung_detail (level of detail for the airway tree in the lungs, range 0 to 1; 0 = complete tree, 1 = no tree)
0.0 : hrt_motion_x (extent in cm's of the heart's lateral motion during breathing; default = 0.0 cm)

1 : vessel_flag (1 = include arteries and veins, 0 = do not include)
0 : arms_flag (0 = arms down, 1 = arms up, 2 = no arms)
0 : male or female phantom (0 = male, 1 = female), be sure to adjust below accordingly
mtorso.nrb : name of organ file that defines all organs except heart (male = mtorso.nrb, female - ftorso.nrb)
34.5 : body_long_axis (sets body transverse axis - scales only body outline) (visible male = 34.5 cm) (visible female = 33 cm)
27.5 : body_short_axis (sets body AP axis - scales only body outline) (visible male = 27.5 cm) (visible female = 25 cm)
192.0 : body_height (sets height of phantom - scales everything) (visible male = 192 cm) (visible female 188 cm)
30.0 : rib_long_axis (sets ribcage transverse axis - scales everything and repositions the heart to adjust to the scaling) (visible male = 30.0 cm) (visible female = 28.0)
22.7 : rib_short_axis (sets ribcage AP axis - scales everything and repositions the heart to adjust to the scaling) (visible male = 22.7 cm) (visible female = 21.0)

95.05 : phantom_weight (sets the weight of the phantom) (visible male = 95.05 kg, visible female = 86.0 kg) (overrides body_long and body_short_axis parameters as well as rib_long, rib_short_axis and rib_height parameters above) See NOTE 3A

0 : render marrow (0 = no, 1 = yes)
0.4 : thickness sternum (cm)
0.3 : thickness ribs (cm)
0.4 : thickness backbone (cm)
0.35 : thickness scapula (cm)
0.35 : thickness collarbones (cm)
0.45 : thickness humerus (cm)
0.45 : thickness radius (cm)
0.45 : thickness ulna (cm)
0.35 : thickness hand bones (cm)
0.5 : thickness femur (cm)
0.6 : thickness tibia (cm)
0.5 : thickness fibula (cm)
0.3 : thickness patella (cm)
0.4 : thickness foot bones (cm)

0.6 : thickness of small intestine wall (cm)
0.6 : thickness of large intestine wall (cm)
3.6 : rectum_long_axis (sets diameter of rectum transverse axis; visible male = 36 cm)
4.9 : rectum_short_axis (sets rectum AP axis diameter; visible male = 49.0 cm)
4 : location of air in the large intestine and rectum see NOTE 4

1.0 : hrt_scale (scales heart in 3D - 1.0 is visible male) (Can use this to alter the heart or the following, but not both)
9.43 : hrt_lv_length (sets the length of the LV - entire heart is scaled with the LV) (XCAT heart = 9.43 cm)
2.97 : hrt_lv_radius (sets the ave. radius of the LV - entire heart is scaled with the radius) (XCAT heart = 2.97 cm)
18 : twist
1 : breast_type (0=supine, 1=prone)
0 : which_breast (0 = none, 1 = both, 2 = right only, 3=left only)
18.2 : breast_long_axis (sets the breasts lateral dimension) (PRONE normal = 15.1 cm, SUPINE normal = 18.2 cm)
7.0 : breast_short_axis (sets the breasts antero-posterior dimension) (PRONE normal = 7.0 cm, SUPINE = 4.0 cm)
14.0 : breast_height (sets the breasts height) (PRONE normal = 14.0 cm, SUPINE normal = 14.9 cm)
4.6 : theta angle of the breasts (angle the breasts are tilted transversely (sideways) from the center of the chest (PRONE normal = 4.6, SUPINE NORMAL = 40.0)
0.0 : phi angle of the breasts (angle the breasts are tilted up (+) or down (-) (PRONE normal = 0, SUPINE normal = -20.0)

3.4 : height of right_diaphragm/liver dome (visible human = 3.4 cm, height = 0 is a flat diaphragm)
1.9 : height of left diaphragm dome (visible human = 1.9 cm, height = 0 is a flat diaphragm)
1.0 : intv in cm (thickness of body tissue around the heart and liver)

0.4 : pixel width (cm); see NOTE 5
0.4 : slice width (cm); see NOTE 5
150 : array size see NOTE 6
1 : subvoxel_index (=1,2,3,4 -> 1,8,27,64 subvoxels/voxel, respectively)
235 : start_slice; see NOTE 7
412 : end_slice; see NOTE 7

-90 :	zy_rotation (beta) in deg. (-90); see NOTE 8
-20. :	xz_rotation (phi) in deg. (-20); see NOTE 8
-50. :	yx_rotation (psi) in deg. (-50); see NOTE 8
0.0 :	x translation in mm ; see NOTE 8
0.0 :	y translation in mm ; see NOTE 8
20.0 :	z translation in mm ; see NOTE 8
0.0 :	apical_thinning (0 to 1.0 scale, 0.0 = not present, 0.5 = halfway present, 1.0 = completely thin)
0.0 :	valve thickness in cm (0= no valve); cannot be a negative value /*parameter is ignored*/
0.3 :	av_step(cm): step width for smooth change between Atr & Ven (0=none) /*parameter is ignored*/
0 :	total_rotation (deg); /*parameter is ignored*/
0 :	activity units (1= scale by voxel volume; 0= don't scale) NOTE 9

SEE NOTE 9 FOR INFORMATION ON SETTING ORGAN ACTIVITIES - activities can be fixed or determined by user defined time-activity curves

0 :	myoLV_time_curve (1= activity determined by a time-activity curve; 0= fixed activity)
75 :	hrt_myoLV_act - fixed activity in left ventricle myocardium if above option is 0
sample_act.txt :	myoLV_act_filename - name of file containing time-activity curve for LV myocardium
0 :	myoRV_time_curve (1= activity determined by a time-activity curve; 0= fixed activity)
75 :	hrt_myoRV_act - activity in right ventricle myocardium
sample_act.txt :	myoRV_act_filename - name of file containing time-activity curve for RV myocardium
0 :	myoLA_time_curve (1= activity determined by a time-activity curve; 0= fixed activity)
75 :	hrt_myoLA_act - activity in left atrium myocardium
sample_act.txt :	myoLA_act_filename - name of file containing time-activity curve for LA myocardium
0 :	myoRA_time_curve (1= activity determined by a time-activity curve; 0= fixed activity)
75 :	hrt_myoRA_act - activity in right atrium myocardium
sample_act.txt :	myoRA_act_filename - name of file containing time-activity curve for RA myocardium
0 :	bldplLV_time_curve (1= activity determined by a time-activity curve; 0= fixed activity)
2 :	hrt_bldplLV_act - activity in left ventricle chamber (blood pool)
sample_act.txt :	bldplLV_act_filename - name of file containing time-activity curve for LV blood pool
0 :	bldplRV_time_curve (1= activity determined by a time-activity curve; 0= fixed activity)
2 :	hrt_bldplRV_act - activity in right ventricle chamber (blood pool)
sample_act.txt :	bldplRV_act_filename - name of file containing time-activity curve for RV blood pool
0 :	bldplLA_time_curve (1= activity determined by a time-activity curve; 0= fixed activity)
2 :	hrt_bldplLA_act - activity in left atria chamber (blood pool)
sample_act.txt :	bldplLA_act_filename - name of file containing time-activity curve for LA blood pool
0 :	bldplRA_time_curve (1= activity determined by a time-activity curve; 0= fixed activity)
2 :	hrt_bldplRA_act - activity in right atria chamber (blood pool)
sample_act.txt :	bldplRA_act_filename - name of file containing time-activity curve for RA blood pool
0 :	body_time_curve (1= activity determined by a time-activity curve; 0= fixed activity)
2 :	body_activity (background activity);
sample_act.txt :	body_act_filename - name of file containing time-activity curve for body
0 :	liver_time_curve (1= activity determined by a time-activity curve; 0= fixed activity)
75.0 :	liver_activity;
sample_act.txt :	liver_act_filename - name of file containing time-activity curve for liver
0 :	gall_bladder_time_curve (1= activity determined by a time-activity curve; 0= fixed activity)
60 :	gall_bladder_activity;
sample_act.txt :	gall_bladder_act_filename - name of file containing time-activity curve for gall bladder
0 :	lung_time_curve (1= activity determined by a time-activity curve; 0= fixed activity)
4 :	lung_activity;
sample_act.txt :	lung_act_filename - name of file containing time-activity curve for lungs

0 :	st_wall_time_curve (1= activity determined by a time-activity curve; 0= fixed activity)
2 :	st_wall_activity; (stomach wall)
sample_act.txt :	st_wall_act_filename - name of file containing time-activity curve for stomach wall
0 :	st_cnts_time_curve (1= activity determined by a time-activity curve; 0= fixed activity)
2 :	st_cnts_activity; (stomach contents)
sample_act.txt :	st_cnts_act_filename - name of file containing time-activity curve for stomach contents
0 :	kidney_time_curve (1= activity determined by a time-activity curve; 0= fixed activity)
75 :	kidney_activity;
sample_act.txt :	kidney_act_filename - name of file containing time-activity curve for kidneys
0 :	spleen_time_curve (1= activity determined by a time-activity curve; 0= fixed activity)
75 :	spleen_activity;
sample_act.txt :	spleen_act_filename - name of file containing time-activity curve for spleen
0 :	rib_time_curve (1= activity determined by a time-activity curve; 0= fixed activity)
5 :	rib_activity;
sample_act.txt :	rib_act_filename - name of file containing time-activity curve for ribs
0 :	bone_time_curve (1= activity determined by a time-activity curve; 0= fixed activity)
10 :	bone_activity;
sample_act.txt :	bone_act_filename - name of file containing time-activity curve for remaining bones
0 :	spine_head_time_curve (1= activity determined by a time-activity curve; 0= fixed activity)
6 :	spine_head_activity;
sample_act.txt :	spine_head_act_filename - name of file containing time-activity curve for spine
0 :	spine_process_time_curve (1= activity determined by a time-activity curve; 0= fixed activity)
6 :	spine_process_activity;
sample_act.txt :	spine_preocess_act_filename - name of file containing time-activity curve for spine
0 :	pelvis_time_curve (1= activity determined by a time-activity curve; 0= fixed activity)
2 :	pelvis_activity;
sample_act.txt :	pelvis_act_filename - name of file containing time-activity curve for pelvis bone
0 :	bone_marrow_time_curve (1= activity determined by a time-activity curve; 0= fixed activity)
2 :	bone_marrow_activity;
sample_act.txt :	bone_marrow_act_filename - name of file containing time-activity curve for bone marrow
0 :	artery_time_curve (1= activity determined by a time-activity curve; 0= fixed activity)
2 :	artery_activity;
sample_act.txt :	artery_act_filename - name of file containing time-activity curve for arteries
0 :	vein_time_curve (1= activity determined by a time-activity curve; 0= fixed activity)
2 :	vein_activity;
sample_act.txt :	vein_act_filename - name of file containing time-activity curve for veins
0 :	bladder_time_curve (1= activity determined by a time-activity curve; 0= fixed activity)
2 :	bladder_activity;
sample_act.txt :	bladder_act_filename - name of file containing time-activity curve for bladder
0 :	prostate_time_curve (1= activity determined by a time-activity curve; 0= fixed activity)
30 :	prostate_activity;
sample_act.txt :	prostate_act_filename - name of file containing time-activity curve for prostate
0 :	ascending_large_intest_time_curve (1= activity determined by a time-activity curve; 0= fixed activity)
2 :	ascending_large_intest_activity;
sample_act.txt :	ascending_large_intest_act_filename - name of file containing time-activity curve for ascending l. intest.

0 :	transcending_large_intest_time_curve (1= activity determined by a time-activity curve; 0= fixed activity)
2 :	transcending_large_intest_activity;
sample_act.txt :	transcending_large_intest_act_filename - name of file containing time-activity curve for transc. l. intest.
0 :	descending_large_intest_time_curve (1= activity determined by a time-activity curve; 0= fixed activity)
2 :	desc_large_intest_activity;
sample_act.txt :	desc_large_intest_act_filename - name of file containing time-activity curve for desc. l. intest.
0 :	small_intest_time_curve (1= activity determined by a time-activity curve; 0= fixed activity)
2 :	small_intest_activity;
sample_act.txt :	small_intest_act_filename - name of file containing time-activity curve for small intestine
0 :	rectum_time_curve (1= activity determined by a time-activity curve; 0= fixed activity)
2 :	rectum_activity;
sample_act.txt :	rectum_act_filename - name of file containing time-activity curve for rectum
0 :	seminal_vessicles_time_curve (1= activity determined by a time-activity curve; 0= fixed activity)
2 :	sem_vess_activity;
sample_act.txt :	sem_vess_act_filename - name of file containing time-activity curve for sem. ves.
0 :	vas_deferens_time_curve (1= activity determined by a time-activity curve; 0= fixed activity)
2 :	vas_def_activity;
sample_act.txt :	vas_def_act_filename - name of file containing time-activity curve for vas def.
0 :	testicular_time_curve (1= activity determined by a time-activity curve; 0= fixed activity)
2 :	testicular_activity;
sample_act.txt :	testicular_act_filename - name of file containing time-activity curve for test.

2 :	pericardium activity;
2 :	cartilage activity;
5 :	cortical activity;
2.0 :	ascending large intestine air activity;
2.0 :	transverse large intestine air activity;
2.0 :	descending large intestine air activity;
2.0 :	small intestine air activity;
2.0 :	rectum air activity;
2.0 :	ureter activity;
2.0 :	urethra activity;
2.0 :	lymph normal activity;
2.0 :	lymph abnormal activity;
2.0 :	airway tree activity
60 :	uterus_activity;
50 :	vagina_activity;
40 :	right_ovary_activity;
30 :	left_ovary_activity;
20 :	fallopian tubes_activity;
140 :	radionuclide energy in keV (range 1-1000 keV) ; for attn. map only

NOTE 0 : The average phantom is the average ONLY OF THOSE FRAMES GENERATED. That is, if you specify that only 2 frames be generated, then the average phantom is just the average of those 2 frames.
FOR A GOOD AVERAGE, generate at least 8-16 frames per 1 complete heart cycle and/or per 1 complete respiratory cycle.

NOTE 1 : Heart motion refers to heart BEATING or contraction, while resp. motion refers to organ motion due to breathing. Note that the entire heart is translated or rotated due to resp. motion, even if it is not contracting.
IF motion_option=1, THE HEART WILL MOVE (TRANSLATE) BUT NOT BEAT.

NOTE 2 : - Users sets the length and starting phase of both the heart and respiratory cycles. NORMAL values for length of heart beat and respiratory are cycles are 1 sec. and 5 secs., respectively, BUT THESE CAN VARY AMONG PATIENTS and will increase if the patient is under stress.
- An index value between 0 and 1 is used the specify the starting phase of the heart or resp cycles. IF NO MOTION IS SPECIFIED THEN THE STARTING PHASE IS USED AS THE SINGLE PHASE AT WHICH THE PHANTOM IS GENERATED. (see documentation for more details).

NOTE 3 : - These NORMAL values are for normal tidal breathing.
** Modeling a deep inhale may require higher values. **
- The AP_expansion parameter controls the anteroposterior diameter of the ribcage, body, and lungs. The ribs rotate upward to expand the chest cavity by the amount indicated by the AP_expansion parameter. The lungs and body move with the expanding ribs. There is maximum amount by which the AP diameter can expand, due to the size of the ribs (some expansions are impossible geometrically.) If the user specifies too great an expansion, the program will terminate with an error message.
- The diaphragm motion controls the motion of the liver, the left diaphragm, the heart, stomach, and spleen. The liver is set to move forward during inspiration an amount equal to the AP expansion of the chest as controlled by the rib/body short axes. The liver moves back to its original position during expiration. The liver is also set to move up/down with the diaphragm. The heart moves with the liver. The stomach and spleen also move with the liver but at a reduced extent.

NOTE 3A : Setting the weight of the phantom will override the body_long and body_short_axis parameters and the rib_long and rib_short_axis parameters. The body_height parameter will set the height of the phantom by scaling about the z axis. Then the body weight will be set by scaling the phantom about the x and y axes.

NOTE 4 : Location of air in the large intestine and rectum
4 = air visible in the entire large intestine and rectum
3 = air visible in ascending, transverse, and descending portions of the large intestine
2 = air visible in ascending and transverse portions of the large intestine
1 = air visible in ascending portion of the large intestine only
0 = no air visible (entire large intestine and rectum filled with contents)

NOTE 5 : Currently, only cubic voxels allowed, therefore,
voxel_volume = $(\text{voxel\_width})^3$

NOTE 6 : - The complete phantom array is 3 dimensional with each dimension=array_size
- Typically, 60 cm x 60 cm is the largest camera field-of-view so the MCAT code has an internal check which prints out a warning in the *_log file if (array_size*pixel_width) >= 60.0; therefore, to keep the FOV less than 60 cm:
+ if array_size =128 –> pixel_width <= 0.468
+ if array_size = 64 –> pixel_width <= 0.937
- Make sure $(\text{array\_size})^3$ is smaller than or equal to the size of the array fphan() (or fphana()) as declared in the main program

NOTE 7 : - The phantom dimensions do not necessarily have to be cubic. The array_size parameter determines the x and y dimensions of the images. The number of slices in the z dimension is determined by the start_slice and end_slice parameters. The total number of slices is end_slice - start_slice + 1.

NOTE 8 : - Rotation parameters determine initial orientation of beating (dynamic) heart LV long axis see the subroutine CALC_DYN_HEART_ROT_MATRIX for details

zy_rotation : +y-axis rotates toward +z-axis (about x-axis) by beta

xz_rotation : +z-axis rotates toward +x-axis (about y-axis) by phi

yx_rotation : +x-axis rotates toward +y-axis (about z-axis) by psi

- Based on patient data, the mean and SD heart orientations are:

zy_rot = -110 degrees (no patient data for this rotation)

xz_rot = 23 $\pm$ 10 deg.

yx_rot = -52 $\pm$ 11 deg.

NOTE 9 : If option 1 is chosen, the values of the activity specified in this parameter file are scaled by the voxel volume

FOR EXAMPLE:

1) body_activity = 1.0 and unit option equal 1

=> phantom will output the value 1.0*(pixel_width)^3 in body voxel

OR

2) body_activity = 1.0 and unit option equal 0

=> phantom will output the value 1 in body voxels

Appendix C
List of Publications

[1] T. D. Than, G. Alici, S. Harvey, H. Zhou, and W. Li, "Rigid-body transformation between points and lines in 3d space for the localization of robotic endoscopic capsules," *International Journal of Robotics Research*, 2015. (submitted).

[2] T. Than, G. Alici, S. Harvey, G. OKeefe, H. Zhou, W. Li, T. Cook, and S. Alam-Fotias, "An effective localization method for robotic endoscopic capsules using multiple positron emission markers," *IEEE Transactions on Robotics*, vol. 30, no. 5, pp. 1174–1186, 2014.

[3] T. D. Than, G. Alici, S. Harvey, H. Zhou, and W. Li, "Concept and simulation study of a novel localization method for robotic endoscopic capsules using multiple positron emission markers," *Medical Physics*, vol. 41, no. 7, p. 072501, 2014.

[4] M. R. Yuce, G. Alici, and T. D. Than, "Wireless endoscopy," *Wiley Encyclopedia of Electrical and Electronics Engineering*, 2014.

[5] H. Zhou, G. Alici, T. D. Than, and W. Li, "Experimental investigation into biomechanical and biotribological properties of a real intestine and their significance for design of a spiral-type robotic capsule," *Proceedings of the Institution of Mechanical Engineers, Part H: Journal of Engineering in Medicine*, vol. 228, no. 3, pp. 280–286, 2014.

[6] H. Zhou, G. Alici, T. D. Than, and W. Li, "Modeling and experimental investigation of rotational resistance of a spiral-type robotic capsule inside a real intestine," *IEEE/ASME Transactions on Mechatronics*, vol. 18, no. 5, pp. 1555 – 1562, 2013.

[7] H. Zhou, G. Alici, T. Than, and W. Li, "Modeling and experimental characterization of propulsion of a spiral-type microrobot for medical use in gas-

trointestinal tract," *IEEE Transactions on Biomedical Engineering*, vol. 60, no. 6, pp. 1751 – 1759, 2013.

[8] T. D. Than, G. Alici, H. Zhou, and W. Li, "A review of localization systems for robotic endoscopic capsules," *IEEE Transactions on Biomedical Engineering*, vol. 59, no. 9, pp. 2387–2399, 2012.

[9] H. Zhou, G. Alici, T. D. Than, and W. Li, "Modeling and experimental investigation on the mechanical behavior of a spiral-type capsule in the small intestine," in *2013 IEEE/ASME International Conference on Advanced Intelligent Mechatronics (AIM)*. IEEE, 2013, pp. 1260–1265.

[10] H. Zhou, G. Alici, T. D. Than, and W. Li, "An investigation into biomechanical and biotribological properties of a real intestine for design of a spiral-type robotic capsule," in *2013 IEEE/ASME International Conference on Advanced Intelligent Mechatronics (AIM)*. IEEE, 2013, pp. 71–76.

[11] H. Zhou, G. Alici, T. Than, and W. Li, "Modeling and experimental investigation of viscoelastic contact between a spiral-type robotic capsule and a gastrointestinal tract," in *Proceedings of the 2012 IEEE International Conference on Robotics and Biomimetics (ROBIO)*. IEEE, 2012, pp. 1305–1310.

[12] H. Zhou, G. Alici, T. D. Than, W. Li, and S. Martel, "Magnetic propulsion of a spiral-type endoscopic microrobot in a real small intestine," in *2012 IEEE/ASME International Conference on Advanced Intelligent Mechatronics (AIM)*. IEEE, 2012, pp. 63–68.